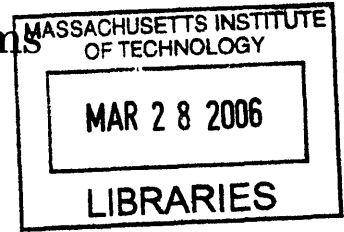


# Control of Open Quantum Systems



by

Nicolas Boulant

Submitted to the Department of Nuclear Engineering  
in partial fulfillment of the requirements for the degree of  
Doctor of Philosophy in Nuclear Science and Engineering

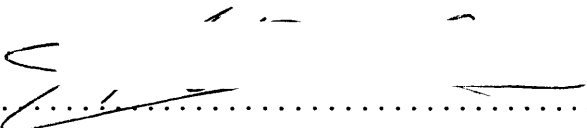
**ARCHIVES**

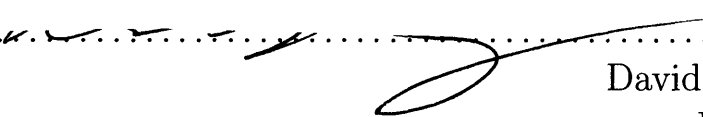
at the


MASSACHUSETTS INSTITUTE OF TECHNOLOGY

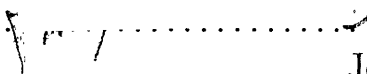
[February 2005]  
November 2004

© Massachusetts Institute of Technology 2004. All rights reserved.

Author .....   
Department of Nuclear Engineering  
November 22, 2004

Certified by .....   
David G. Cory  
Professor  
Thesis Supervisor

Read by .....   
Peter Shor  
Professor  
Thesis Reader

Accepted by .....   
Jeffrey Coderre  
Chairman, Department Committee on Graduate Students

0000000000

# Control of Open Quantum Systems

by

Nicolas Boulant

Submitted to the Department of Nuclear Engineering  
on November 22, 2004, in partial fulfillment of the  
requirements for the degree of  
Doctor of Philosophy in Nuclear Science and Engineering

## Abstract

This thesis describes the development, investigation and experimental implementation via liquid state nuclear magnetic resonance techniques of new methods for controlling open quantum systems.

First, methods that improve coherent control through the use of both strong control fields and detailed knowledge of the subsystem's Hamiltonian are demonstrated. With the aid of numerical search methods, pulsed irradiation schemes are obtained that perform accurate, arbitrary, selective gates on multi-qubit systems. For systems of 3 and 4 qubits, simulations show that the control sequences faithfully implement unitary operations with gate fidelities on the order of 0.999 while experimentally determined correlations of 0.99 were obtained. The technique is then extended to account for the incoherent errors arising from the slow variation of control parameters. It is demonstrated in this study that such errors can be greatly counteracted directly from the design of the time-dependent control fields if some knowledge about the incoherence source is available. The results obtained show a substantial decrease of the non-unitary features normally caused by incoherent noise.

The methods are applicable to a variety of experimental studies in quantum information processing. To test the control techniques, we carried out two benchmark experiments, namely an entanglement transfer and an entanglement swapping experiment performed on a 4-qubit system. The second experiment, while more complex, yields significantly better results, thereby showing the improvement made by the further development of the control techniques.

To optimally protect a quantum system against various decoherent errors, it is essential to design methods to acquire knowledge about them. It is in this context that we then develop a robust method for quantum process tomography for measuring relaxation superoperators and Lindblad operators, which is experimentally tested.

Finally, we explore both theoretically and experimentally the concatenation of a quantum error correction code with a decoherence-free subspace scheme. Using the two techniques, a 4-qubit quantum system is efficiently protected against a noise containing partial symmetry. To date, this is the first experimental demonstration of such a concatenation scheme.

Thesis Supervisor: David G. Cory

Title: Professor



## Acknowledgments

First, I would like to thank my advisor, Prof. David G. Cory. His knowledge, intuition and honesty in science have been very inspiring. I want to thank him for having given me the chance to work in his lab and to work in such a great team.

I want to thank my first labmates with whom I worked my first three years at MIT: Evan Fortunato, Marco Pravia (my good friend Garcon), Lorenza Viola (thank you for your support), Grum Teklemariam (Yo G Yo) and Greg Boutis (OK). I consider myself very lucky to have worked with so brilliant people.

In the next two years, I had the chance to interact also with Joseph Emerson with whom I enjoyed a lot talking about science and life. We had a lot of nice laughs. I enjoyed working also with Tim Havel, Sekhar Ramanathan, Joon, Paola Capellaro (my homework partner), Jonathan Hodges, Zhiying Chen, Suddha Sinha (Cancun), Michael Henry (Texas), Jamie Yang (dude) and Dan Caputo. Thanks also a lot to Sugi Furuta with whom I enjoyed collaborating in Cambridge UK. Our discussions and trips were very productive and fun. At MIT, I would also like to thank Karl Berggren's group for welcoming me and teaching me some nanofabrication. Finally, thanks to all my MIT professors with whom I learnt so much.

Out of MIT, I want to thank the whole Millerick family: Gerard, Martin, Peter, Edward, Lorraine and Anne. Thanks a lot for your friendship and all this great time we spent together !

I want also to thank my friends and some of my family members in France for their friendship and support: the affranloulous, Laure (working girl), Estelle (la Jacquasse), Fabien (Raggasonic), Damien (la Mouchasse), Aurelien (la Badasse), mes amis du Nord, Marion (Pilou), the Chopin and the Poirot families. Thanks also to Pol-Bernard Gossiaux for his support and encouragement while I was still at EMN.

Finally, and most importantly, I would like to thank my dear American friend Gerard Millerick, my brother Alexandre, and my parents for their love and support.



# Contents

|          |  |           |
|----------|--|-----------|
| <b>1</b> | <b>Introduction</b>  | <b>17</b> |
| <b>2</b> | <b>Quantum Control</b>   | <b>19</b> |
| 2.1      | Metrics of Control . . . . .   | 20        |
| 2.2      | Designing Gates for Controlling Quantum Information . . . . .        | 23        |
| 2.2.1    | NMR Spin System . . . . .  | 23        |
| 2.2.2    | Numerical Search Method . . . . .                                    | 24        |
| 2.2.3    | Gate Simulations . . . . .   | 26        |
| 2.3      | Systematic Errors . . . . .  | 29        |
| 2.3.1    | Variations in the External Hamiltonian . . . . .                     | 30        |
| 2.3.2    | Variations in the Internal Hamiltonian . . . . .                     | 30        |
| 2.3.3    | RF Waveform Feedback Correction . . . . .                            | 32        |
| 2.4      | Experimental Demonstrations . . . . .                                | 35        |
| 2.5      | Conclusion . . . . .   | 37        |
| <b>3</b> | <b>Counteracting Incoherent Errors</b>                               | <b>39</b> |
| 3.1      | Background . . . . .   | 39        |
| 3.2      | Modeling, Measurement and Analysis of Incoherent Processes . . . . . | 41        |
| 3.2.1    | Incoherent Processes in NMR Spectroscopy . . . . .                   | 42        |
| 3.2.2    | Designing Pulses That Compensate for RF Inhomogeneity . . . . .      | 44        |
| 3.3      | Eigenvalue Spectra of Superoperators . . . . .                       | 45        |
| 3.3.1    | Perturbation Analysis of Superoperator Eigenvalue Spectra . . . . .  | 46        |
| 3.3.2    | Eigenvalue Spectra for Uncompensated Pulses . . . . .                | 47        |
| 3.3.3    | Eigenvalue Spectra for the Compensated Pulses . . . . .              | 49        |
| 3.3.4    | Symmetric Inhomogeneity Profile . . . . .                            | 50        |
| 3.4      | Simple Experimental Demonstrations . . . . .                         | 50        |
| 3.5      | Conclusion . . . . .   | 53        |
| <b>4</b> | <b>Experimental Benchmarks</b>                                       | <b>55</b> |
| 4.1      | Entanglement Transfer Experiment . . . . .                           | 55        |
| 4.2      | Entanglement Swapping Experiment . . . . .                           | 60        |
| 4.2.1    | The Experiment . . . . .   | 60        |
| 4.2.2    | Measurement in the Bell Basis . . . . .                              | 62        |
| 4.3      | Conclusion . . . . .   | 64        |

|          |  |           |
|----------|--|-----------|
| <b>5</b> | <b>Quantum Process Tomography</b>                                  | <b>65</b> |
| 5.1      | Introduction . . . . .   | 65        |
| 5.2      | Computational Procedure . . . . .                                  | 67        |
| 5.3      | Experimental Validation . . . . .                                  | 71        |
| 5.4      | Interpretation via Lindblad and Hadamard Operators . . . . .       | 75        |
| 5.5      | Conclusion . . . . .   | 78        |
| <b>6</b> | <b>Concatenated Quantum Error-Correcting Codes</b>                 | <b>79</b> |
| 6.1      | Concatenation between Active and Passive Error Control Codes . . . | 80        |
| 6.2      | Experimental Implementation . . . . .                              | 82        |
| 6.3      | Results . . . . .  | 84        |
| 6.4      | Discussion . . . . .   | 87        |
| 6.5      | Conclusion . . . . .   | 92        |



# List of Figures

|     |  |    |
|-----|--|----|
| 2-1 | <b>Molecular structure and Hamiltonian parameters for alanine and crotonic acid.</b> The chemical shift of each carbon nucleus is given in the corresponding diagonal element while the coupling strengths are given by the off-diagonal values. All values are in Hertz, and they were measured in a 300 MHz ( $\sim 7$ T) magnet. . . . .  | 24 |
| 2-2 | <b>Ideal RF waveform for two example pulses.</b> The solid (dashed) line is the amplitude (phase) of the waveform. Changes in the transmitter frequency (within a single period) were implemented by a discrete linear phase ramp. The sharp discontinuities occur at the transitions between periods. Substantial filtering of these high frequency components (smoothing of the shape) has little effect on the gate fidelity. In order to experimentally implement the pulse, it is converted into a discrete series of amplitudes and phases (order 1K long) by sampling the ideal waveform at a constant rate. Details of the pulse parameters (as per Eqn. 2.24) are listed below each waveform. Due to experimental implementation issues, a $6 \mu\text{s}$ period with zero RF power ( <i>i.e.</i> , $H_{ext} = 0$ ) is needed before and after the pulse and must be included to produce the desired propagator. . . . . | 28 |
| 2-3 | <b>Exploration of achievable fidelities.</b> The plot shows the maximum fidelities found for a $\pi/2 _x^2$ alanine pulse as allowed RF power and magnetic field strength were varied. The three lines correspond to the magnetic field strengths explored, as denoted by the legend. The dotted vertical lines mark the point of the minimum chemical shift difference at each of the three field strengths. Using ideal experimental control in a 800 MHz magnet, a single-spin gate fidelity reaching 0.99999 is potentially realizable. . . . .  | 29 |
| 2-4 | <b>Gate fidelity vs. variations in experimental parameters.</b> The experimental parameters were varied over the range of expected errors, demonstrating that both the alanine and crotonic acid pulses are most sensitive to RF amplitude. . . . .  | 30 |

|     |  |    |
|-----|--|----|
| 2-5 | <b>Gate fidelity vs. spin frequency.</b> The gate fidelities of two example pulses were calculated as a function of the resonance frequency of a test spin. The frequency was varied in the range of chemical shifts of the molecules. The solid (dashed) line is calculated with identity (desired transformation) as the theoretical transformation. The vertical dotted lines denote the actual chemical shifts for each spin. As can be seen, the gate only works when the test spin is at the appropriate resonance frequency. . . . .  | 31 |
| 2-6 | <b>Feedback loop for correcting experimental RF waveforms.</b> Distorted signals arriving at the carbon coil are detected and digitized through the proton coil. The difference between the measured RF wave and the desired wave is then calculated, resulting in a fixed wave that is then retransmitted to the coil. The loop continues until the shape of the fixed wave produces the desired signal at the carbon coil.   | 33 |
| 2-7 | <b>Improvement of errors in digitized RF waveforms.</b> The errors from a test sample of 25 waveforms are plotted here as a function of the feedback loop iteration number. The errors are the mean absolute differences between fits to the digitized waveform and the ideal waveform. Three to four iterations were typically sufficient to improve the RF shape. . . . .  | 34 |
| 2-8 | <b>Distorted and corrected RF amplitudes.</b> The solid line represents the desired shape, while the dashed and dotted-dashed lines correspond to the initial measured waveform and the final one (after two iterations of the feedback code) respectively. The high frequency transients present at the transitions between periods have little effect on the overall performance of the gates. . . . .   | 35 |
| 2-9 | <b>Spectra resulting from different sequences of pulses applied to the thermal equilibrium density matrix <math>\rho_{thermal} = I_z^1 + I_z^2 + I_z^3</math>.</b> All sequences are read from left to right. The reference spectra (resulting from a $\frac{\pi}{2}$ pulse applied to all 3 carbons) is also shown (grey) for reference. Although the chemical shift is of order $\frac{1}{\tau}$ , no significant phase evolution is seen. Selective coupling sequences are also demonstrated. The phase correction used for all the spectra is strictly the same for all of them and is done such that the reference spectrum ( $\pi/2$ pulse on all the spins at thermal equilibrium) is perfectly absorptive. | 36 |
| 3-1 | <b>Radio-frequency inhomogeneity profile.</b> The RF inhomogeneity in the carbon channel was measured using a spin nutation experiment. The resulting decaying signal was Fourier transformed to distill the various RF nutation frequencies present in the sample. The dotted line is the plot of the Fourier transformation, and it is the measured RF inhomogeneity profile. The solid gray line is the profile that was used to design pulses compensated for RF inhomogeneity, and it was extracted from the measured profile. . . . .  | 44 |

|     |   |    |
|-----|---|----|
| 3-2 | <b>Simulations of compensated and uncompensated pulses as a function of radio-frequency strengths and distribution widths.</b><br>The dashed lines correspond to compensated pulses, while the solid gray lines denote uncompensated pulses. The left plot shows how the compensated pulses maintain high fidelities even when the RF strength is scaled from the ideal value. The plot on the right simulates the same pulses as a function of the scaled width of the RF inhomogeneity profile. These results demonstrate the improved fidelity of the compensated pulses for all but the narrowest RF distributions. At the small widths, the RF profile would no longer be inhomogeneous, eliminating the need for the compensated gates. . . . . | 45 |
| 3-3 | <b>Eigenvalue spectrum of the simulated superoperator for a test gate and the radio-frequency inhomogeneity profile shown in Fig. 3-1.</b> The dots are the exact eigenvalues of $S$ while the crosses are the ones obtained by using the first order perturbation analysis. The zoom box shows some of the detail in the left-hand side of the plot. The additional trend line drawn in the zoomed plot emphasizes the fact that the larger the phase shift, the larger the attenuation. . . . .   | 48 |
| 3-4 | <b>Eigenvalue spectrum of the simulated superoperators corresponding to a compensated and uncompensated pulse.</b> The dots correspond to the uncompensated gate, while the crosses correspond to the compensated one. Note that the crosses basically lie on the unit circle while the dots are spread inside, confirming the closer-to-unitary behavior of the compensated gates. . . . .   | 49 |
| 3-5 | <b>Eigenvalue spectrum of the simulated superoperator for the symmetric radio-frequency inhomogeneity profile.</b> The dots are the unperturbed eigenvalues and the crosses are the ones computed by using first order perturbation theory. The symmetry in the distribution mainly results in some attenuation of the eigenvalues with no phase shift. The zoom box allows more detail to be seen for the eigenvalues close to $-1$ . . . . .  | 51 |
| 4-1 | <b>Logical network for the entanglement transfer experiment.</b><br>The four spins are represented by the four horizontal control lines, where each line is labelled on the left by the input state superscripted by the spin's index (where "1" indicates that the spin is depolarized and $E_+$ indicates that it was part of the pseudo-pure state). The pseudo-pure ground state on spins 2 and 3, $\rho_{pp}^{23} \leftrightarrow  00\rangle\langle 00 $ , is converted by an entanglement operation on the same spins to obtain $\rho_{Ent}^{23} \leftrightarrow \frac{1}{2}( 00\rangle +  11\rangle)(\langle 00  + \langle 11 )$ . This state is then transferred to spins 1 and 4 by using swap gates. . . . .                                | 56 |
| 4-2 | <b>Molecule of crotonic acid.</b> . . . . .   | 57 |

|     |  |    |
|-----|--|----|
| 4-3 | <b>Experimental density matrices.</b> From left to right are shown the real part of the reconstructed density matrices of the initial pseudo-pure $\rho_{pp}^{23}$ , spins 2&3 entangled $\rho_{Ent}^{23}$ and spins 1&4 entangled $\rho_{Ent}^{14}$ (in normalized units). The bottom row of density matrices is obtained from the top row after having traced over the two ancilla spins. The rows and columns represent the standard computational basis in binary order, with $\langle 0000 $ starting on the leftmost column and $\langle 1111 $ being the rightmost column. . . . .  | 59 |
| 4-4 | <b>Logical network for the entanglement swapping experiment.</b> The four qubits are initialized to the full pseudo-pure state $ \psi\rangle_{12} \otimes  \psi\rangle_{34}$ where $ \psi\rangle = \frac{1}{\sqrt{2}}( 01\rangle -  10\rangle)$ . The CNOT and Hadamard gates then map the Bell basis to the computational one. That operation followed by a strong measurement in the computational basis mimicks a strong measurement in the Bell basis. . . . .   | 61 |
| 4-5 | <b>Real part of the initial density matrix (product of singlet states).</b> The rows and columns represent the standard computational basis in binary order, with $\langle 0000 $ starting from the leftmost column and $\langle 1111 $ being the rightmost column. . . . .  | 62 |
| 4-6 | <b>Bell states.</b> For the sake of convenience, the labels of the spins have been switched so that the pattern characteristic of the Bell states is more clear. Now the ket $ 0000\rangle$ should be interpreted as $ 0\rangle_2 \otimes  0\rangle_3 \otimes  0\rangle_1 \otimes  0\rangle_4$ . One can see that the measurement results in an equal mixture of the four Bell states. For clarity, we zoomed on the sub-matrices along the diagonal to show the Bell states more clearly ( $ \psi^\pm\rangle = \frac{1}{\sqrt{2}}( 00\rangle \pm  11\rangle)$ , $ \phi^\pm\rangle = \frac{1}{\sqrt{2}}( 01\rangle \pm  10\rangle)$ ). . . . . | 63 |
| 4-7 | <b>Entanglement transfer efficiency versus the strength of the measurement.</b> For $\alpha = 1$ the correlation between the simulated $\rho_{out}$ and the theoretical density matrix is equal to 0.93. This value being less than 1 is due to the non perfect experimental input state and to the coherent errors contained in $U_{BellMap}$ . . . . .   | 64 |
| 5-1 | <b>Molecule of 2,3 dibromothiophene with the two protons labeled 1 and 2.</b> The chemical bonds among the atoms are indicated by double parallel lines, and a transparent “dot-surface” used to indicate their van der Waals radii. . . . .   | 71 |
| 5-2 | <b>Redfield kite structure of the relaxation superoperator expressed in the transition basis (TABLE I).</b> The shaded area corresponds to blocks of different coherence order which are effectively decoupled from each other. . . . .  | 73 |

|     |   |    |
|-----|---|----|
| 5-3 | <p><b>Three different estimates of the relaxation superoperator of 2,3 dibromothiophene in the transition basis, indexed as indicated in Table I. (a)</b> Relaxation superoperator obtained from a least-squares fit, without the complete positivity constraint, of the exponential <math>\exp(-i(\underline{\mathcal{H}} + \underline{\mathcal{R}}) t_m)</math> to the propagators <math>\underline{\mathcal{P}}_m</math> at the corresponding times (<math>t_1 = 0.4, t_2 = 0.8, t_3 = 1.6, t_4 = 3.2</math> s) with respect to the symmetric Redfield kite relaxation superoperator matrix <math>\underline{\mathcal{R}}</math>, starting from the results of Richardson extrapolation (see text). <b>(b)</b> The relaxation superoperator obtained from a fit to the same data and with the same starting value of <math>\underline{\mathcal{R}}</math>, but with the complete positivity constraint included in the fit. <b>(c)</b> The relaxation superoperator obtained by assuming that <math>\mathcal{H}</math> and <math>\mathcal{R}</math> commute, and using the average of the estimates obtained by taking the logarithms of the absolute values of the eigenvalues of the propagators over all four time points as the final estimate (see text).</p> | 74 |
| 6-1 | <p><b>Quantum network for the DFS-QEC concatenation scheme.</b> The second physical qubit from the top is the data qubit, while the first physical qubit and the third grouped with the fourth one are the ancillae and the logical ancillae respectively. <math>H_L</math> denotes a logical Hadamard operation [1]. The engineered noise implemented incoherent independent <math>z</math> noise on qubits 1, 2 and 3, in addition to a strong collective <math>z</math> noise on qubits 3 and 4 only.</p>  | 83 |
| 6-2 | <p><b>Pulse sequence for the DFS-QEC scheme.</b> The blocks represent selective one-qubit rotations while the bell-shapes represent magnetic field gradients. Each pulse is a strongly modulating pulse designed to be robust against RF inhomogeneity, and corrected using a feedback loop to counteract systematic errors. The experiment contains 83 pulses, 13 gradient pulses and lasts roughly 130 ms.</p>  | 84 |
| 6-3 | <p><b>Pulses and magnetic field gradients sequence to implement the noise.</b> The black boxes represent <math>\pi</math> pulses. The internal Hamiltonian is thereby refocused while encoding k-space components along different directions for the different qubits. The collective noise was also implemented using a magnetic field gradient in the <math>z</math> direction together with the weak <math>z</math> noise on the third physical qubit, thereby implementing the noise model b. Here <math>T = 35 \mu\text{s}</math>, <math>G_3 = 60 \times 2.6\% G/cm</math>, <math>G_4 = 60 \times 20\% G/cm</math>, and <math>G_1</math> and <math>G_2</math> were calibrated to yield the same attenuations as for <math>G_3</math> given the geometry of the sample (<math>L_z \approx 1.6</math> cm, <math>L_x = L_y \approx 0.5</math> cm) and unequal gradient strengths (<math>G_z^{max} = 60 G/cm</math>, <math>G_x^{max} = G_y^{max} \approx 46 G/cm</math>).</p>  | 85 |

|     |  |    |
|-----|--|----|
| 6-4 | <p><b>Experimental results.</b> The dots correspond to the 3-qubit QEC scenario with independent <math>z</math> noise only while the asterisks correspond to the same scenario but with additional strong collective noise, and <math>k(t) = k_0(t)</math>. The squares correspond to the No QEC scenario and the diamonds to the DFS-QEC scheme. There is an error bar of <math>\pm 0.02</math> for each data point which is not displayed here for the sake of clarity. <b>(a)</b> Entanglement fidelity results (see text for an explanation of the different effects). <b>(b)</b> Average normalized polarization of the output states (see text). . . . .</p> | 87 |
| 6-5 | <p><b>Simulation of the DFS-QEC concatenation experiment.</b> Most of the experimental features, i.e. the "hump" in addition to the drop of the QEC-DFS scenario compared to the QEC alone are reproduced. The "hump" is due to an imperfect initialization of the ancillae (see text for a detailed explanation). The drop mentioned above on the other hand is primarily due to coherent and incoherent errors because of the longer sequence (more pulses) for the QEC-DFS scheme. We add here for clarity that <math>k(t) = k_0(t)</math>. . . . .</p>   | 89 |
| 6-6 | <p><b>Illustration of the "hump" effect (ideal simulation).</b> The maximum correlation for the QEC case is <math>\sim 1.00341</math> as predicted by the analysis. . . . .</p>  | 91 |

# List of Tables

|     |  |    |
|-----|--|----|
| 2.1 | <b>Summary of relevant characteristics for an example set of transformations.</b> The three columns list the pulse duration (in $\mu s$ ), maximum power (in kHz), and the gate fidelity of the simulated pulse. While the maximum power is relatively large, all powers are experimentally feasible. The pulses designed for the crotonic acid sample require longer times and yield lower fidelities due to the decreased chemical shift separation and increase of coupling strengths. . . . .  | 27 |
| 2.2 | <b>Summary of experimental data for the Alanine sample.</b> For each of six $\pi/2$ pulses, the experimentally determined density matrix is compared with the expected result. The first column (No Pulse) confirms that the experimental and expected inputs have almost unit overlap. Each of the other headings denote which spins are rotated by $\pi/2$ . In each case, the projection and attenuated correlation for each pulse is averaged over the three inputs $I_j^1 + I_j^2 + I_j^3$ , for $j = x, y, z$ . Because all pulses are short in comparison to the natural decoherence times, the attenuation gives an indication of the relative significance of the coherent and incoherent errors. Uncertainties arising from errors in the tomographic density matrix reconstruction are of order 1%. . . . . | 37 |
| 3.1 | <b>Summary of experimental results.</b> The metrics $C$ , $A$ , and $C_A$ , refer to the correlation (or projection), attenuation, and attenuated correlation ( $C_A = C \cdot A$ ). The superscripts specify whether the pulses employed were compensated or uncompensated for RF inhomogeneity, while the angle brackets denote that the reported quantities are means over the three input states tested for each transformation. In the case of the spin-rotation values, the quantity reported is the average of all the spin-rotation results. . . . .   | 52 |
| 3.2 | <b>Experimental results of spin-rotation gates.</b> The metrics $C$ , $A$ , and $C_A$ , refer to the correlation (or projection), attenuation, and attenuated correlation ( $C_A = C \cdot A$ ). The superscripts specify whether the pulses employed were compensated or uncompensated for RF inhomogeneity, while the angle brackets denote that the reported quantities are means over the three input states tested for each transformation. The spin-rotation pulses tested were $\pi/2$ and $\pi$ rotations of the carbon spins denoted in the superscript. . . . .  | 53 |

5.1 Table of operators (versus Cartesian basis) of the transition basis used for the density and superoperator matrices, the corresponding matrix indices and their coherence orders (see text). . . . . 72



# Chapter 1

## Introduction

Computers today play a fundamental role in science and industry. During the last few decades, a tremendous increase in the performance of computers has been observed. As a matter of fact, the power of computers has increased exponentially with the number of years, as predicted by Moore's law. The massive increase of computational power represented by contemporary computers is a direct result of the successful drive to build electronic devices on a smaller and smaller scale. When the size of the components approaches atomic dimensions, quantum mechanics becomes an unavoidable factor. This theory has revealed itself to be one of the most successful in the history of science, in spite of many features that defy common sense. Nevertheless, even with so powerful a theory, great obstacles to improve conventional computers will soon arise due to the unavoidable bounds of miniaturization. For this reason, members of the scientific community started to work on improving the capabilities of a computer from a totally different angle.

In the early 1980s, scientists, including Richard Feynman [2], thought about possible schemes to exploit the laws of quantum physics to their rational ends. This led to the idea of a "quantum computer", i.e. a computer whose functional principles would be based on the quantum mechanical laws. Though a functional quantum computer still lies beyond the grasp of current technology, a succession of theoretical and practical advances suggests some heartening progress towards that goal.

In a quantum computer, information is not stored as a string of ones and zeros, but in a quantum mechanical wavefunction, containing information for instance about spin directions or photon polarizations, that can represent superpositions of states. Within this context, the term "bit" is now replaced by "qubit", and the latter quantity can be in the 0 and the 1 state at the same time. Because the quantum dynamics of a system are linear, if a  $n$ -qubit system is prepared in a superposition of  $2^n$  states a quantum computer acting on it will perform  $2^n$  operations, or computations, at once. Research in the field of quantum computing really exploded when Shor published a paper describing an algorithm that would enable the factorization of an integer into primes exponentially faster than the best classical algorithm known so far would [3]. This factorization problem lies in the heart of the RSA cryptographic system, which is used very heavily. This discovery had an enormous impact, given that the security of encryption systems that depend on the difficulty of performing this operation could

someday be compromised. Building a quantum computer however remains a very technically challenging problem, requiring both precise control of a quantum system and isolation from the noisy effects of the environment. These two requirements are some of the main obstacles in the quest for a working quantum computer.

In this context, this thesis addresses some aspects of the different problems encountered in the control of a quantum information processor, namely the coherent control of the quantum system dealing with unitary dynamics only, and then in the presence of incoherent and decoherent noise. We report here a new and original technique based on time-dependent control fields tailored to perform accurate and selective unitary operations on small nuclear spin systems (up to 10). The method is then extended to counteract the main source of incoherence in liquid state nuclear magnetic resonance (NMR) experiments, namely radio-frequency power inhomogeneity (chapter 3). The sequences obtained are modular, i.e. their performance compared to a desired transformation does not really depend on the input state, and their calculated fidelities represent today the state of the art control of homonuclear spins. Simple experiments are reported in order to confirm their performance. Two more sophisticated experiments, namely an entanglement transfer and an entanglement swapping experiment, using 4 qubits are then carried out as benchmarks to illustrate the performance of the technique and its extension (chapter 4). This leads us finally to the final and very important problem of decoherence. Methods based on quantum process tomography (QPT) are developed to acquire further qualitative and quantitative information about the underlying sources of incoherence and decoherence (chapter 5). The latter techniques are furthermore illustrated and tested through the measurement of the noise generators of a two-qubit system. As confirmed by this measurement, one can in general expect in a quantum computer some partial symmetry in the noise process. In chapter 6, we investigate the concatenation of a decoherence-free subspace (DFS) scheme, which counteracts completely the collective part of the noise, with a quantum error correction code which corrects for the remaining part to first order. We thereby report the first experimental concatenation of different quantum information protection schemes. As a whole, this work represents one of the first steps in the development of precise control of quantum information both in the presence of incoherence and decoherence.

# Chapter 2

## Quantum Control

The past decade has seen a substantial interest in improving coherent quantum control. Coherent control has origins in both nuclear magnetic resonance (NMR) [4, 5] and optical spectroscopy [6, 7]. For an overview of advances in both fields, the reader is referred to [8]. Since coherent control's inception, many different techniques have been used both to improve selectivity and to reduce the duration of control pulses. For spin systems, the Fourier transform has been used to approximate the excitation profile in the limit of low power and no spin-spin couplings [9] and more complete analytic solutions have been developed to aid in general pulse design and analysis [10, 11, 12, 13, 14, 15]. Alternatively, very sophisticated shaped pulses have been designed using a variety of computer-aided methods [16, 17] or feedback from system observables [18]. Equivalent analytic theories [19, 20], computer-aided methods [21] and feedback techniques [22, 23] have also been developed by the optics community. Similar techniques are also used in other fields such as the control of trapped ions [24, 25].

The development of liquid-state NMR systems as prototype quantum information processors [26, 27] has enabled experimental demonstration of quantum algorithms [28, 29, 30], quantum error correction [31, 32], and quantum simulations [33]. These experiments built upon well-established spectroscopic techniques developed over the past four decades, such as using low-power (soft) shaped radio-frequency (RF) pulses to obtain selective operations. However, the selective pulses employed to date have the disadvantage that low power implies long duration. This not only introduces errors due to relaxation, or decoherence, but also allows significant evolution under the action of the internal Hamiltonian. In the past, this evolution was rarely of concern because there was little importance placed on implementing a particular operation. For example, in spectroscopy there are entire classes of propagators that selectively excite a single spin from its equilibrium state, but for applications such as quantum computing the transformation must act as expected for all input states.

---

<sup>1</sup>Parts of this chapter were extracted from E. M. Fortunato, M. A. Pravia, N. Boulant, G. Teklemariam, T. F. Havel, and D. G. Cory, "Design of strongly modulating pulses to implement precise effective Hamiltonians in quantum information processing," *Journal of Chemical Physics*, 116:7599-606, 2002.

A second problem with soft-pulse techniques is that selective pulses simultaneously applied to different spins interfere with each other, thus causing significant deviation from the desired action [34]. To address some of these problems, several groups pre-calculate these errors and incorporate corrections into their analysis and pulse design [35, 36]. However, not all errors can be corrected using these techniques<sup>2</sup>, and it would be preferable to average out unwanted evolution by the use of strong control fields, so that no additional corrections are required.

In this chapter, we present a procedure for finding high-power pulses that strongly modulate the system’s dynamics to produce precisely a desired spin-selective unitary propagator. These operations, or gates, allow arbitrary rotations of each spin around independent single-spin axes, while refocusing the internal evolution. They are “self-contained”, in the sense that they can be placed back to back in longer sequences without requiring additional computational resources or post-experiment corrections<sup>3</sup>. By using high-power, pulse durations are decreased by almost an order of magnitude, thereby significantly reducing the effects of relaxation. The simulated gate fidelities of the pulses are high, reaching past 0.9999 on the three-spin system <sup>13</sup>C-alanine placed in a 800 MHz magnet. Finally, the use of strong modulation also allows the incorporation of robustness against slowly varying or time-independent incoherent errors such as those caused by RF inhomogeneities [37, 38, 39]. Our control methods are the first to combine all of these features.

The pulses presented here have been applied in recent Quantum Information Processing (QIP) experiments to demonstrate algorithms [30], study notions of measurement [40], and test new methods for noise control [41]. They promise to be increasingly useful in future NMR QIP experiments, where larger numbers of qubits will necessitate increasing the number of homonuclear spins. In addition, these methods can be adapted to develop improved pulses for selective spectroscopy [42] and imaging [43]. Finally, although presented within the context of NMR, these methods are applicable to any system where the total Hamiltonian is well known and the external degrees of freedom allow for universal control, both requirements of any quantum information processor.

## 2.1 Metrics of Control

In designing gates for controlling quantum information, a metric is required to judge how well a specific implementation compares to the ideal, desired transformation. A metric of a gate’s performance should describe the quality of a general transformation, including the possibility of non-unitary evolution. Unfortunately, such information is not directly accessible by experiment, so we choose a metric comprised only of sets of state measurements. For an input state,  $\rho_{in}$ , the ideal transformation maps the

---

<sup>2</sup>For instance, not all errors can be represented as a composition of phase shifts,  $\sigma_z \otimes \sigma_z$  couplings and ideal  $\pi/2$  or  $\pi$  pulses.

<sup>3</sup>The term “modular” has also been used in the literature to describe such operations

system to a theoretical output state,  $\rho_{th}$ , *i.e.*,

$$\rho_{in} \xrightarrow{U_{th}} \rho_{th}. \quad (2.1)$$

On the other hand, a simulated or experimentally implemented control sequence will produce a different output state,  $\rho_{out}$ , *i.e.*,

$$\rho_{in} \longrightarrow \rho_{out}. \quad (2.2)$$

Noting that  $\rho$  is Hermitian, the projection between these two states, defined as

$$P(\rho_{th}, \rho_{out}) = \frac{\text{trace}(\rho_{th} \rho_{out})}{\sqrt{\text{trace}(\rho_{th}^2) \text{trace}(\rho_{out}^2)}}, \quad (2.3)$$

quantifies how similar in 'direction' the two states are. This metric is analogous to the dot product between two vectors, varying from  $-1$  for anti-parallel states to  $1$  for identical states. A value of zero indicates orthogonal density matrices. In order to account for non-unitary evolution, a second term multiplies the projection yielding the attenuated correlation, namely,

$$C(\rho_{th}, \rho_{out}) = P(\rho_{th}, \rho_{out}) \sqrt{\frac{\text{trace}(\rho_{out}^2)}{\text{trace}(\rho_{in}^2)}} \quad (2.4)$$

$$= \frac{\text{trace}(\rho_{th} \rho_{out})}{\sqrt{\text{trace}(\rho_{th}^2) \text{trace}(\rho_{in}^2)}}. \quad (2.5)$$

The projection and the attenuated correlation serve as metrics for state fidelity.

The gate fidelity,  $F$ , of a transformation is defined as

$$F = \overline{C(\rho_{th}, \rho_{out})}, \quad (2.6)$$

where  $\overline{C}$  represents the average attenuated correlation over an orthonormal set of input density operators (*i.e.*,  $\text{Trace}[\rho_j \rho_k] = \delta_{jk}$ ) that span the Hilbert space. It should be noted that  $F$  is maximized (with a value of one) when the implemented and ideal transformations are the same, and is insensitive to differences in the global phase between the ideal and implemented transformation.

We can derive a useful alternate form for the gate fidelity in terms of the actual and theoretical transformations instead of the input-output state relations. This form is both easier to compute and has intuitive appeal in that knowledge of the transformation can be directly translated to gate fidelities. First we assume that our ideal transformation is unitary, and the implemented transformation is a completely positive, trace-preserving linear map [44]. In other words, the implemented transformation takes density operators to valid density operators. Under these assumptions, Eqns. 2.1 and 2.2 are explicitly given by

$$\rho_{th} = U_{th} \rho_{in} U_{th}^\dagger, \quad (2.7)$$

and

$$\rho_{out} = \sum_{\mu} A_{\mu} \rho_{in} A_{\mu}^{\dagger}, \quad (2.8)$$

where the  $A_{\mu}$  satisfy the trace-preserving condition

$$\sum_{\mu} A_{\mu}^{\dagger} A_{\mu} = 1. \quad (2.9)$$

We now show that the gate fidelity reduces to

$$F = \sum_{\mu} |Trace(U_{th}^{\dagger} A_{\mu})/N|^2, \quad (2.10)$$

where  $N$  is the dimension of the Hilbert space. Using the normalized Pauli basis,  $\sigma_j$ , as the orthonormal input density operators and the cyclic properties of the trace, Eqn. (2.6) becomes

$$F = \sum_{j=1}^{N^2} Tr[(U_{th} \sigma_j U_{th}^{\dagger}) (\sum_{\mu} A_{\mu} \sigma_j A_{\mu}^{\dagger})] / N^2 \quad (2.11)$$

$$= \sum_{j=1}^{N^2} Tr[\sigma_j \sum_{\mu} U_{th}^{\dagger} A_{\mu} \sigma_j A_{\mu}^{\dagger} U_{th}] / N^2. \quad (2.12)$$

Expanding the product of  $U_{th}^{\dagger} A_{\mu}$  in terms of the orthonormal Pauli basis ( $U_{th}^{\dagger} A_{\mu} = \sum_k B_{\mu}^k \sigma_k$ ), yields

$$= \sum_{j\mu} Tr[\sigma_j (\sum_k B_{\mu}^k \sigma_k) \sigma_j (\sum_m B_{\mu}^{m*} \sigma_m)] / N^2 \quad (2.13)$$

$$= \sum_{j\mu km} B_{\mu}^k B_{\mu}^{m*} Tr[\sigma_j \sigma_k \sigma_j \sigma_m] / N^2. \quad (2.14)$$

Because the  $\sigma$  Pauli basis is orthogonal, only terms where  $k = m$  contribute. Therefore, Eqn. (2.14) reduces to

$$F = \sum_{j\mu k} |B_{\mu}^k|^2 Tr[\sigma_j \sigma_k \sigma_j \sigma_k] / N^2. \quad (2.15)$$

If  $\sigma_k$  is not proportional to identity, it will anti-commute with exactly half the  $\sigma_j$  terms in the sum, while commuting with the other half. Therefore, two sets of terms cancel and have no contribution to  $F$ . Defining  $\sigma_1$  to be the element that is proportional to identity, Eqn. (2.15) further reduces to

$$F = \sum_{j\mu} |B_{\mu}^1|^2 Tr[\sigma_j \sigma_j] / N^3 \quad (2.16)$$

$$= \sum_{j\mu} |B_\mu^1|^2 / N^3 = \sum_{\mu} |B_\mu^1|^2 / N. \quad (2.17)$$

This is clearly equal to Eqn. 2.10. Thus, the gate fidelity corresponds to how well the actual transformation reverses the action of  $U_{th}^\dagger$ . In this form it is obvious that the gate Fidelity is independent of which orthonormal basis of input states is used as  $\rho_{in}$ , as long as it has the same properties as the Pauli basis.

## 2.2 Designing Gates for Controlling Quantum Information

In the standard model of quantum computing, an algorithm can be expressed as a series of unitary operations that maps a set of input states to a particular set of output states. The physical implementation of an algorithm requires the use of a quantum system with an Hamiltonian that contains a sufficient set of externally controlled parameters to allow for the generation of a universal set of gates [45]. The task of control is to find a time-dependent sequence of values for these control parameters that modulates the system's dynamics in order to generate a particular gate to the required precision.

Given a control sequence, solving for the effective Hamiltonian is straightforward. Unfortunately, going the other way is much more difficult. That is, finding a RF waveform that produces a propagator with desired properties is an inverse problem. Traditionally, analytic techniques, such as average Hamiltonian theory [5], have been used to determine an appropriate control sequence. With modern computer resources, numerical methods provide a more efficient and accurate solution to this problem.

### 2.2.1 NMR Spin System

As an example, liquid-state NMR is used to demonstrate how to find control sequences to implement particular gates. In NMR, spins in a large static magnetic field (in our case,  $\sim 7$  T) are controlled via external RF pulses. The internal spin Hamiltonian is composed of both Zeeman interactions with the applied field modified by electron screening (chemical shift) and scalar couplings with other spins. Together these provide the QIP requirements of addressability and conditional logic respectively. In terms of spin operators, the internal Hamiltonian is

$$H_{int} = \sum_{k=1}^n \omega_k I_z^k + 2\pi \sum_{j>k}^n \sum_{k=1}^n J_{kj} I^k \cdot I^j, \quad (2.18)$$

where  $\omega_k$  represent the chemical shifts of the spins,  $J_{kj}$  the coupling constant between spins  $k$  and  $j$ , and  $n$  is the number of spins. The test molecules used throughout this document are shown in Fig. 2-1, along with the relevant internal Hamiltonian values.

The external Hamiltonian describing the coupling between the spins and an oscil-

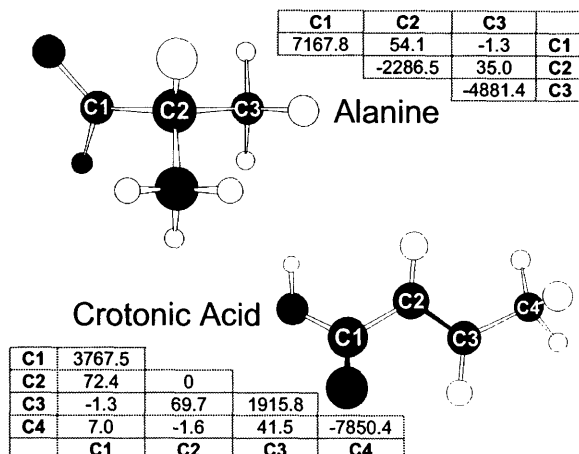


Figure 2-1: **Molecular structure and Hamiltonian parameters for alanine and crotonic acid.** The chemical shift of each carbon nucleus is given in the corresponding diagonal element while the coupling strengths are given by the off-diagonal values. All values are in Hertz, and they were measured in a 300 MHz ( $\sim 7$  T) magnet.

lating RF field generated by a single transmitter is

$$H_{ext}(\omega_{RF}, \phi, \omega, t) = - \sum_{k=1}^n e^{-i(\omega_{RF}t + \phi)} I_z^k \omega I_x^k e^{i(\omega_{RF}t + \phi)} I_z^k, \quad (2.19)$$

where  $\omega_{RF}$  is the transmitter's angular frequency,  $\phi$  the initial phase, and  $\omega$  the power<sup>4</sup>. Of course, additional species can be added by including appropriate terms in  $H_{int}$  and an additional  $H_{ext}$  for each additional RF field.

## 2.2.2 Numerical Search Method

Using this knowledge of the internal Hamiltonian and the form of the external Hamiltonian, the parameter values that generate the desired gate must be determined. Here, a quality factor  $Q = 1 - \sqrt{F}$  is minimized by searching through the mathematical parameter space using the Nelder-Mead Simplex algorithm [46]. While this function has many local minima, the Simplex algorithm often succeeds in finding satisfactory solutions. Our goal is to show that sufficient, implementable control sequences can be found. Finding the optimal solution is much more challenging and based on our system and control parameter values, is not expected to improve pulse performance significantly. We have parameterized the control sequence as a cascade of RF pulses with fixed power, transmitter frequency, initial phase, and pulse duration ( $\tau$ ). As will be seen, this is a particularly convenient and completely general parameterization,

<sup>4</sup>Actually,  $\omega$  equals a spin's nutation rate caused by a RF field. Because this parameter is experimentally controlled by attenuating the RF power, it is commonly referred to as the pulse power.



but we make no claims that it is the only, nor necessarily the best choice. If the RF power is constant over the duration of a pulse, *i.e.*, the pulse's amplitude is square, the total Hamiltonian  $H_{tot} = H_{int} + H_{ext}$  can be made time-independent by transforming into the frame that rotates at the frequency of the transmitter. This allows the Liouville-von Neumann equation of motion to be solved by a single diagonalization. Initially, the starting density matrix is the same in both frames ( $\tilde{\rho}(0) = \rho(0)$ ), so that at the end of the pulse, the density matrix in the new frame is given by

$$\tilde{\rho}(\tau) = e^{-iH_{eff}\tau} \rho(0) e^{iH_{eff}\tau}, \quad (2.20)$$

where  $H_{eff}$  is the effective Hamiltonian in the new frame [47]. Transforming this density matrix back to the original frame gives

$$\rho(\tau) = U_z(\tau)^{-1} e^{-iH_{eff}\tau} \rho(0) e^{iH_{eff}\tau} U_z(\tau), \quad (2.21)$$

where

$$U_z(\tau) = (e^{i\omega_{RF} \sum_{k=1}^n I_z^k \tau}). \quad (2.22)$$

Therefore the transformation in the original rotating frame is given by

$$U_{period}(\tau) = U_z^{-1}(\tau) e^{-iH_{eff}\tau}. \quad (2.23)$$

Because the evolution under the whole sequence is given in the original rotating frame, no additional resources are required to concatenate pulses, nor is any mathematical correction required at the end of an experiment.

Cascading these periods yields the net transformation

$$U_{net} = \prod_{m=1}^N U_z^{-1}(\tau_m) e^{-iH_{eff}^m(\omega^m, \omega_{RF}^m, \phi^m)\tau_m} \quad (2.24)$$

where the index  $m$  refers to the  $m^{th}$  period, *i.e.*, to the  $m^{th}$  square pulse, with a corresponding set of 4 parameters. In other words,  $N$  constant amplitude pulse periods, each with a different transmitter frequency and initial phase, are applied in series. Clearly, a single period is not sufficient to generate an arbitrary transformation; therefore the number of periods is increased until a suitable net transformation is found. Using desktop computing resources, this yields convergence times for three- and four-spin systems that are typically seconds to minutes.

In addition to the desired propagator,  $U_{ideal}$ , an initial set of starting parameters for the pulse shape is required. While this initial guess must be reasonable (*i.e.*, in the vicinity of the solution), many different starting points typically converge to equally deep minima. We have observed that the number of acceptable solutions for this parameterization is very large, allowing experimental implementation issues to be considered. For example, experimental limitations do not allow arbitrarily high powers or frequencies to be implemented. To keep the algorithm from returning infeasible solutions, a penalty function that increases as the parameter value moves towards infeasible solutions is added to the quality factor. Penalty functions are also

used to guide the algorithm towards more favorable pulse solutions. In our case, penalties are placed on high powers, large frequencies, and negative- or long-time periods.

### 2.2.3 Gate Simulations

The methods described above were used to obtain a set of pulses that implement each of a set of important single-spin gates. To study the performance of these gates, propagators for each of the pulses were simulated under different conditions. In the first set of simulations, the pulse performance was calculated for ideal implementations using current experimental conditions. Second, the gate fidelity was simulated as a function of systematic distortions of the pulse parameters. From these results, the relative importance of implementation precision is determined. A final set of calculations showed how a pulse can generate quite different evolutions as the resonance frequency of a test spin is varied over a range of chemical shifts.

#### Ideal Pulse Simulations

Pulses were created for three- ( $^{13}\text{C}$ -labeled alanine) and four- ( $^{13}\text{C}$ -labeled crotonic acid) spin homonuclear systems. The chemical shifts and scalar coupling constants for each of these systems are listed in Fig. 2-1. As a representative set, each of the single spin  $\pi/2$ , and nearest-neighbor paired  $\pi$  pulses were simulated with the relevant characteristics summarized in Table 2.1 and example waveforms shown in Fig. 2-2. The duration of the pulses is on the order of 200  $\mu\text{s}$  for the three-spin system and 420  $\mu\text{s}$  for the four-spin system, both significantly shorter than those that could be obtained using low-power pulses. The average fidelities for each system are 0.9995 and 0.995, demonstrating that, at least under ideal conditions, control sequences that implement the desired transformation with high fidelity can be found.

The ultimate goal of control in quantum computing is to attain fault-tolerant computation. While it has been proven that perfect control is not required [48], estimates of the precision needed vary from 0.9999 to 0.999999 depending on the assumptions used. These simulations predict an achievable level of control that approaches the most optimistic estimates for fault-tolerant computation. As expected, the pulse duration decreases with increasing chemical shifts dispersion (selectivity condition) and, for the case that  $J_{jk} \ll |\omega_k - \omega_j|$ , the fidelity of the sequence decreases with increasing ratio of the couplings (bilinear terms) to chemical shift.

#### Exploring Achievable Fidelities

One of the most important results in QIP is the discovery that indefinite, fault-tolerant computation is possible when the gates used to correct for experimental errors have a fidelity above a certain level [48]. The simulated single-spin gate fidelities of the alanine pulses in Table 2.1 reach the lower end of the threshold, but it is important to explore further what fidelities are achievable (with the present method) in situations with extended experimental capabilities. For this purpose, we extensively explored

| Pulse                       | Time( $\mu s$ ) | Max. Power( $kHz$ ) | Fidelity |
|-----------------------------|-----------------|---------------------|----------|
| <b>Alanine Pulses</b>       |                 |                     |          |
| $\pi/2]_x^1$                | 202             | 7.9                 | 0.9995   |
| $\pi/2]_x^2$                | 221             | 9.3                 | 0.9995   |
| $\pi/2]_x^3$                | 212             | 9.0                 | 0.9995   |
| $\pi/2]_x^{12}$             | 194             | 8.5                 | 0.9995   |
| $\pi/2]_x^{23}$             | 179             | 9.2                 | 0.9995   |
| $\pi/2]_x^{123}$            | 163             | 10.3                | 0.9995   |
| $\pi]_x^{12}$               | 252             | 8.0                 | 0.9996   |
| $\pi]_x^{23}$               | 129             | 10.3                | 0.9997   |
| <b>Crotonic Acid Pulses</b> |                 |                     |          |
| $\pi/2]_x^1$                | 389             | 8.5                 | 0.9930   |
| $\pi/2]_x^2$                | 610             | 4.8                 | 0.9957   |
| $\pi/2]_x^3$                | 392             | 6.3                 | 0.9950   |
| $\pi/2]_x^4$                | 559             | 7.6                 | 0.9923   |
| $\pi]_x^{12}$               | 326             | 9.0                 | 0.9963   |
| $\pi]_x^{23}$               | 315             | 11.3                | 0.9932   |
| $\pi]_x^{34}$               | 345             | 8.4                 | 0.9962   |

Table 2.1: **Summary of relevant characteristics for an example set of transformations.** The three columns list the pulse duration (in  $\mu s$ ), maximum power (in kHz), and the gate fidelity of the simulated pulse. While the maximum power is relatively large, all powers are experimentally feasible. The pulses designed for the crotonic acid sample require longer times and yield lower fidelities due to the decreased chemical shift separation and increase of coupling strengths.

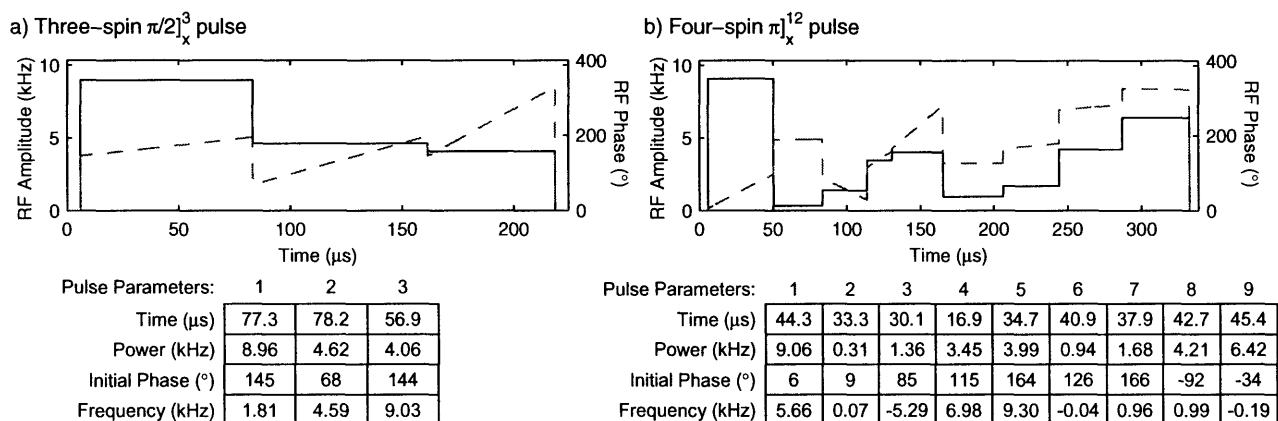


Figure 2-2: **Ideal RF waveform for two example pulses.** The solid (dashed) line is the amplitude (phase) of the waveform. Changes in the transmitter frequency (within a single period) were implemented by a discrete linear phase ramp. The sharp discontinuities occur at the transitions between periods. Substantial filtering of these high frequency components (smoothing of the shape) has little effect on the gate fidelity. In order to experimentally implement the pulse, it is converted into a discrete series of amplitudes and phases (order 1K long) by sampling the ideal waveform at a constant rate. Details of the pulse parameters (as per Eqn. 2.24) are listed below each waveform. Due to experimental implementation issues, a  $6 \mu\text{s}$  period with zero RF power (*i.e.*,  $H_{ext} = 0$ ) is needed before and after the pulse and must be included to produce the desired propagator.

the parameter space of a  $\pi/2_x^2$  alanine pulse by running hundreds of Simplex searches, each time varying the initial guess, the penalty function for the maximum allowable RF, or the magnetic field strength. Fig. 2-3 summarizes the findings. The three curves represent the results for each of three magnetic field strengths tested. The stronger fields allow pulse solutions with higher fidelities because of the increased chemical shift dispersion. The stronger fields cause the spin frequencies to widen, allowing more spectral room for addressability and control. Fidelities also tended to increase with the maximum RF power for values between  $\sim 1 \text{ Hz}$  and  $\sim 10^4 \text{ Hz}$ . At low powers, the RF control is insufficient to average out the internal Hamiltonian, resulting in low fidelities. At high RF control power, the strength of the RF dominates the internal Hamiltonian, resulting in the desired control. The three vertical dotted lines (one for each field) indicate where the smallest chemical shift frequency differences fall relative to the RF power strength. As expected, the sharp increase in the fidelities occurs when the RF power is able to dominate the chemical shift terms in the internal Hamiltonian. The maximum gate fidelity in the plot is close to 0.99999, suggesting that, for the single-spin gate examined, the fault-tolerant limit is potentially achievable.

It is important to emphasize that the maximum achievable fidelities of Fig. 2-3 represent the best gates achieved using the current pulse parameterization and available search method and resources. The results do not preclude other methods

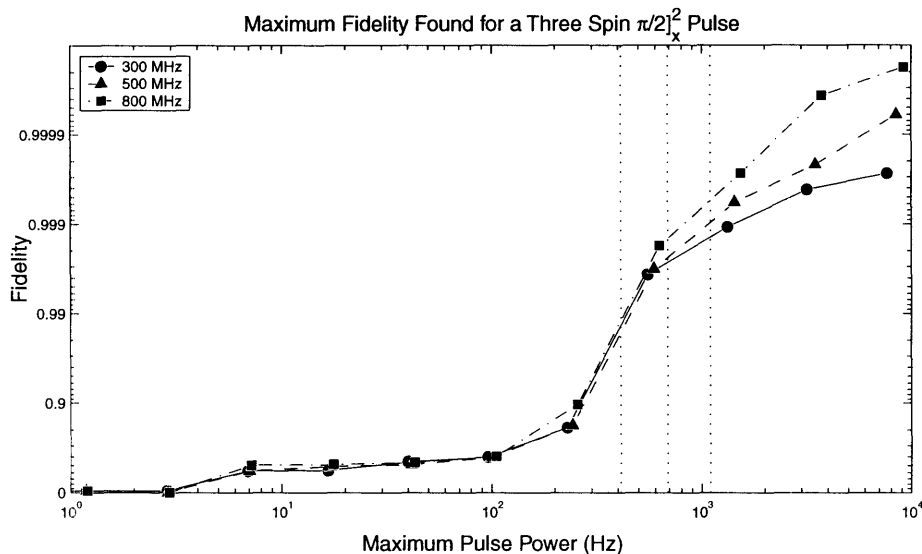


Figure 2-3: **Exploration of achievable fidelities.** The plot shows the maximum fidelities found for a  $\pi/2_x^2$  alanine pulse as allowed RF power and magnetic field strength were varied. The three lines correspond to the magnetic field strengths explored, as denoted by the legend. The dotted vertical lines mark the point of the minimum chemical shift difference at each of the three field strengths. Using ideal experimental control in a 800 MHz magnet, a single-spin gate fidelity reaching 0.99999 is potentially realizable.

and pulse strategies from yielding higher fidelities.

## 2.3 Systematic Errors

The above results demonstrate how knowledge of the internal and the control Hamiltonians can be used to design custom sequences for generating unitary transformations. The fidelities reported are around 0.999 for the typical systems of three and four qubits. It still remains however to estimate how sensitive these solutions are with respect to small errors in the control parameters. The simulations in this section report the robustness of the implemented gates versus some systematic variation or uncertainty of control parameters such as power, phase, time, frequency, chemical shifts etc... Although simulations of the pulses demonstrate that the gates are robust against small deviations in some of the control parameters, a substantial loss of fidelity occurs when the RF amplitudes deviate in a systematic way from the prescribed values, the robustness decreasing with the number of spins. At the end of this section, we describe a feedback procedure that detects and corrects experimental deviations from the ideal RF shapes. The study and the development of tools aimed at counteracting incoherent errors is reported in the next chapter.

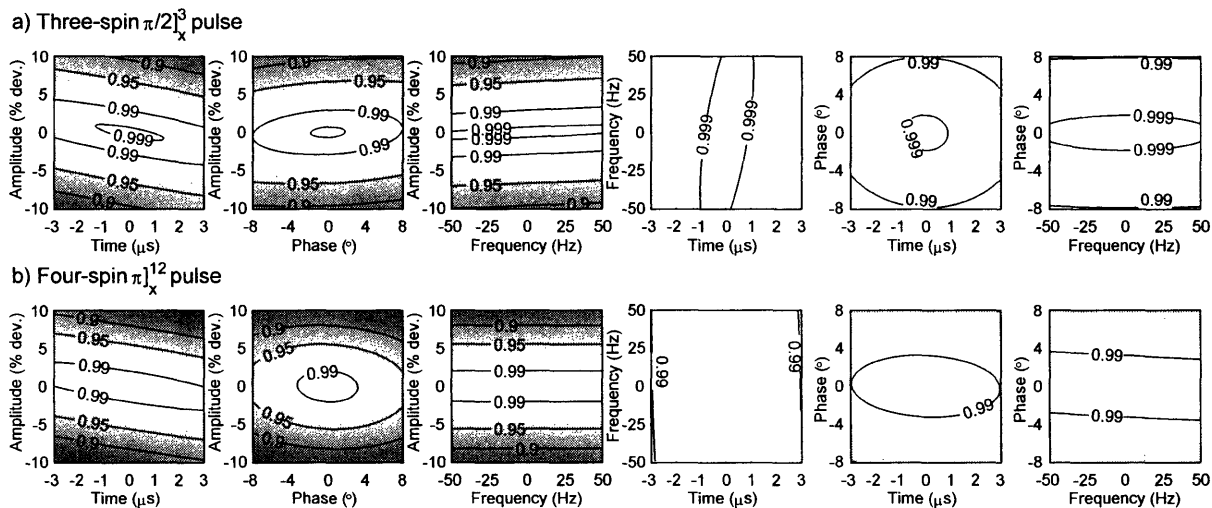


Figure 2-4: Gate fidelity vs. variations in experimental parameters. The experimental parameters were varied over the range of expected errors, demonstrating that both the alanine and crotonic acid pulses are most sensitive to RF amplitude.

### 2.3.1 Variations in the External Hamiltonian

The external RF parameters are determined by a minimization procedure, suggesting that small variations of the external parameters should have little effect on the quality of the pulses. To check this assumption, the gate fidelity was calculated as each of the six pairs of the four control parameters were varied over a range of errors typical of an experimental implementation. As a sample set, one pulse for each of the two systems is presented here. The results shown in Fig. 2-4 demonstrate the natural robustness against typical variations in the initial phase, frequency, and duration of each period.

Clearly, the sequence is most sensitive to power variations. For the pulses listed in Table 2.1, if the power's amplitude is changed by 5% the average fidelity falls to  $0.96 \pm 0.01$  for alanine pulses and  $0.94 \pm 0.04$  for crotonic acid pulses. For the 25 pulses used in [41] the average fidelity at 5% amplitude deviation is  $0.97 \pm 0.02$ . For 10% deviation, the gate fidelity drops to  $0.86 \pm 0.03$  for the alanine pulses and  $0.81 \pm 0.12$  for the crotonic acid pulses. This pulse sensitivity to RF amplitude suggests that RF inhomogeneity may be a leading cause of experimental errors. While techniques to select homogeneous regions are available [36, 49], the loss in signal to noise is significant, especially if multiple coils are used. Instead, because these errors are incoherent in nature, it is possible to design pulse sequences that refocus such inhomogeneities (see chapter 3).

### 2.3.2 Variations in the Internal Hamiltonian

For NMR spectroscopy, the goal is to excite selectively spins in a band of frequencies leaving all other possible spins (with unknown precession frequencies) along the  $z$

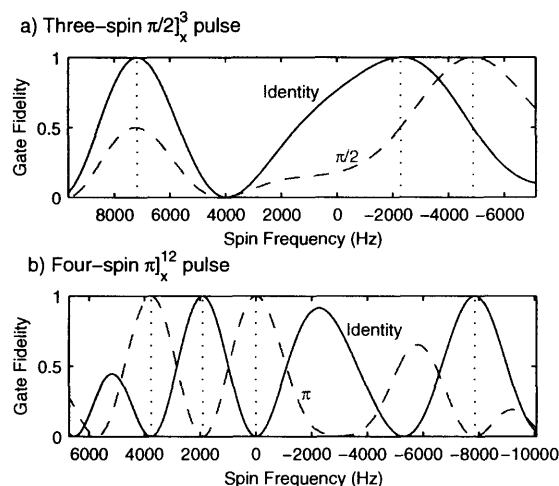


Figure 2-5: **Gate fidelity vs. spin frequency.** The gate fidelities of two example pulses were calculated as a function of the resonance frequency of a test spin. The frequency was varied in the range of chemical shifts of the molecules. The solid (dashed) line is calculated with identity (desired transformation) as the theoretical transformation. The vertical dotted lines denote the actual chemical shifts for each spin. As can be seen, the gate only works when the test spin is at the appropriate resonance frequency.

axis. This requires that the propagator for spins at any other frequency be, at most a phase change. With detailed knowledge of the internal Hamiltonian, the effect of the applied RF field needs only be considered at the resonance frequencies of the chemical species present in the given molecule. By relaxing the requirement that the average Hamiltonian be zero for all chemical shifts other than those in the band of excitation, a RF shape can be found that more efficiently implements the desired gate for the frequencies of concern yielding high-power yet selective pulses. To demonstrate this idea more clearly, the gate fidelities of the two sample pulses considered in this chapter were calculated as a function of a test spin's resonance frequency. As can be seen in Fig. 2-5, the fidelity is close to unity only near the resonance frequency for which the pulse was designed to work.

This stresses the necessity of having accurate knowledge of the system's Hamiltonian. On the other hand, looking at the region immediately around the resonance we see the fidelity falls off quite slowly. This implies that small variations in the chemical shift do not significantly affect the fidelity of the pulses. For example, in the experiments presented below, the unwanted scalar couplings to the hydrogen atoms, which are equivalent to errors in the resonance frequency when these are left untouched, were automatically refocused by the control pulse. It should be noted that no constraint was used to require this robustness, but that it results from the use of strongly modulating pulses. If this natural robustness is not sufficient, additional constraints can be added. However, it was found empirically that the robustness of the pulses versus chemical shift variations decreases as the number of spins increases (unless the

width of the window of resonance frequencies also increases). When considering a single nuclear species coupled with another species via the scalar coupling, this observation suggests the use of dynamical decoupling [50] if the experiment is not too long (it leads otherwise to some nuclear Overhauser enhancement [47]) to average out these undesired couplings.

### 2.3.3 RF Waveform Feedback Correction

In the spectrometer originally used to test these new schemes, a digital waveform generator creates the desired shape. The signal is then amplified and routed to a coil in the probe that is tuned to the carbon resonance frequency ( $\sim 75$  MHz). The sample is inserted in the coil, where it is exposed to the RF irradiation that generates the desired gates. Because of nonlinearities in the transmitter and probe circuits, the waveforms observed by the spins are distorted from the intended shapes. For a set of 25 sample waveforms, the mean absolute deviation between the observed RF amplitudes and the intended amplitudes was about 150 Hz, while the mean phase deviations were comparatively smaller, at about 0.7 degrees. Using Fig. 2-4 as a reference, one can expect that the phase errors cause negligible loss in fidelity. In contrast, the amplitude errors cause the RF nutation rate in each period to vary up to 4 percent for typical alanine pulses, resulting in a significant drop in fidelity. Simulations of alanine gates having errors of this magnitude have fidelities about 0.03 smaller than the fidelities of the ideal transformations, suggesting a need for improved RF shaping.

To correct the amplitude and phase errors, we used an iterative feedback procedure to determine the prewarped RF waveforms that, when distorted through the transmitter chain, would create a RF shape close to the intended shape. The feedback was accomplished by using the hydrogen coil as a spy pick-up antenna to observe the final RF wave transmitted to the sample. The hydrogen resonant circuit was tuned to 300 MHz, and, as a result, it attenuated the 75 MHz carbon signals by about 30 dB. In addition, its response at the low carbon frequencies was expected to be nearly flat for a 1 MHz band around the carbon resonance frequency<sup>5</sup>. Both the attenuation factor and the flat response made the hydrogen coil a useful observation tool for the carbon waveforms. The signals collected from the hydrogen coil were directed to a mixer and finally to a digitizer for measurement.

The digitizer scale was calibrated by measuring the waveforms of pulses with known spin responses. In separate experiments, we applied a series of on-resonance, square pulses with varying power settings. For each pulse, we determined the time necessary to generate a  $4\pi$  rotation on a spin on resonance. We then digitized each pulse using time steps  $\Delta t = 1 \mu s$ . Because each pulse generated a  $4\pi$  rotation, a properly calibrated digitizer scale would result in the total integral of the magnitude of each waveform to equal  $4\pi$ . We made use of this fact to determine the scaling constant  $C_N$  that converted the arbitrary digitizer units into units of angular frequency. Given

---

<sup>5</sup>The probe response of a 400 MHz coil was measured at 100 MHz, and it was found to be very flat. We expected a similar result in the 300 MHz system.



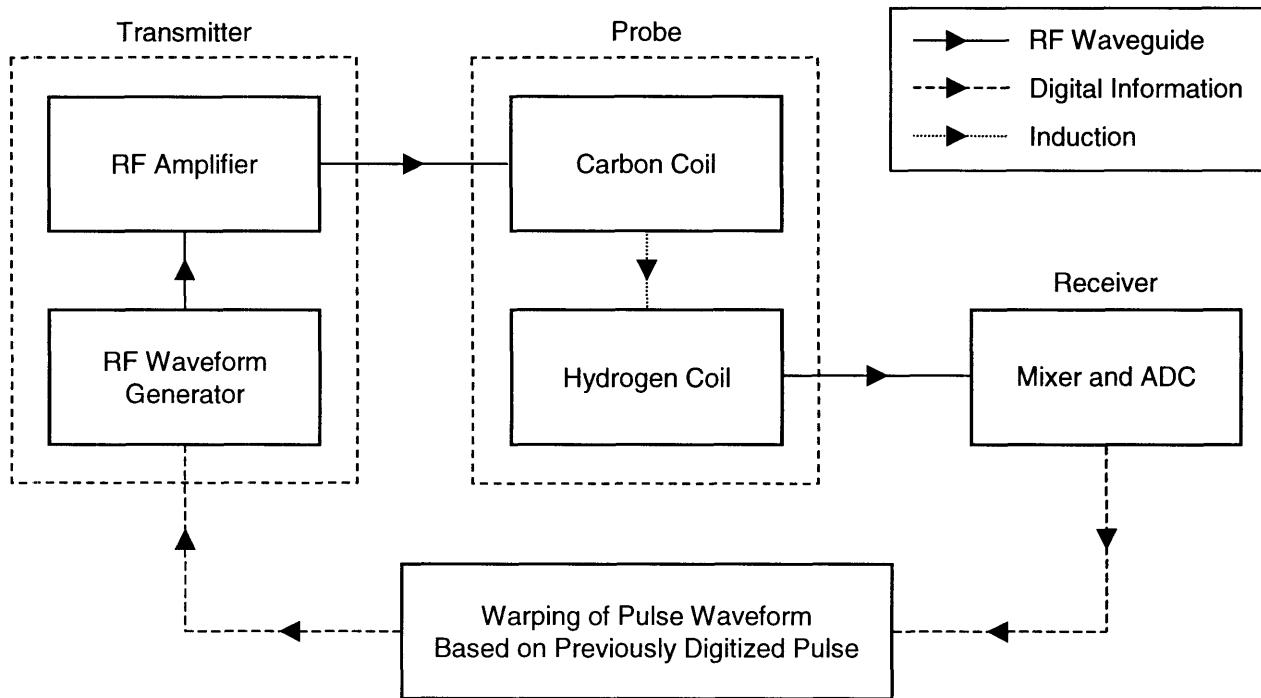


Figure 2-6: **Feedback loop for correcting experimental RF waveforms.** Distorted signals arriving at the carbon coil are detected and digitized through the proton coil. The difference between the measured RF wave and the desired wave is then calculated, resulting in a fixed wave that is then retransmitted to the coil. The loop continues until the shape of the fixed wave produces the desired signal at the carbon coil.

in terms of the digitized values  $d_n$ , the time step  $\Delta t$ , and the chosen rotation angle  $4\pi$ , the scaling constant is

$$C_N = \frac{4\pi}{\sum_n d_n \Delta t} \quad (2.25)$$

and, when multiplied against each digitizer bin value  $d_n$ , converts it to the nutation rate  $w_n = C_N d_n$ <sup>6</sup>. In practice, the scaling constant used for the tested waveforms was the average of the individual constants obtained for a range of calibration power settings. The constants  $C_N$  obtained from pulses with different power settings varied less than 0.2 percent from pulse to pulse. This calibration was carried out each time a new feedback procedure was begun.

The properly normalized scale was then used to analyze all of subsequent digitized waveforms. The feedback loop for a given pulse began by digitizing the RF shape  $\omega_{dig}(k)$  generated at the sample from the input waveform  $\omega_{input}(k)$  specified to the waveform generator. The variable  $k$  denotes the iteration number. For the first

<sup>6</sup>If the RF inhomogeneity profile is known, this is trivially extended to obtain a better estimate of  $C_N$ .

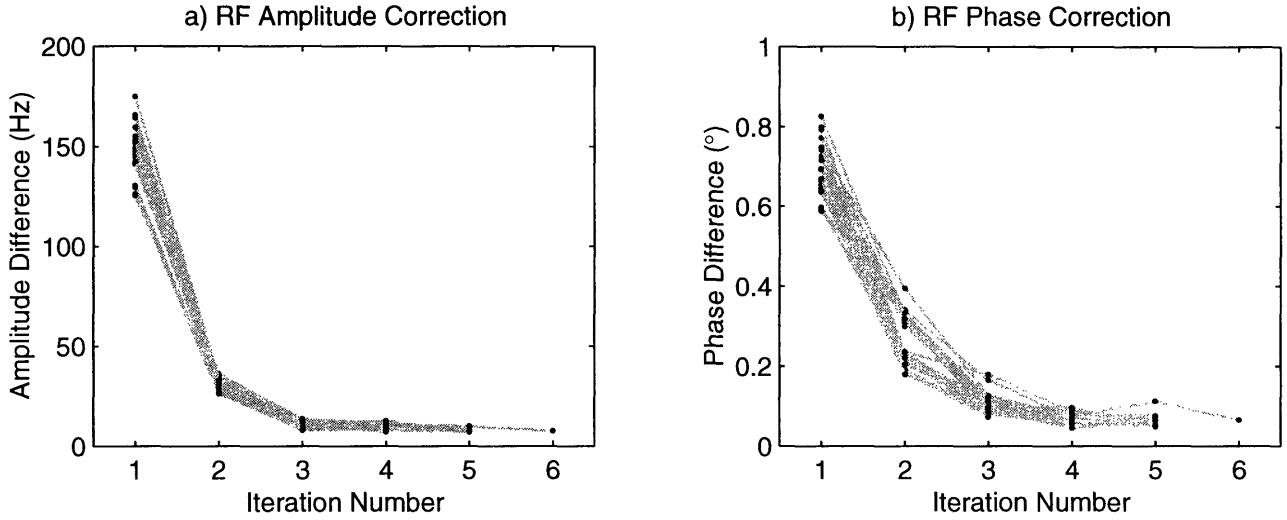


Figure 2-7: **Improvement of errors in digitized RF waveforms.** The errors from a test sample of 25 waveforms are plotted here as a function of the feedback loop iteration number. The errors are the mean absolute differences between fits to the digitized waveform and the ideal waveform. Three to four iterations were typically sufficient to improve the RF shape.

iteration, the input waveform used was the ideal shape. The magnitude and phase of each period in  $\omega_{dig}(k)$  were then fit using low order polynomials, yielding the corresponding fitted waveform  $\omega_{fit}(k)$ . For the magnitude, the order of the polynomial was usually 3, depending on the length of the period, while the phases were fit with a line. The new fixed waveform  $\omega_{fix}(k)$  was constructed by subtracting from the input waveform the difference between the fitted signal  $\omega_{fit}$  and the ideal waveform  $\omega_{ideal}$ , as shown in

$$\omega_{fix}(k) = \omega_{input}(k) - \alpha (\omega_{fit}(k) - \omega_{ideal}). \quad (2.26)$$

The variable  $\alpha$  denotes the fraction of the deviation to subtract into the fixed shape, and it controls the rate of convergence of the feedback loop. We typically employed values ranging from 1/1.3 to 1. The fixed signal  $\omega_{fix}$  was then sent to the waveform generator and the transmitter chain, resulting in the digitized shape for the next loop.

Using the above mentioned values of  $\alpha$ , the iterative scheme typically converged the digitized pulses  $\omega_{dig}(k)$  to the ideal shapes  $\omega_{ideal}$  in two to three steps, as shown in Fig. 2-7. The average difference between the final digitized amplitude and the ideal amplitude was reduced to about 20 Hz, while the average phase difference was reduced to 0.08 degrees. The signal to noise in the digitized signal was the limiting factor. Fig. 2-8 shows the digitized amplitudes of two pulses, both before and after the feedback procedure. The amplitude of the corrected pulse matches very well with the ideal pulse.

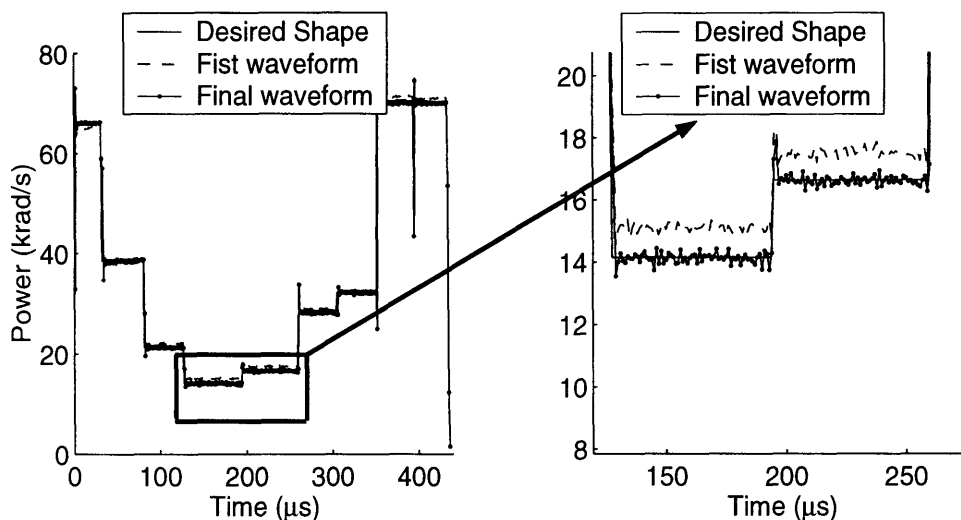


Figure 2-8: **Distorted and corrected RF amplitudes.** The solid line represents the desired shape, while the dashed and dotted-dashed lines correspond to the initial measured waveform and the final one (after two iterations of the feedback code) respectively. The high frequency transients present at the transitions between periods have little effect on the overall performance of the gates.

## 2.4 Experimental Demonstrations

In this section we experimentally demonstrate the efficacy of a representative set of pulses via both spectra and reconstructed density matrices. All experimental tests were carried out on the three carbons of  $^{13}\text{C}$ -labeled Alanine (see Fig. 2-1 for internal Hamiltonian parameters) using a Bruker 300 MHz AVANCE spectrometer.

First, a series of selective single-spin pulses was applied to the thermal state to demonstrate that these selective rotations fully refocus the internal Hamiltonian and so can be concatenated arbitrarily. Fig. 2-9 shows sample sequences and the resulting spectra. In addition, because the internal Hamiltonian is fully refocused, applying selective transformations on different spins sequentially has an effect equivalent to applying all the appropriate transformations to each of the spins simultaneously (neglecting relaxation). With simultaneous, fully self-refocused  $\pi$  pulses, selective couplings can be efficiently implemented using previously published techniques [47, 51], and is demonstrated in Fig. 2-9.

Second, the projection and attenuated correlation between the expected and experimentally determined results of different control sequences were measured for a set of input states. While spectra contain information about the observables of the current state of the system (single-spin transitions in the case of NMR), a single spectrum does not contain enough information to reconstruct the entire state of the system (density matrix). By using readout pulses that rotate different elements of the density matrix into the single-spin transitions, every term of the density matrix can be determined [52]. In our case, seven repetitions of the experiment, each with a

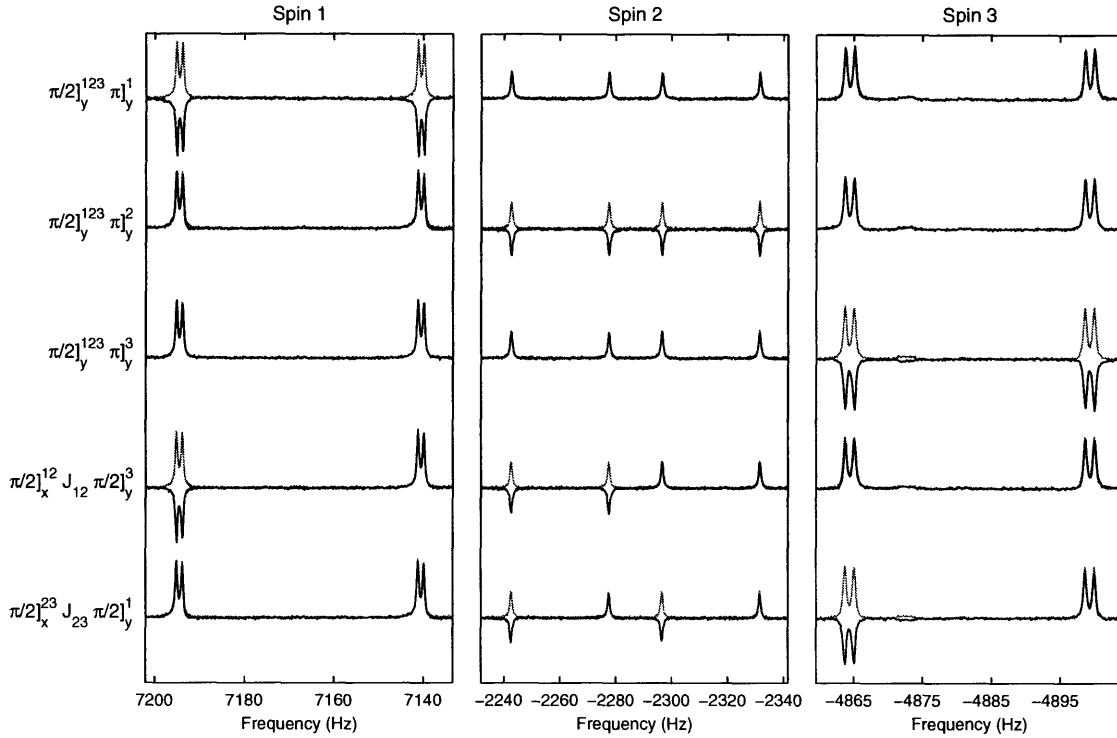


Figure 2-9: **Spectra resulting from different sequences of pulses applied to the thermal equilibrium density matrix**  $\rho_{thermal} = I_z^1 + I_z^2 + I_z^3$ . All sequences are read from left to right. The reference spectra (resulting from a  $\frac{\pi}{2}$  pulse applied to all 3 carbons) is also shown (grey) for reference. Although the chemical shift is of order  $\frac{1}{\tau}$ , no significant phase evolution is seen. Selective coupling sequences are also demonstrated. The phase correction used for all the spectra is strictly the same for all of them and is done such that the reference spectrum ( $\pi/2$  pulse on all the spins at thermal equilibrium) is perfectly absorptive.

different readout pulse, are sufficient to reconstruct the density matrix <sup>7</sup>. Using this method to determine  $\rho_{out}$ , the projections and attenuated correlations, averaged over three different input states, and under the action of six different pulses, are measured and listed in Table 2.2. The input states considered are of the form

$$\rho_{in} = I_j^1 + I_j^2 + I_j^3, \quad (2.27)$$

for  $j = x, y, z$ .

Because the pulses are short with respect to the decoherence times (all greater than 400 ms) the difference between the projection and the attenuated correlation indicates that incoherent evolution (e.g., RF inhomogeneity) has caused significant errors. This is demonstrated by the fact that the ratio of the correlation to the

<sup>7</sup>The seven readout pulses used for density matrix reconstruction are:  $\pi/2]_{y}^1$ ,  $\pi/2]_{y}^3$ ,  $\pi/2]_{x}^3$ ,  $\pi/2]_{y}^{1,2}$ ,  $\pi/2]_{x}^{2,3}$ ,  $\pi/2]_{y}^{1,2,3}$ ,  $\pi/2]_{x}^{1,2,3}$ .

|             | No Pulse | 1     | 2     | 3     | 1&2   | 2&3   | 1&2&3 |
|-------------|----------|-------|-------|-------|-------|-------|-------|
| Projection  | 0.996    | 0.992 | 0.995 | 0.996 | 0.993 | 0.996 | 0.992 |
| Correlation | NA       | 0.977 | 0.985 | 0.986 | 0.975 | 0.984 | 0.986 |
| Attenuation | NA       | 0.985 | 0.990 | 0.990 | 0.982 | 0.988 | 0.994 |

Table 2.2: **Summary of experimental data for the Alanine sample.** For each of six  $\pi/2$  pulses, the experimentally determined density matrix is compared with the expected result. The first column (No Pulse) confirms that the experimental and expected inputs have almost unit overlap. Each of the other headings denote which spins are rotated by  $\pi/2$ . In each case, the projection and attenuated correlation for each pulse is averaged over the three inputs  $I_j^1 + I_j^2 + I_j^3$ , for  $j = x, y, z$ . Because all pulses are short in comparison to the natural decoherence times, the attenuation gives an indication of the relative significance of the coherent and incoherent errors. Uncertainties arising from errors in the tomographic density matrix reconstruction are of order 1%.

projection, or the attenuation, is on the order of the projection (see Table 2.2). This further supports the need to address errors caused by inhomogeneous effects. Robustness to inhomogeneity can be added as a criterion in pulse determination; the additional resource requirements (time, power, etc.) are investigated in the next chapter. Decreases in the coherent errors are also desirable, but such improvements should first be sought through improved experimental implementation. While the goal of fault tolerance clearly hasn't been met, these results indicate that experimental implementation is nearing ideal simulation results.

## 2.5 Conclusion

The ability to implement faithfully a desired unitary transformation is at the heart of any future implementation of a quantum computer. Any control technique should minimize the effects of decoherence while retaining the required addressability. We have demonstrated a method to find control sequences that uses detailed knowledge of the system's Hamiltonian and of experimental imperfections to generate desired gates. The sequences employ high-power pulses that strongly modulate the system's dynamics. These gates are short in duration yet selective, implementing a transformation close to the ideal one. The effect of these control sequences has been simulated under various conditions and experimentally demonstrated by NMR. The unitary behavior is however greatly affected because of incoherent errors that have not yet been taken into account. There is therefore still some room for improvement, which is the subject of the next chapter.



# Chapter 3

## Counteracting Incoherent Errors

Errors in the control of quantum systems may be classified as unitary, decoherent and incoherent. Unitary errors are systematic, and result in a density matrix that differs from the desired one by a unitary operation. Decoherent errors correspond to general completely positive superoperators [53, 54], and can only be corrected using methods such as quantum error correction. Incoherent errors can also be described, on average, by completely positive superoperators, but can nevertheless be corrected by the application of a locally unitary operation that “refocuses” them. They are due to reproducible, slowly varying spatial or temporal experimental control parameters, so that information on the variations is encoded in the system’s spatiotemporal state and can be used to correct them. Here, liquid-state nuclear magnetic resonance (NMR) is used to demonstrate that such refocusing effects can be built directly into the control fields, where the incoherence arises from spatial inhomogeneities in the quantizing static magnetic field as well as the radio-frequency control fields themselves. Using perturbation theory, it is further shown that the eigenvalue spectra of the corresponding completely positive superoperators of the gates exhibit a characteristic spread that contains information on the Hamiltonians’ underlying distribution.

### 3.1 Background

Methods of controlling quantum systems [4, 5, 6, 7, 8] are needed to direct the course of chemical reactions [55, 56], to determine molecular structure [47], and to achieve quantum information processing [54]. The common goal is to preserve or manipulate a quantum system so that the effective evolution over a control sequence is precisely the desired process. The causes of unwanted dynamics include irreversible couplings to the environment (decoherence), static or slowly varying fluctuations in the system’s Hamiltonian (incoherence), and systematic unitary errors. Here, we

---

<sup>1</sup>Parts of this chapter were extracted from M. A. Pravia, N. Boulant, J. Emerson, A. Farid, E. M. Fortunato, T. F. Havel, R. Martinez and D. G. Cory, “Robust control of quantum information,” *Journal of Chemical Physics*, 119:9993-10001, 2003; and from N. Boulant, S. Furuta, J. Emerson, T. F. Havel, and D. G. Cory, “Incoherent noise and quantum information processing,” *Journal of Chemical Physics*, 121:2955-2961, 2004.

examine a common class of experimental imperfections characterized by a spatially or temporally “incoherent variation” in the system’s Hamiltonian. In addition, we describe a method for mitigating this class of errors, and we report an experimental demonstration using liquid-state nuclear magnetic resonance (NMR) techniques [47].

Experimental limitations present an important set of challenges to achieving precise control over quantum systems. Incoherent errors, which are often present in experiments, may be distinguished from decoherent because they are in principle refocusable. In the case of a spatially distributed ensemble interacting with a field, the field amplitude and direction can vary over the ensemble so that the ensemble average dynamics becomes a convex sum of spatially distinct unitary processes. The ensemble’s dynamics will in general appear non-unitary, but as long as the correlation between the spins’ location and the strength/direction of the field remains unchanged the dispersion in the dynamics can be refocused, at least in principle.

Spatially incoherent errors have been a recurring topic of interest in the field of NMR, where they arise as inhomogeneities in the static and radio-frequency (RF) fields involved. The spatially incoherent evolution caused by the inhomogeneities dephases the spins in the NMR ensemble, attenuating and rotating the final state away from the desired state. Past methods of refocusing incoherent evolution have been directed mainly towards achieving rotations of specific states rather than implementing a desired unitary operation on all possible states. Examples include “composite pulses” [57, 58, 59, 60, 61], which have played an important role in creating the robust RF pulse sequences used for spin inversion, spin excitation, and decoupling. Adiabatic pulses have also been used to overcome the problem of RF inhomogeneity [62, 63]. It should also be added that Tycko and Jones have also found very robust sequences that work regardless of the input state [59, 64]. However, these studies either consider collective rotations on a system of spins or individual (non selective) dynamics on the Bloch sphere. Average Hamiltonian methods [5] have also been applied to create pulse sequences that depend mostly on phase changes in the RF fields to control the spins, making the RF field’s amplitude a less important experimental parameter [49]. Most of this work has been devoted to designing robust one-spin operations, but more recently the work has been extended, in the context of quantum information processing, to include two-spin operations [65].

Here, we extend our previously described method in the previous chapter for creating RF control gates in liquid-state NMR quantum information processing experiments [26, 27, 66, 67]. We incorporate information about the main source of incoherence in the numerical optimization and obtain modulation pulses that are robust over the entire distribution and thus yield the desired transformation with even higher fidelity.



## 3.2 Modeling, Measurement and Analysis of Incoherent Processes

In quantum information processing, the central experimental goal is to efficiently generate any desired unitary operation on a quantum system. Unitary operations are realized by manipulating externally-controlled parameters in the system's Hamiltonian. The problem of finding the appropriate external parameters, however, is an inverse problem, and analytical solutions are not available except for the simplest cases. As described in the previous chapter, we can utilize the more easily solved forward problem in a numerical search for a control field modulation that solves the inverse problem, at least in small Hilbert spaces. The density matrix evolution under an incoherent process appears to evolve in a larger space with a continuum of parameters, denoted by  $\vec{r}$ , describing the variations over the ensemble. In NMR,  $\vec{r}$  would be the spatial location of the individual molecules. Every measurement is an integral over  $\vec{r}$ , so assuming that the local initial density matrix  $\rho(\vec{r})$  is uncorrelated with the local unitary operation  $U(\vec{r})$ , the ensemble-average density matrix  $\rho_{in} = \int \rho(\vec{r}) d\vec{r}$  evolves in Hilbert space as

$$\rho_{out} = \int U(\vec{r}) \rho_{in} U^\dagger(\vec{r}) d\vec{r} \quad (3.1)$$

The variation of the operator  $U(\vec{r})$  is tied to the variation of a field in the corresponding Hamiltonian. The evolution can be expressed in matrix form as a superoperator acting on Liouville space [68], i.e.

$$|\rho_{out}\rangle = \int (\bar{U}(\vec{r}) \otimes U(\vec{r})) d\vec{r} |\rho_{in}\rangle \quad (3.2)$$

where  $|\rho\rangle$  is the columnized density matrix (obtained by stacking its columns on top of each other from left to right),  $\bar{U}$  is the complex conjugate of  $U$  and “ $\otimes$ ” is the Kronecker product of the matrices [47, 68]. In this form, it is clear that the input state  $|\rho_{in}\rangle$  is transformed by the non-unitary superoperator

$$S = \int p(\alpha) \bar{U}(\alpha) \otimes U(\alpha) d\alpha, \quad (3.3)$$

where  $p(\alpha)$  is a probability density, i.e. the fraction of quantum systems within an ensemble that sees a given  $U(\alpha)$  within an interval  $d\alpha$  and  $\int p(\alpha) d\alpha = 1$ . This decomposition of a completely positive (CP) map into unitary Kraus operators is sometimes called a random unitary decomposition (RUD) [69]. A RUD exists for an incoherent process, but such a decomposition is sometimes possible even for a very general decoherent process [70] when there is no correspondence between the unitary operators in the decomposition and some actual distribution of associated experimental control parameters  $\alpha$ . The distinction between the two therefore is practical, and depends primarily on the correlation time of the variation of experimental parameters. If the latter quantity is longer than the inverse of the typical modulation

frequency, the process falls into the class of incoherent noise [37, 38]. The point of making this distinction is that, whilst correcting for decoherent errors requires the full power of quantum error correction, in practice incoherent noise effects are often reduced directly through the design of the time-dependence of the control fields. This is possible since the operators underlying the incoherence  $U(\alpha)$  are assumed to be time-independent over the length of the expectation value measurement.

### 3.2.1 Incoherent Processes in NMR Spectroscopy

In the specific case of liquid-state NMR, the task of quantum control is to determine the RF pulse sequence that modulates the internal spin Hamiltonian of every molecule to generate a desired evolution. The internal Hamiltonian for a molecule containing  $N$  spin 1/2 nuclei is

$$H_{int} = \sum_{k=1}^N -\gamma_k(1 - \sigma_z^k)B_0(\vec{r})I_z^k + 2\pi \sum_{j>k}^N \sum_{k=1}^N J_{kj}I^k \cdot I^j, \quad (3.4)$$

where  $-\gamma_k(1 - \sigma_z^k)B_0(\vec{r})$  represents the chemical shift frequency of the  $k$ th spin ( $\gamma$  is the gyromagnetic ratio and  $\sigma_z$  is the shielding constant),  $J_{kj}$  is the scalar coupling constant between spins  $k$  and  $j$  and  $I_i$  denotes the  $i$  axis spin angular momentum operator. The chemical shifts are functions of space because the main magnetic field is never perfectly homogeneous throughout the sample. The scalar coupling constants, however, are independent of location since they depend only on molecular bonding.

The corresponding experimentally-controlled RF Hamiltonian is

$$H_{ext}(t) = \sum_{k=1}^N -\gamma_k f(\vec{r}) B_{RF}(t) e^{-i\phi(t)I_z^k} I_x^k e^{i\phi(t)I_z^k}, \quad (3.5)$$

where the time-dependent functions  $B_{RF}(t)$  and  $\phi(t)$  specify the applied RF control field, while  $f(\vec{r})$  reflects the RF field strength distribution over the sample. Here, we assume that only phase changes in time are important and drop the spatial dependence of  $\phi$ .

Excluding decoherence, the evolution generated by the above Hamiltonians between time 0 and  $\tau_f$  is

$$U_{gate}(\vec{r}) = \mathcal{T} e^{-i \int_0^{\tau_f} (H_{int}(\vec{r}) + H_{ext}(\vec{r}, t)) dt}, \quad (3.6)$$

where  $\mathcal{T}$  is the Dyson time-ordering operator. The goal is to determine a function  $B_{RF}(t)$  and  $\phi(t)$  that results in a net evolution that at every location is close to the desired transformation. In general, this inverse problem is difficult to solve but the forward problem of evaluating  $U_{gate}$  is readily solved numerically for small spin systems.

To efficiently calculate  $U_{gate}(\vec{r})$ , several simplifications can be made. First, the use of shim controls allows the static magnetic field homogeneity to be made less

than 1 part in  $10^8$  over the sample volume, meaning that the resonance frequencies of magnetically equivalent spins differ by the same amount. To confirm our expectations, we did a simulation of the three spin system of alanine under a strongly modulating pulse and with a 5 Hz variation of chemical shifts [71]. The simulations returned two Kraus operators, the norm of the most important one being  $10^6$  times larger than the norm of the other one, proving a behavior very close to unitary. As a result, for now we will drop the spatial dependence of  $B_0$ ; the major problem is the RF field variations in  $H_{ext}$ . We have shown previously that in the fully coherent case strongly modulating RF pulses with piecewise constant RF amplitudes provide an easily computed modulation sequence with sufficient control over the spins. The evolution of a single pulse with constant (in time) RF power  $B_{RF}$ , phase  $\phi$ , frequency  $\nu_{RF}$ , and of duration  $\tau$ , can be solved with one frame transformation and a single diagonalization in that frame. This simplification allows the net propagator of a train of  $M$  such square pulses to be written as

$$U_{gate} = \prod_{m=1}^M U_z^{-1}(\nu_{RF,m}, \tau_m) e^{-iH_{eff}^m(B_{RF,m}, \nu_{RF,m}, \phi_m)\tau_m} \quad (3.7)$$

where  $U_z^{-1}(\nu_{RF,m}, \tau_m)$  executes the rotating-frame transformation of the  $m$ th period and  $H_{eff}$  is the effective, *time-independent* Hamiltonian in the new frame of reference [47]. Using the standard simplex search algorithm, a set of parameters which match  $U_{gate}$  to a desired transformation can often be obtained. In the coherent case, we found the dynamics of these pulses to be very rich, admitting many different strongly-modulating pulses for a given ideal unitary gate. Here we extend this solution to the case of incoherent processes in the control Hamiltonian.

Radio-frequency power inhomogeneity was incorporated into the parameter search by tabulating a discrete histogram of the RF power variations. This distribution of RF power defines a Kraus operator sum [53, 54] instead of the unitary transformation of Eqn. 3.7, namely

$$\rho_{out} = \sum_k A_k \rho_{in} A_k^\dagger, \quad (3.8)$$

where  $A_k = \sqrt{p_k} U_k$  and  $p_k$  is the fraction of the ensemble that undergoes a unitary transformation  $U_k$ . The operators  $U_k$  were evaluated using Eqn. 3.7, and they differ only in the RF amplitudes involved. In NMR spectrometers, the frequency and duration of the pulse do not vary as a function of position, and although the absolute phase does, this phase is unobservable there since the same RF coil is used for both transmission and reception.

The RF inhomogeneity of our experimental setup was measured using a spin nutation experiment in which the transverse magnetization of the spin system was measured after on-resonance pulses of increasing duration. The power spectrum of nutation frequencies (Fig. 3-1) is a direct measure of the distribution of RF field strengths over the sample. The inclusion of RF inhomogeneity in the calculation of the fidelity increases the required computational resources per iteration by a factor equal to the number of intervals used to define the distribution. Hence for the design of the pulses there only 9 intervals were used, and this distribution is superimposed

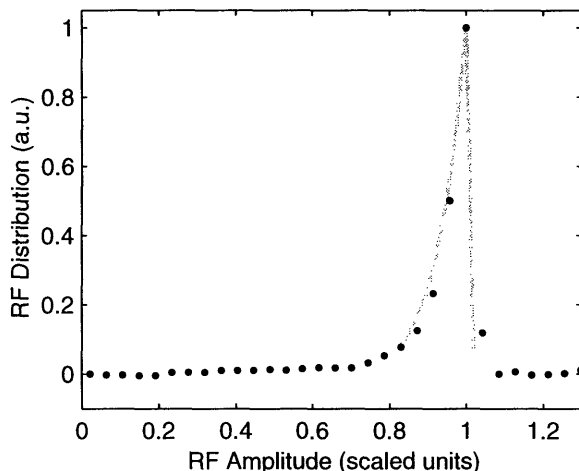


Figure 3-1: **Radio-frequency inhomogeneity profile.** The RF inhomogeneity in the carbon channel was measured using a spin nutation experiment. The resulting decaying signal was Fourier transformed to distill the various RF nutation frequencies present in the sample. The dotted line is the plot of the Fourier transformation, and it is the measured RF inhomogeneity profile. The solid gray line is the profile that was used to design pulses compensated for RF inhomogeneity, and it was extracted from the measured profile.

on the experimental measurement in Fig. 3-1 (gray line).

### 3.2.2 Designing Pulses That Compensate for RF Inhomogeneity

The spatial incoherence of the RF amplitude, or RF inhomogeneity, in NMR is a consequence of the need for high sensitivity, which necessitates wrapping the RF coil tightly around the sample. As a result, different parts of the NMR sample feel unequal RF fields, causing a dephasing of the spins that attenuates the signal and introduces errors in the rotations of the spins. The problem can be avoided by using smaller parts of the sample (and thus less signal). An alternative, however, is to take advantage of the reproducibility of the field strength distribution so as to design gates that are insensitive to these errors.

We used the methods of section 3.2 to search for both compensated and uncompensated modulation sequences for 11 single qubit transformations. The calculations were performed for the three-spin system consisting of the  $^{13}\text{C}$ -nuclei in isotopically-enriched alanine. Fig. 3-2 summarizes the simulated fidelities for the resulting gates. Each fidelity point on the left of Fig. 3-2 was calculated for a unitary gate having a single RF field strength. Each curve traces the gate fidelity as a function of the deviation from the ideal RF field strength. The plot shows that the compensated pulses are significantly less sensitive to changes in the RF modulation strength. The uncompensated pulses, however, have the overall highest fidelities when the RF amplitude

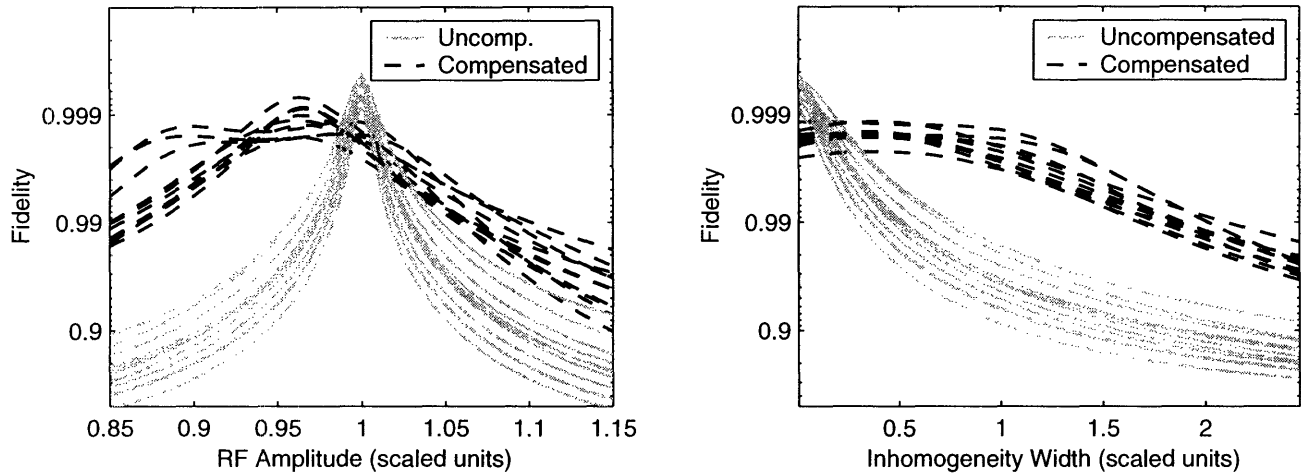


Figure 3-2: **Simulations of compensated and uncompensated pulses as a function of radio-frequency strengths and distribution widths.** The dashed lines correspond to compensated pulses, while the solid gray lines denote uncompensated pulses. The left plot shows how the compensated pulses maintain high fidelities even when the RF strength is scaled from the ideal value. The plot on the right simulates the same pulses as a function of the scaled width of the RF inhomogeneity profile. These results demonstrate the improved fidelity of the compensated pulses for all but the narrowest RF distributions. At the small widths, the RF profile would no longer be inhomogeneous, eliminating the need for the compensated gates.

is at its optimum value. This fact is confirmed in the more realistic situation where a spectrum of RF frequencies is present. The plot on the right of Fig. 3-2 graphs the pulse fidelities for the non-unitary transformations generated with RF distributions of varying widths. The distributions used were stretched or narrowed versions of the measured RF profile (Fig. 3-1), and the widths have been rescaled such that a value of 1.0 corresponds to the experimentally measured RF profile.

### 3.3 Eigenvalue Spectra of Superoperators

In this section, we present a numerical study of the action of both compensated and uncompensated gates by looking at the eigenvalue spectrum of the superoperators of the gates. We will show how the eigenvalues of the superoperators can serve as a useful and convenient tool for extracting information about the imperfections in the implementations of unitary transformations. In particular, we shall describe features of the eigenvalue spectrum that allow us to characterize the distribution of incoherent processes in the superoperators, so that the reduction of these features in our simulated superoperators provides further evidence for the closer-to-unitary behavior of compensated gates as compared to uncompensated ones. Last but not least, the analysis suggests the use of eigenvalue spectra of superoperators as an

intuitive approach to identify symmetries in incoherent and decoherent processes <sup>2</sup>.

### 3.3.1 Perturbation Analysis of Superoperator Eigenvalue Spectra

Let  $n$  be the number of qubits, and  $U_k$  denote the unitary operator generated by the RF field in the  $k$ th frequency interval of the RF amplitude profile. The eigenvalues of the superoperator  $S = \bar{U}_k \otimes U_k$  are products of the eigenvalues of  $\bar{U}_k$  with those of  $U_k$ . This yields  $2^n$  eigenvalues that are equal to unity and  $(2^{2n-1} - 2^{n-1})$  pairs of eigenvalues  $(\lambda, \bar{\lambda})$ . In general, the eigenvalues of CP superoperators come in conjugate pairs <sup>3</sup>, but only in the case of unitary superoperators do all the eigenvalues lie on the complex unit circle.

The incoherent process resulting from an inhomogeneous distribution of  $U_k$  processes is given by the superoperator  $S = \sum_k p_k \bar{U}_k \otimes U_k$ , where  $p_k$  is the fraction of spins that sees the unitary evolution  $U_k$ . The more broadly the  $\{p_k\}$  are distributed, the larger the degree of inhomogeneity in the evolution, and the more incoherent noise enters into the evolution. Estimates of the actual eigenvalues of  $S = \sum_k p_k \bar{U}_k \otimes U_k$  will now be obtained using non-degenerate first-order perturbation theory. Because the RF pulses are not perfect, even in the absence of RF field inhomogeneity, we may assume that the unperturbed eigenvalues are generically non-degenerate. The unitary operator  $U_k$  generated by the RF field acting at position  $k$  may be written in exponential form as  $U_k = e^{-iH_k t}$  where  $H_k$  represents the effective Hamiltonian of the evolution over the period  $t$  for which the pulse is applied ( $\hbar$  has been set equal to 1). Defining  $H_0$  to be the unperturbed (and desired) Hamiltonian, the eigenvalues  $\phi_j$  and eigenstates  $|\phi_j\rangle$  of  $H_0$  satisfy the eigenvalue equation

$$U_0|\phi_j\rangle = e^{-i\phi_j t}|\phi_j\rangle, \quad (3.9)$$

where  $U_0 = \exp(-iH_0 t)$ . The Hamiltonian of a particular  $U_k$  is assumed to be a perturbation of the desired, homogeneous Hamiltonian

$$H_k = H_0 + K_k, \quad (3.10)$$

where  $K_k$  is the perturbation. To first order, the new eigenvalues of  $H_k$  are

$$\tilde{\phi}_{j,k} = \phi_j + \langle \phi_j | K_k | \phi_j \rangle, \quad (3.11)$$

and the corresponding eigenvalues of  $U_k$  are

$$U_k|\tilde{\phi}_{j,k}\rangle = e^{-i\tilde{\phi}_{j,k} t}|\tilde{\phi}_{j,k}\rangle. \quad (3.12)$$

---

<sup>2</sup>The depolarization channel for instance has a simple eigenvalue structure and is easy to identify. An effective depolarizing behavior has thereby been observed experimentally in a three qubit QFT superoperator [72].

<sup>3</sup>This is easily seen by noticing that  $\bar{S} = \sum_k A_k \otimes \bar{A}_k$  (where  $\{A_k\}$  are Kraus operators) is related to  $S$  by a unitary operation.

Although  $S$  is not a normal matrix, i.e.  $[S, S^\dagger] \neq 0$ , to first order it can be considered to have the following spectral decomposition

$$S = \sum_{k,m,j} p_k \left( e^{i\tilde{\phi}_{m,k}t} |\phi_m\rangle\langle\phi_m| \otimes e^{-i\tilde{\phi}_{j,k}t} |\phi_j\rangle\langle\phi_j| \right) \quad (3.13)$$

and the eigenvalues of  $S$  are given approximately by

$$\begin{aligned} \lambda_{jm} &= \sum_k p_k e^{-i(\tilde{\phi}_{j,k} - \tilde{\phi}_{m,k})t} \\ &= e^{-i(\phi_j - \phi_m)t} \sum_k p_k e^{-i(\langle\phi_j|K_k|\phi_j\rangle - \langle\phi_m|K_k|\phi_m\rangle)t}. \end{aligned}$$

We now imagine the scenario where  $K_k$  is given by  $K_k t = \frac{\omega_k - \omega_0}{\omega_0} K$ . This result would in fact be exact for one spin on resonance. In this case,  $\frac{\omega_k - \omega_0}{\omega_0}$  is the parameter  $\alpha$  defined in the introduction (which parameterizes the inhomogeneity) and represents the normalized RF power deviation from the desired power  $\omega_0$ . Defining  $\Delta\omega = \frac{\omega_k - \omega_0}{\omega_0}$  and  $K_{jm} = \langle\phi_j|K|\phi_j\rangle - \langle\phi_m|K|\phi_m\rangle$ , the previous equation in the continuous limit becomes

$$\lambda_{jm} = e^{-i(\phi_j - \phi_m)t} \int p(\Delta\omega) e^{-iK_{jm}\Delta\omega} d\Delta\omega. \quad (3.14)$$

We see in this case that to first order the eigenvalue  $\lambda_{jm}$  is just the unperturbed eigenvalue  $e^{-i(\phi_j - \phi_m)t}$  times the Fourier transform of the RF distribution profile evaluated at  $K_{jm}$ . This result demonstrates that the probability distribution profile  $p(\Delta\omega)$  of an incoherent process can be determined, within some degree of approximation, from the eigenvalue structure  $\{\lambda_{jm}\}$  of an experimental superoperator, given some model for the incoherence  $K$  (see [73] for the inverse problem of finding the RF profile from the eigenvalue spectra of superoperators). Knowing  $K$  would indeed allow one to build the correspondence between  $\lambda_{jm}$  and  $K_{jm}$ , and then to determine  $p(\Delta\omega)$  by performing an inverse Fourier transform. Of course, this result holds for general  $K$  only when the perturbation is in the first order regime, and when the unperturbed eigenvalues are non-degenerate. But if  $K$  approximately commutes with  $H_0$ , then the first-order perturbation in the eigenvalues is close to an exact correction, and the above analysis gives a very accurate description of the incoherent process.

### 3.3.2 Eigenvalue Spectra for Uncompensated Pulses

We now use the result of the previous section, to calculate the first-order eigenvalues of an uncompensated  $\frac{\pi}{2}$  pulse that rotates the alanine carbon spins 1 and 2 about the  $x$ -axis. Fig. 3-3 compares the numerically exact eigenvalues with the results from the approximation. The dots are the eigenvalues corresponding to the full simulation of the gate under the influence of the experimental RF inhomogeneity profile. The crosses are the eigenvalues computed by first-order perturbation theory. To calculate

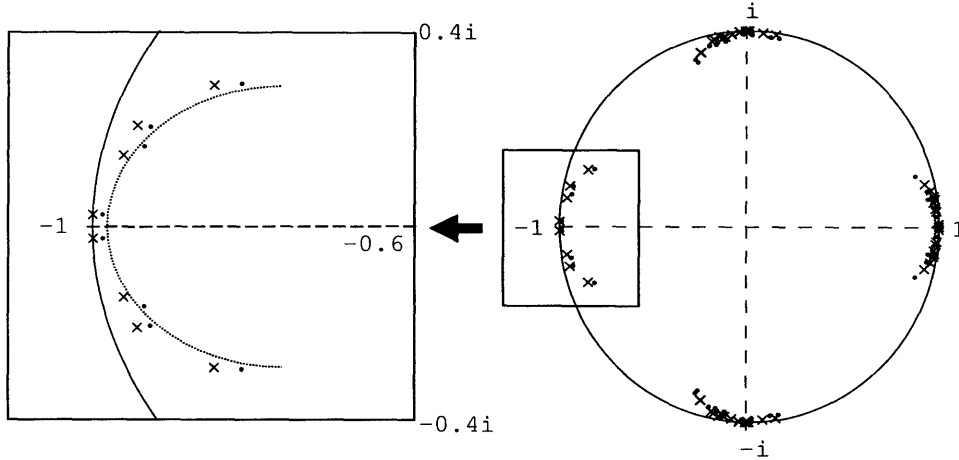


Figure 3-3: **Eigenvalue spectrum of the simulated superoperator for a test gate and the radio-frequency inhomogeneity profile shown in Fig. 3-1.** The dots are the exact eigenvalues of  $S$  while the crosses are the ones obtained by using the first order perturbation analysis. The zoom box shows some of the detail in the left-hand side of the plot. The additional trend line drawn in the zoomed plot emphasizes the fact that the larger the phase shift, the larger the attenuation.

$\lambda_{jm}$ , we first determined  $K_k$  using

$$\begin{aligned} K_k &= i \times (\log(U_k) - \log(U_0))/t \\ &= H_k - H_0 \end{aligned}$$

where  $\log$  is a logarithm of the matrix obtained from the principal branch and then used Eqn. 3.14.

Fig. 3-3 also shows an interesting relationship between the phase shift and the attenuation of the eigenvalues, i.e. the larger the phase shift from the nearly ideal eigenvalues (obtained from  $U_0$ ), the larger the attenuation. This could have been anticipated from the Fourier transform relation found previously. This behavior therefore indicates mainly low frequency components in the RF inhomogeneity profile.

To gain further understanding about the estimation of the eigenvalues of  $S$ ,  $K_k$  can be expanded in the basis of products of Pauli spin matrices and the matrix elements contributing to the perturbation theory analysis can be determined. As an example, let us consider a one-spin system. In this case,  $K_k$  can be expanded in terms of  $\sigma_x$ ,  $\sigma_y$  and  $\sigma_z$ . If we take  $H_0 t = \frac{\pi}{4} \sigma_x$ , then we see that any operator in the expansion of  $K_k$  that anticommutes with  $\sigma_x$  results in zero diagonal matrix elements in the eigenbasis of  $\sigma_x$

$$\begin{aligned} A\sigma_x + \sigma_x A = 0 &\Rightarrow \langle \pm | A\sigma_x + \sigma_x A | \pm \rangle = 0 \\ &\Rightarrow \pm 2 \langle \pm | A | \pm \rangle = 0 \end{aligned} \tag{3.15}$$



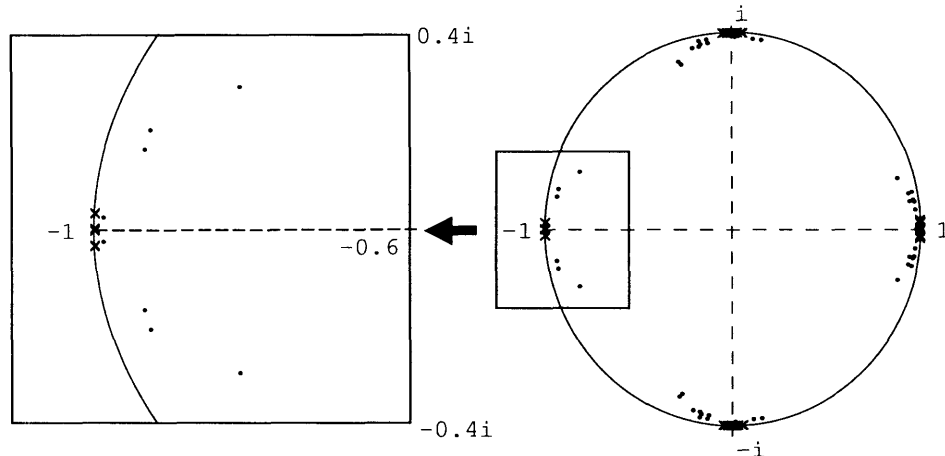


Figure 3-4: **Eigenvalue spectrum of the simulated superoperators corresponding to a compensated and uncompensated pulse.** The dots correspond to the uncompensated gate, while the crosses correspond to the compensated one. Note that the crosses basically lie on the unit circle while the dots are spread inside, confirming the closer-to-unitary behavior of the compensated gates.

where  $|\pm\rangle$  denote the eigenstates of  $\sigma_x$ , and  $A$  is an operator in the decomposition of  $K_k$  that anticommutes with  $\sigma_x$ . In this simple example, only the component along  $H_0$  in  $K_k$  yields a non-zero contribution in the eigenvalue calculation given above ( $I$  is not present either since the operation must be in  $SU(2)$ ). In our three-spin system, if  $H_0 t = \frac{\pi}{4}\sigma_x^1$ , it follows that out of the 64 possible operators in the expansion of  $K_k$  only  $\sigma_x^1$ ,  $\sigma_i^2$ ,  $\sigma_j^3$ ,  $\sigma_i^2\sigma_j^3$ ,  $\sigma_x^1\sigma_i^2$ ,  $\sigma_x^1\sigma_j^3$  and  $\sigma_x^1\sigma_i^2\sigma_j^3$  (or linear combinations of them) will give a nonzero contribution, where  $i, j = x, y$  or  $z$ . In general, the number of operators that yield a non-zero contribution for a  $2^n$  by  $2^n$  unitary operator  $U$  is  $2^n - 1$ , i.e. the number of diagonal elements minus 1 (the identity part). This quick analysis reveals to some extent the slight discrepancy we have between the first order perturbation theory results and the fully simulated ones. Due to the nature of our physical system, the first order perturbation approach takes into account only a small number of elements in the decomposition of  $K_k$ . However, because it captures the general distribution of the eigenvalue spectrum, we can conclude that a significant amount of the perturbation is contained in these few operators.

### 3.3.3 Eigenvalue Spectra for the Compensated Pulses

As described in the previous sections, pulses that are compensated for RF inhomogeneity result in an overall operation closer to being unitary than for uncompensated pulses. In Fig. 3-4, we compare the eigenvalue spectra of the superoperators corresponding to a compensated and uncompensated  $\frac{\pi}{2}$  pulse about the  $x$  axis on the alanine spins 1 and 2.

In general, a unitary superoperator in the Zeeman basis [68], acting on columnized

density matrices  $|\rho\rangle$ , which is trace-preserving and completely positive must correspond to a unitary process in Hilbert space, and can be written as  $\bar{U} \otimes U$  (Boulant, not published). Since the superoperator of an incoherent process can be written as a trace-preserving Kraus operator sum, it must be completely positive and hence is physically reasonable. Thus the fact that the eigenvalues of the superoperators that were simulated for the compensated pulses basically lie on the unit circle provides further evidence about their correspondence to unitary processes in Hilbert space.

### 3.3.4 Symmetric Inhomogeneity Profile

As a final test for our analysis and the validity of our assumptions, we calculated the superoperators where a symmetric inhomogeneity profile is present. We recall the previous formula

$$\begin{aligned}\lambda_{jm} &= e^{-i(\phi_j - \phi_m)t} \sum_k p_k e^{-i(\langle \phi_j | K_k | \phi_j \rangle - \langle \phi_m | K_k | \phi_m \rangle)t} \\ &= e^{-i(\phi_j - \phi_m)t} \sum_k p(\Delta\omega_k) e^{-iK_{jm}(\Delta\omega_k)}\end{aligned}\quad (3.16)$$

where  $K_{jm}(\Delta\omega_k) = (\langle \phi_j | K_k | \phi_j \rangle - \langle \phi_m | K_k | \phi_m \rangle)t$  and  $\Delta\omega_k = \frac{\omega_k - \omega_0}{\omega_0}t$ . Now because  $p(\Delta\omega_k)$  is symmetric with respect to 0, one can see that the additional assumption of  $K_{jm}(-\Delta\omega_k) = -K_{jm}(\Delta\omega_k)$  (as we did previously in this section) leads to the result that  $\lambda_{jm} = e^{-i(\phi_j - \phi_m)t} A_{jm}$  where  $A_{jm}$  is a real number smaller than 1. In other words, in the case of a symmetric inhomogeneity profile, and provided the above assumption is valid, the eigenvalues simply get attenuated, and are not phase shifted. As one can see in Fig. 3-5, for a symmetric profile, the eigenvalues have practically the same phase as when there is no RF inhomogeneity and are simply attenuated by the real factor  $A_{jm}$ . This provides further evidence that the new eigenvalues are correlated with the Fourier transform of the inhomogeneity profile, since the Fourier transform of an even and real function is real.

## 3.4 Simple Experimental Demonstrations

The experimental tests were carried out on the three carbons of  $^{13}\text{C}$ -labeled alanine using a 300 MHz Bruker AVANCE spectrometer (see previous chapter for the internal Hamiltonian's parameters). The experiments tested compensated and uncompensated versions of seven different spin-rotation pulses, which were then used to selectively evolve the two scalar couplings  $J_{12}$  and  $J_{23}$  while refocusing the other couplings<sup>4</sup>. These pulses were applied to the three input states

$$\rho_{in} = I_j^1 + I_j^2 + I_j^3, \quad (3.17)$$

---

<sup>4</sup>The waveforms of all the pulses were corrected using the RF feedback procedure described in chapter 2, reducing distortions caused by amplifier nonlinearities in the experimental setup.

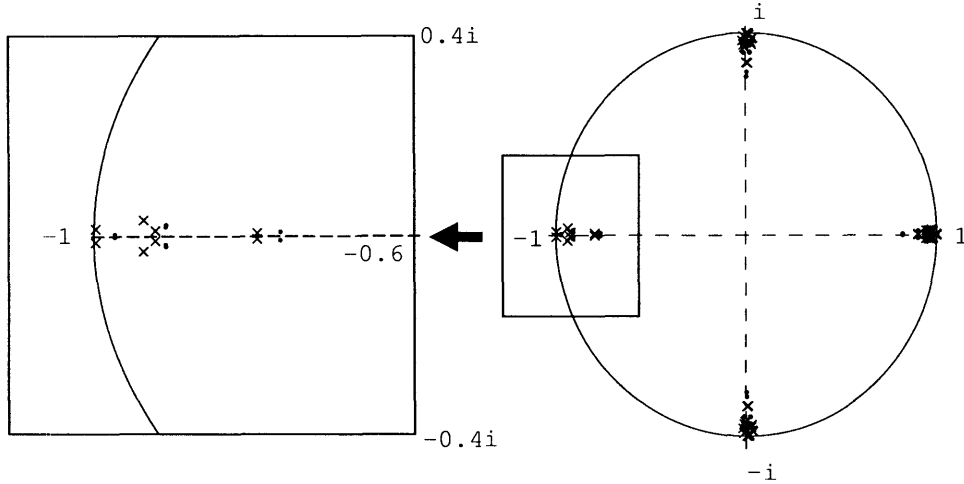


Figure 3-5: **Eigenvalue spectrum of the simulated superoperator for the symmetric radio-frequency inhomogeneity profile.** The dots are the unperturbed eigenvalues and the crosses are the ones computed by using first order perturbation theory. The symmetry in the distribution mainly results in some attenuation of the eigenvalues with no phase shift. The zoom box allows more detail to be seen for the eigenvalues close to  $-1$ .

where  $j = x, y, z$ . The input states were created using compensated or uncompensated pulses, depending on the type of gate being tested. For each gate tested, the average over the three input states was calculated and is shown in Tables 3.1 and 3.2. Table 3.1 shows the results for the input states, the states obtained by selective coupling, and an average over all the single-pulse experiments, while Table 3.2 shows the specific results for each single-pulse experiment.

The input and output density matrices were measured using state tomography and were used to evaluate the correlation  $C$ , attenuation  $A$ , and attenuated correlation  $C_A$  ( $C_A = C \cdot A$ ) given by

$$C(\hat{\rho}_{ideal}, \hat{\rho}_{out}) = \frac{\text{trace}(\hat{\rho}_{ideal} \hat{\rho}_{out})}{\sqrt{\text{trace}(\hat{\rho}_{ideal}^2) \text{trace}(\hat{\rho}_{out}^2)}}, \quad (3.18)$$

$$C_A(\hat{\rho}_{ideal}, \hat{\rho}_{out}) = C(\hat{\rho}_{ideal}, \hat{\rho}_{out}) \sqrt{\frac{\text{trace}(\hat{\rho}_{out}^2)}{\text{trace}(\hat{\rho}_{in}^2)}} \quad (3.19)$$

$$= \frac{\text{trace}(\hat{\rho}_{ideal} \hat{\rho}_{out})}{\sqrt{\text{trace}(\hat{\rho}_{ideal}^2) \text{trace}(\hat{\rho}_{in}^2)}}. \quad (3.20)$$

where  $C$  goes from  $-1$  to  $1$  and represents the directional cosine between the two density matrices and the extra factor in  $C_A$  accounts for the loss of magnetization. In all cases, the result of state tomography on the thermal state  $I_z^1 + I_z^2 + I_z^3$  was used as the reference for the attenuation ( $\rho_{in}$  in Eqn. 3.19). State tomography [52] employs readout pulses to rotate unobservable elements of the density matrix into observable

| Control Metrics                 | Input State | Average over Seven Spin-Rotation Gates | Selective $J_{12}$ Gate | Selective $J_{23}$ Gate |
|---------------------------------|-------------|--|-------------------------|-------------------------|
| $\langle C^{comp.} \rangle$     | 0.993       | 0.991                                  | 0.986                   | 0.990                   |
| $\langle C^{uncomp.} \rangle$   | 0.995       | 0.995                                  | 0.975                   | 0.988                   |
| $\langle A^{comp.} \rangle$     | 0.998       | 0.987                                  | 0.954                   | 0.994                   |
| $\langle A^{uncomp.} \rangle$   | 0.970       | 0.949                                  | 0.951                   | 0.930                   |
| $\langle C_A^{comp.} \rangle$   | 0.991       | 0.979                                  | 0.941                   | 0.984                   |
| $\langle C_A^{uncomp.} \rangle$ | 0.965       | 0.944                                  | 0.927                   | 0.919                   |

Table 3.1: **Summary of experimental results.** The metrics  $C$ ,  $A$ , and  $C_A$ , refer to the correlation (or projection), attenuation, and attenuated correlation ( $C_A = C \cdot A$ ). The superscripts specify whether the pulses employed were compensated or uncompensated for RF inhomogeneity, while the angle brackets denote that the reported quantities are means over the three input states tested for each transformation. In the case of the spin-rotation values, the quantity reported is the average of all the spin-rotation results.

single-spin transitions. For the three-spin alanine system used there, eight repetitions of the experiment, each with a different readout pulse, were used to reconstruct the density matrix <sup>5</sup>.

To determine the actual experimental gate performed, however, one requires knowledge about the effect of the gate on a complete set of input states so that the full superoperator can be determined, a procedure called quantum process tomography [74, 75, 76, 77]. To carry out process tomography for a single alanine gate requires state tomography of the input and output density matrices for a set of 64 linearly independent inputs. Thus full process tomography for one gate would involve  $2 \times 64 \times 8 = 1024$  separate experiments. While this is certainly possible, it is quite laborious. For this reason we limited ourselves to performing state tomography on just the three input states and the corresponding output states described above. The results do not fully characterize the experimental transformations, but they provide a reasonable estimate of the quality of the gates. The most notable difference between the results for compensated and uncompensated gates is in the severe attenuation caused by RF inhomogeneity on the uncompensated gates. The average attenuation value  $A_{comp.}$  for the spin rotations is nearly four times closer to unity than the corresponding value for normal pulses (i.e.  $(1 - A_{uncomp.})/(1 - A_{comp.}) = 3.92$ ). In addition,  $A_{comp.}$  for the  $J_{23}$  coupling is more than 10 times closer to unity than  $A_{uncomp.}$ , although  $A_{comp.}$  for  $J_{12}$  is only slightly higher than  $A_{uncomp.}$ . The correlations for

<sup>5</sup>The eight readout transformations used for the density matrix reconstruction were: identity,  $\pi/2]_y^1$ ,  $\pi/2]_y^{12}$ ,  $\pi/2]_x^{23}$ ,  $\pi/2]_y^3$ ,  $\pi/2]_x^3$ ,  $\pi/2]_x^{1,2,3}$ ,  $\pi/2]_y^{1,2,3}$ . All of the density matrices discussed in this section were acquired using the eight readouts, with the exception of the input states, which used only the last seven. The last seven readouts alone are also sufficient, but we included the identity because of its particularly simple implementation.

| Metrics                         | $\pi/2]_x^1$ | $\pi/2]_x^3$ | $\pi/2]_x^{12}$ | $\pi/2]_x^{23}$ | $\pi/2]_x^{123}$ | $\pi]_x^{12}$ | $\pi]_x^{23}$ |
|---------------------------------|--------------|--------------|-----------------|-----------------|------------------|---------------|---------------|
| $\langle C^{comp.} \rangle$     | 0.991        | 0.992        | 0.991           | 0.986           | 0.994            | 0.993         | 0.992         |
| $\langle C^{uncomp.} \rangle$   | 0.996        | 0.994        | 0.996           | 0.994           | 0.996            | 0.995         | 0.995         |
| $\langle A^{comp.} \rangle$     | 0.990        | 0.989        | 0.987           | 0.988           | 0.986            | 0.984         | 0.986         |
| $\langle A^{uncomp.} \rangle$   | 0.954        | 0.953        | 0.948           | 0.951           | 0.942            | 0.952         | 0.941         |
| $\langle C_A^{comp.} \rangle$   | 0.981        | 0.981        | 0.978           | 0.974           | 0.980            | 0.977         | 0.979         |
| $\langle C_A^{uncomp.} \rangle$ | 0.950        | 0.948        | 0.944           | 0.945           | 0.938            | 0.947         | 0.936         |

Table 3.2: **Experimental results of spin-rotation gates.** The metrics  $C$ ,  $A$ , and  $C_A$ , refer to the correlation (or projection), attenuation, and attenuated correlation ( $C_A = C \cdot A$ ). The superscripts specify whether the pulses employed were compensated or uncompensated for RF inhomogeneity, while the angle brackets denote that the reported quantities are means over the three input states tested for each transformation. The spin-rotation pulses tested were  $\pi/2$  and  $\pi$  rotations of the carbon spins denoted in the superscript.

the compensated rotation gates averaged 0.991, slightly but consistently below the average of 0.995 for the uncompensated gates. The attenuated correlations for the compensated gates, however, were higher than the corresponding values for normal pulses, and the difference was caused by the sharp differences in the attenuations. The results confirm that incorporating RF inhomogeneity into the pulse design can yield more robust gates and narrows the gap between the experimental implementation and the simulation results.

### 3.5 Conclusion

In this section, we explored the capabilities of numerically-determined strongly modulating pulses to achieve high gate fidelities in the presence of a common variety of experimental imperfections. In particular, we showed that robustness against incoherent errors such as RF field inhomogeneity can be obtained when knowledge of these errors is incorporated into the pulse design process. The basic ideas used, i.e. strong modulation, numerical pulse-design procedures, and the incorporation of incoherent errors in these procedures, are likely to find broad applicability in the development of quantum information processing devices based in many diverse physical systems.



# Chapter 4

## Experimental Benchmarks

We report in this chapter two experimental benchmarks on a four-qubit liquid state nuclear magnetic resonance quantum information processor aimed at testing the techniques developed in the previous chapters. In both cases, partial or full pseudo-pure entangled states were created and full state tomography was performed at the key different steps. In the first case, i.e. for the entanglement transfer, entanglement was just transferred using swap gates while in the second case, i.e. for the entanglement swapping, it was transferred via a measurement of a two qubit subsystem in the Bell basis. Roughly eighteen months separated these two experiments. The second one, while more complex, yields higher correlations and therefore provides experimental evidence for the improvement in coherent control.

### 4.1 Entanglement Transfer Experiment

Entanglement is one of the most striking features of quantum mechanics and a key requirement for many procedures in QIP. Entangled pairs of particles are usually obtained by having both particles emerging from a common source, or bringing them together and letting them interact in a tightly controlled fashion [78]. It has recently been demonstrated that entanglement can be teleported from one pair of photons to another when the quadruple contains two singlet states among disjoint pairs [78]— an effect which has been argued to show that quantum correlations are as nonlocal as the quantum states themselves [79]. The experiment reported here demonstrates the dynamics of entanglement transfer by a relatively simple liquid-state NMR experiment, in which two swap operations from the two qubits of a (pseudo-pure [80, 81]) Bell state to two other qubits are performed. Despite its simplicity, this form of transfer provides a means of shuttling data between quantum memory (with long decoherence time) and a fast processor (capable of applying a universal set of gates), thereby

---

<sup>1</sup>Parts of this chapter were extracted from N. Boulant, E. M. Fortunato, M. A. Pravia, G. Teklemariam, D. G. Cory, T. F. Havel, “Entanglement transfer experiment in NMR quantum information processing,” *Physical Review A*, 65:024302, 2002; and N. Boulant, K. Edmonds, J. Yang, M. A. Pravia, and D. G. Cory, “Experimental demonstration of an entanglement swapping operation and improved control in NMR quantum-information processing,” *Physical Review A*, 68:032305, 2003.

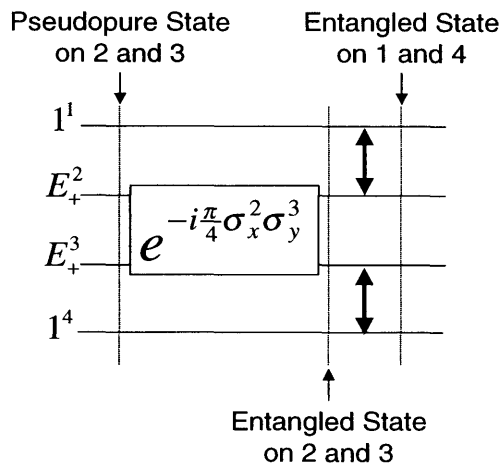


Figure 4-1: **Logical network for the entanglement transfer experiment.** The four spins are represented by the four horizontal control lines, where each line is labelled on the left by the input state superscripted by the spin's index (where “1” indicates that the spin is depolarized and  $E_+$  indicates that it was part of the pseudo-pure state). The pseudo-pure ground state on spins 2 and 3,  $\rho_{pp}^{23} \leftrightarrow |00\rangle\langle 00|$ , is converted by an entanglement operation on the same spins to obtain  $\rho_{Ent}^{23} \leftrightarrow \frac{1}{2}(|00\rangle + |11\rangle)(\langle 00| + \langle 11|)$ . This state is then transferred to spins 1 and 4 by using swap gates.

simplifying the programming of a quantum computer in a fashion similar to that proposed with the aid of quantum teleportation [82]. An overview of the experiment is given in Fig. 4-1. From an information point of view, it consists of initializing two bits (or qubits) out of four in a fiducial state, entangling them, and finally transferring this entanglement to the two remaining ones via two swap gates.

This demonstration was carried out on a liquid-state NMR quantum information processor [83, 80], using the four  $^{13}\text{C}$  nuclei in a sample of crotonic acid (Fig. 4-2) as the qubits. Because liquid-state NMR deals with a highly mixed ensemble of spin systems (molecules) in thermal equilibrium, the state of which can always be described by an ensemble of unentangled systems [81], the experiment described here does not depend on the existence of entanglement in the individual molecules. Nevertheless, the use of pseudo-pure states provides a macroscopic representation of exactly the same unitary dynamics to which the microscopic systems are subject [26, 27]. Pseudo-pure states can be created by introducing an incoherent interaction into the spin dynamics, usually by means of magnetic field gradients. The thermal equilibrium density matrix for four spins in the high temperature limit [84], given by

$$\rho_{eq} \approx \frac{I}{2^4} + \frac{\hbar\beta}{2 \cdot 2^4} \sum_{k=1}^n \omega_k \sigma_z^k, \quad (4.1)$$



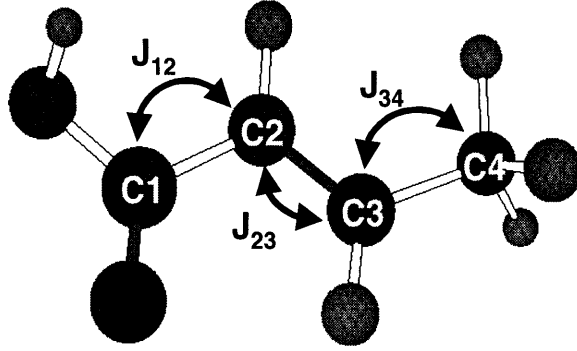


Figure 4-2: Molecule of crotonic acid.

can thereby be transformed into a pseudo-pure ground state

$$\rho = \frac{1 - \epsilon}{2^n} I + \epsilon |0000\rangle\langle 0000|, \quad (4.2)$$

where  $\beta = 1/k_B T$  is the Boltzmann factor,  $\omega_k$  are their chemical shifts,  $I$  is the identity matrix and  $\sigma_z^k$  is a Pauli matrix for the  $k$ th spin.

With decoupling of the protons, the internal spin Hamiltonian of crotonic acid in the weak coupling limit is

$$H_{int} = \pi \left( \sum_{k=1}^4 \nu_k \sigma_z^k + \frac{1}{2} \sum_{\ell=k+1}^4 \sum_{k=1}^4 J_{k\ell} \sigma_z^k \sigma_z^\ell \right). \quad (4.3)$$

The chemical shifts,  $\nu_k$ , are in a 300 MHz magnet 3767.5, 0, 1915.8 and  $-7850.4$  Hz for carbons 1, 2, 3 and 4, respectively, while the coupling constants are  $J_{12} = 72.4$  Hz,  $J_{13} = 1.4$  Hz,  $J_{14} = 7.0$  Hz,  $J_{23} = 69.7$  Hz,  $J_{24} = 1.6$  Hz and  $J_{34} = 41.5$  Hz. The  $T_1$  relaxation times for the carbons are all greater than 2 s, while the  $T_2$  times are longer than 500 ms. The experiments were performed on a Bruker AVANCE 300 MHz spectrometer, using strongly modulating pulses optimized to implement all the single spin rotations required with relatively high speed and precision while simultaneously refocusing evolution under the internal Hamiltonian. Returning to Fig.4-1, the states created at each of the steps indicated will be denoted by  $\rho_{pp}^{23}$ ,  $\rho_{Ent}^{23}$ ,  $\rho_{Ent}^{14}$  and are given explicitly by

$$\begin{aligned} \rho_{pp}^{23} &= \lambda I + \epsilon \sum_{a,b=0}^1 |a00b\rangle\langle a00b|, \\ &= \lambda I + \epsilon (|0000\rangle\langle 0000| + |0001\rangle\langle 0001| + |1000\rangle\langle 1000| \\ &\quad + |1001\rangle\langle 1001|), \\ \rho_{Ent}^{23} &= \lambda I + \frac{\epsilon}{2} \sum_{a,b=0}^1 (|a00b\rangle + |a11b\rangle)(\langle a00b| + \langle a11b|), \end{aligned}$$

$$\rho_{Ent}^{14} = \lambda I + \frac{\epsilon}{2} \sum_{a,b=0}^1 (|0ab0\rangle + |1ab1\rangle)(\langle 0ab0| + \langle 1ab1|).$$

where  $\lambda = \frac{1-\epsilon}{2^n}$ . Here and throughout, the computational basis  $|0\rangle$  and  $|1\rangle$  corresponds to the spins being aligned parallel or anti-parallel to the z-axis. Once the pseudo-pure state was created, the subsequent pulse sequences were:

$$\begin{aligned} P_{Ent}^{23} &= \left[\frac{\pi}{2}\right]_{-x}^3 - \left[\frac{\pi}{2}\right]_y^2 - \left[\frac{1}{2J_{23}}\right] - \left[\frac{\pi}{2}\right]_{-y}^2 - \left[\frac{\pi}{2}\right]_x^3, \\ P_{SWAP}^{12,34} &= \left[\frac{\pi}{2}\right]_x - \left[\frac{1}{2J}\right] - \left[\frac{\pi}{2}\right]_{-x} - \left[\frac{1}{2J}\right] - \left[\frac{\pi}{2}\right]_{-y} \\ &\quad - \left[\frac{1}{2J}\right] - \left[\frac{\pi}{2}\right]_y. \end{aligned}$$

These sequences are written in left-to-right temporal order. Radio-frequency pulses are indicated by  $[angle]_{axis}^{spins}$ , and are applied to the spins in the superscript, along the axis in the subscript, by the angle in brackets. No superscript indicates a pulse applied on all the spins. Evolution for the indicated periods under the system's internal couplings is denoted by  $[\frac{1}{2J_{k\ell}}]$ , where  $J_{k\ell}$  represents the coupling constant between spins  $k$  and  $\ell$ . During these free precession periods, only the specific coupling term in the internal Hamiltonian evolves, while the other terms are refocussed by  $\pi$  pulses [51, 47]. The unsubscripted evolution  $[\frac{1}{2J}]$  denotes a sequence of  $\pi$ -pulses designed to allow the evolutions  $[1/(2J_{12})]$  and  $[1/(2J_{34})]$  to occur while refocussing all other interactions. Because the two swap gates commute, they were performed simultaneously in order to reduce decoherence. The details of translating logic gates to pulse sequences can be found in [85, 86].

The density matrices were reconstructed by state tomography [52]. Since only single quantum coherences can be directly observed, tomography involves repeating the experiment several times followed by a different readout pulse sequence each time. A total of 18 readout sequences:  $[\frac{\pi}{2}]_x^1$ ,  $[\frac{\pi}{2}]_x^3$ ,  $[\frac{\pi}{2}]_x^{2,3}$ ,  $[\frac{\pi}{2}]_x^{1,2,3,4}$ ,  $[\frac{\pi}{2}]_y^{1,2,3,4}$ ,  $[\frac{\pi}{2}]_y^{1,2}$ ,  $[\frac{\pi}{2}]_x^{1,3}$ ,  $[\frac{\pi}{2}]_x^{2,4}$ ,  $[\frac{\pi}{2}]_y^{1,2,3}$ ,  $[\frac{\pi}{2}]_x^{1,2,4}$ ,  $[\frac{\pi}{2}]_y^{1,3,4}$ ,  $[\frac{\pi}{2}]_y^2 - [\frac{\pi}{2}]_{-x}^4$ ,  $[\frac{\pi}{2}]_{-x}^1 - [\frac{\pi}{2}]_y^{2,3}$ ,  $[\frac{\pi}{2}]_y^{1,2} - [\frac{\pi}{2}]_{-x}^3$ ,  $[\frac{\pi}{2}]_x^{1,2} - [\frac{\pi}{2}]_y^4$ ,  $[\frac{\pi}{2}]_x^{1,3} - [\frac{\pi}{2}]_y^4$ ,  $[\frac{\pi}{2}]_y^{1,3} - [\frac{\pi}{2}]_{-x}^4$ ,  $[\frac{\pi}{2}]_x^{2,3} - [\frac{\pi}{2}]_y^4$ , were used to rotate all density matrix elements into single quantum coherences. These sequences were of the order of 500  $\mu s$  and therefore did not introduce significant decoherent errors. To measure the efficacy with which the experiment was carried out, we calculated the attenuated correlation [40], i.e.

$$C = \frac{\text{tr}(\rho_{exp}\rho_{theory}^\dagger)}{\sqrt{\text{tr}(\rho_{input}^2)\text{tr}(\rho_{theory}^2)}}.$$

If  $\rho_{exp}$  and  $\rho_{theory}$  are viewed as vectors, then this metric is the directional cosine between the experimental and theoretical density matrices, reduced by the overall attenuation due to relaxation. Using this metric, the correlations at the different steps were respectively 0.99, 0.92 and 0.65 ( $\pm 0.03$ ) (projection equal to 0.79 for the

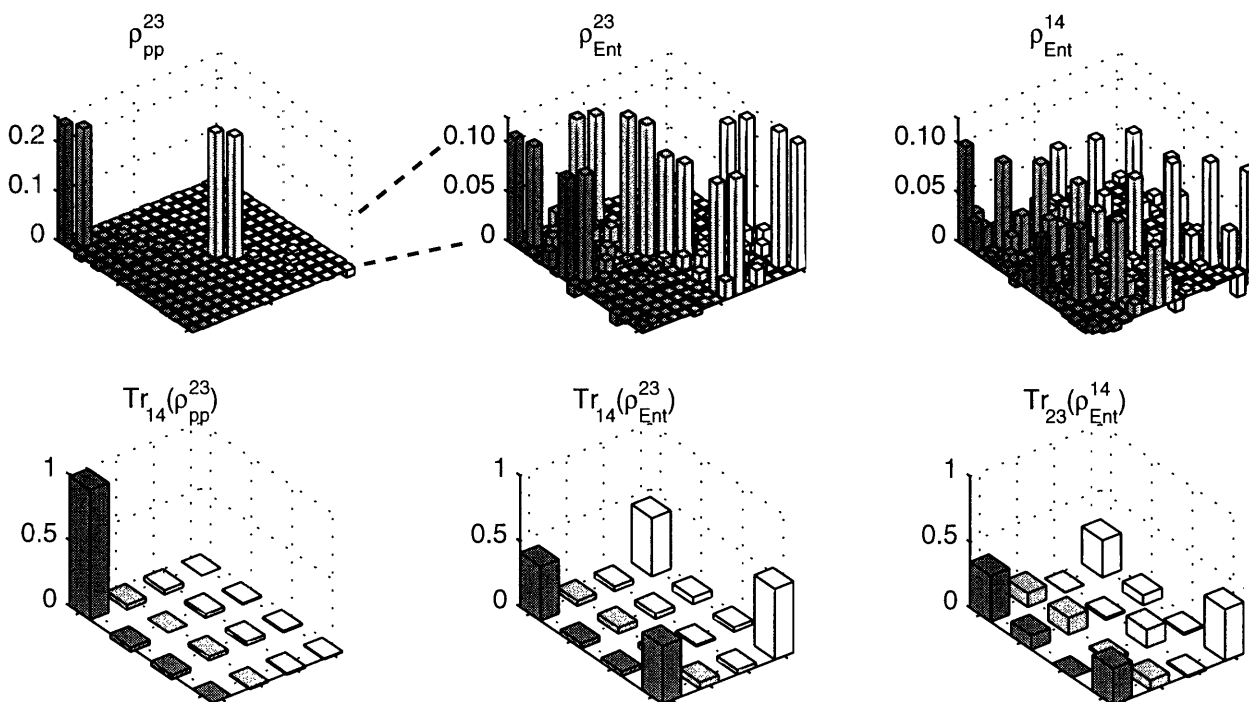


Figure 4-3: **Experimental density matrices.** From left to right are shown the real part of the reconstructed density matrices of the initial pseudo-pure  $\rho_{pp}^{23}$ , spins 2&3 entangled  $\rho_{Ent}^{23}$  and spins 1&4 entangled  $\rho_{Ent}^{14}$  (in normalized units). The bottom row of density matrices is obtained from the top row after having traced over the two ancilla spins. The rows and columns represent the standard computational basis in binary order, with  $|0000\rangle$  starting on the leftmost column and  $|1111\rangle$  being the rightmost column.

last density matrix)<sup>2</sup> while the corresponding reconstructed density matrices are given in Fig. 4-3. This demonstrates a substantial degree of coherent control over a four-qubit homonuclear system. Furthermore, the attenuated correlation of 0.65 at the end of the experiment shows that the deviation part of the density matrix describes, to a significant extent, a pseudo-pure entangled state, demonstrating the dynamics of entanglement transfer. The decrease in the correlations in the course of the experiment can be attributed to imperfect pulses, RF inhomogeneities, and intrinsic decoherence (the total duration of the experiment was 75 ms).

In summary, we have demonstrated entanglement transfer by liquid-state NMR on an homonuclear four-spin system. The density matrices were reconstructed and

<sup>2</sup>The error bar arises from errors in the fits due to non-ideal spectra (imperfect shim), imperfect fitting algorithm and from some unknown coherent and incoherent errors in the readout pulses. It is simply estimated by doing state tomography on the thermal equilibrium state and by calculating the correlation.

the correlations calculated, illustrating the control available in NMR with the use of strongly modulating pulses. It should be noted that the (relatively small)  $J_{14}$  term in the internal spin Hamiltonian was always refocussed, so that no direct interaction between spins 1 and 4 was used for this entanglement transfer [78, 87]. Since the coupling networks available in larger molecules are generally quite sparse, this technique is expected to be useful in future demonstrations of quantum information processing by NMR, as well as in many potential implementations of quantum computers.

## 4.2 Entanglement Swapping Experiment

### 4.2.1 The Experiment

We report in this section the implementation of an entanglement swapping experiment to illustrate the gain in control achieved given the compensations for the errors presented earlier in this thesis (RF inhomogeneity, feedback). In addition, this experiment shows the manipulation of entanglement through measurements. This demonstration was carried out on a liquid-state NMR quantum information processor, using the same sample of crotonic acid as in the previous experiment (see Fig. 4-2) and a Bruker AVANCE 400 MHz spectrometer for the control and acquisition. The experiment consisted of initializing the system to a full 4-spin pseudo-pure state made of two pairs of singlet states and then performing on two of these qubits a Bell measurement, each one belonging to a different pair (an NMR version of [78]) (see Fig. 4-4). The protons were decoupled only during acquisition to avoid Nuclear Overhauser Enhancement [47]. During the gate sequence, the proton-carbon couplings were refocused using  $\pi$  pulses on the carbon channel. Since liquid-state NMR deals with a highly mixed ensemble of spin systems, we stress that the use of pseudo-pure states allows a macroscopic description of the same unitary dynamics to which the microscopic systems are subject [26, 27]. The experiment described here does not depend on the entanglement within the individual molecules. The traceless part of the density matrix was prepared in a state isomorphic to:

$$|\Psi\rangle_{1234} = \frac{1}{2}(|01\rangle_{12} - |10\rangle_{12}) \otimes (|01\rangle_{34} - |10\rangle_{34}).$$

which can be rewritten as

$$|\Psi\rangle_{1234} = \frac{1}{2}(|\Psi^+\rangle_{14}|\Psi^+\rangle_{23} + |\Psi^-\rangle_{14}|\Psi^-\rangle_{23} + |\Phi^+\rangle_{14}|\Phi^+\rangle_{23} + |\Phi^-\rangle_{14}|\Phi^-\rangle_{23}).$$

where  $\Psi^\pm$  and  $\Phi^\pm$  correspond to the four Bell states. Performing a von-Neumann measurement on qubits 2 and 3 in the Bell basis projects qubits 1 and 4 onto one of the four Bell states with probabilities equal to 1/4. The entanglement thereby is transferred between two pairs of spins. This experiment includes the first 4 qubit initialization to a full spatial pseudo-pure state. State tomography was done again at

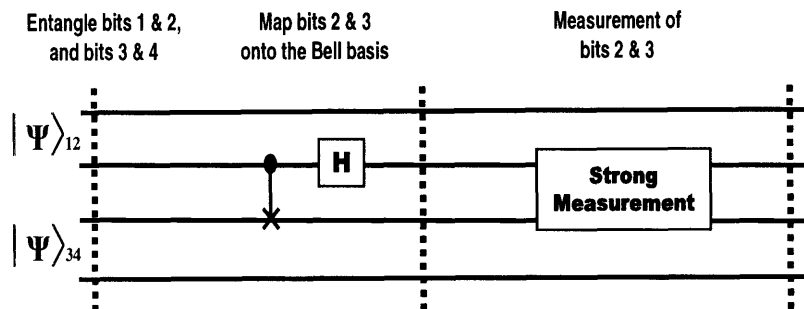


Figure 4-4: **Logical network for the entanglement swapping experiment.** The four qubits are initialized to the full pseudo-pure state  $|\psi\rangle_{12} \otimes |\psi\rangle_{34}$  where  $|\psi\rangle = \frac{1}{\sqrt{2}}(|01\rangle - |10\rangle)$ . The CNOT and Hadamard gates then map the Bell basis to the computational one. That operation followed by a strong measurement in the computational basis mimicks a strong measurement in the Bell basis.

the different key steps using 18 readout pulses in order to identify the different errors and to calculate the correlation. The sequence used to initialize the spin-system to the pseudo-pure state was derived from [40]<sup>3</sup>. We stress that, once the NMR spectrometer had been calibrated and the strongly modulating pulses programmed, no further adjustments of any kind were required (or made) during the course of the measurements that made up this study. The correlation of the initialized density matrix is  $0.929 \pm 0.015$  (the real part of the density matrix is plotted in Fig. 4-5), while the one of the final density matrix, i.e. after the Bell measurement, is  $0.90 \pm 0.015$  (see Fig. 4-6).

The experiment consisted of 65 pulses with a total duration of 121 ms. This may be compared to the previous experiment, which used 44 pulses, lasted 75 ms, and yielded a final correlation of  $0.79 \pm 0.03$  (attenuated correlation =  $0.65 \pm 0.03$ ). This experiment with a correlation of 0.90, confirms the increased level of control. In addition, simulations of the full spin system (including the protons) without decoherent effects using the new design of the pulses yielded a correlation of 0.935 for the initial pseudo-pure state and 0.87 using the previous design, providing further evidence of improved control. The sample has a dephasing time,  $T_2$ , of order 600 ms, and we assume that most of the differences between the measurements and simulation arise from decoherence. Because different elements in the density matrix decay

<sup>3</sup>The sequence is the following (from left to right):  $[acos(1/6)]_y^1 - G - \sqrt{C1NOT}2 - \sqrt{C1NOT}3 - \sqrt{C1NOT}4 - G - [acos(1/3)]_y^3 - \sqrt{C3NOT}2 - \sqrt{C3NOT}4 - G - SWITCH_{2,3}$ . At this point the state is  $E_p \otimes E_p \otimes (\sigma_z^3 + \sigma_z^4 + \frac{2}{3})$  where  $E_p = |0\rangle\langle 0|$ . Qubits 1 and 2 from there can easily be transformed to a singlet state while qubits 3 and 4 are transformed into the same state via:  $[\frac{\pi}{2}]_{-x}^3 - [\frac{\pi}{2}]_y^4 - [\frac{1}{2J_{34}}] - [\frac{\pi}{2}]_y^4 - [\frac{\pi}{2}]_{-x}^3 - [asin(1/\sqrt{(3)})]_{y,y}^{3,4} - [\frac{\pi}{4}]_x^{3,4} - G$ . The last two pulses could have been ideally  $[54.73 \text{ deg}]_{\pi/4}^{3,4}$  (magic angle) but the last sequence behaves the same on this particular input state.

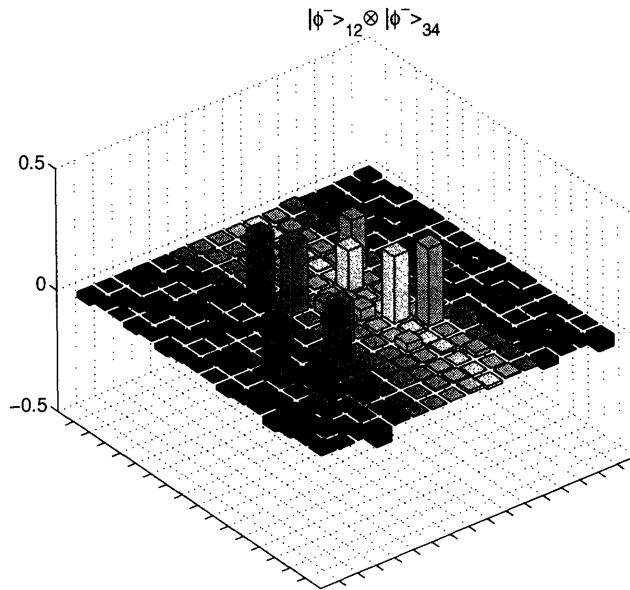


Figure 4-5: **Real part of the initial density matrix (product of singlet states).** The rows and columns represent the standard computational basis in binary order, with  $|0000\rangle$  starting from the leftmost column and  $|1111\rangle$  being the rightmost column.

with different rates, decoherence not only attenuates the magnitude of the density matrix  $\text{trace}(\rho^2)$  but it also rotates it so that the correlation between the two density matrices is reduced.

### 4.2.2 Measurement in the Bell Basis

In this study, measurement in the Bell basis is replaced with dephasing, which is more conveniently carried out in the Zeeman basis (see [88] for a detailed description). The mapping from the Bell to the Zeeman basis can be performed by applying a CNOT gate on qubits 2 and 3 followed by an Hadamard on only qubit 2. After the dephasing in the Zeeman basis, the inverse mapping should be applied to return the system to the original basis. However, in the network shown in Fig. 4-4 this inverse mapping was not included for the sake of clarity, i.e. to exhibit the structure of the 4 Bell states shown in Fig. 4-6. The measurement in the computational basis destroys phase coherences between the two spins of interest. Experimentally this was accomplished using the non-unitary dynamics of magnetic field gradients integrated over the spatially distributed sample [9]. Because a gradient evolution superimposes a linear phase ramp on the chemical shift function of position, the resulting spatial average over the ensemble destroys any phase coherence between the spins. In the simulation to be described, the amount of entanglement transferred to qubits 1 and 4 clearly depends on the selective decoherence of qubits 2 and 3. The input state in this simulation is the measured experimental density matrix  $\rho_{\text{singlet}}$  given in Fig. 4-5, on which the simulated unitary operator  $U_{\text{BellMap}}$  which maps the Bell basis to the Zeeman one is applied. The state then goes through a measurement process,

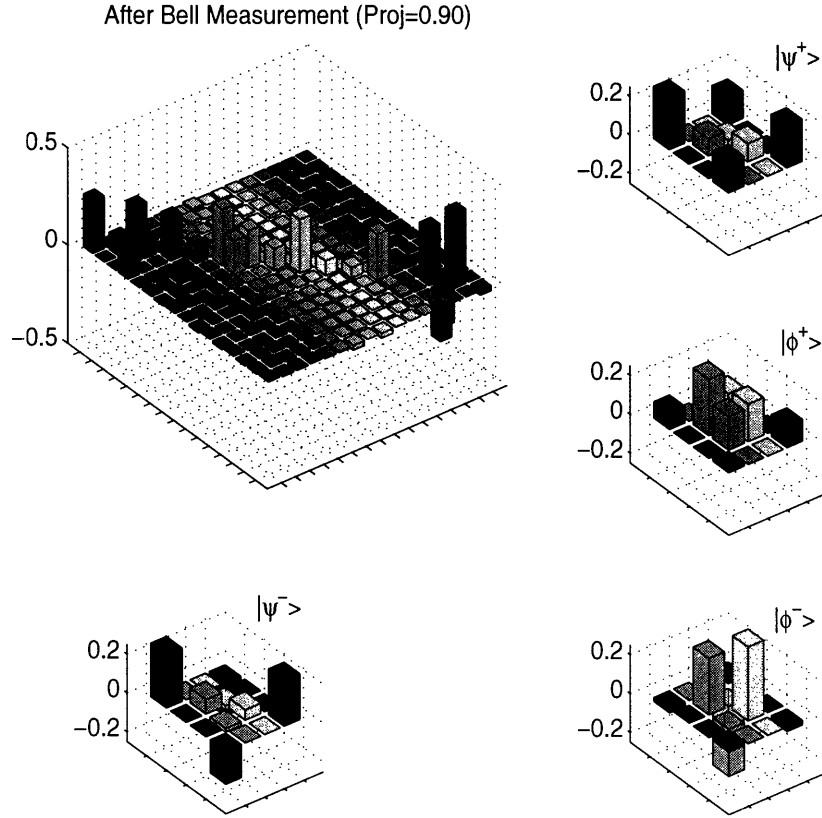


Figure 4-6: **Bell states.** For the sake of convenience, the labels of the spins have been switched so that the pattern characteristic of the Bell states is more clear. Now the ket  $|0000\rangle$  should be interpreted as  $|0\rangle_2 \otimes |0\rangle_3 \otimes |0\rangle_1 \otimes |0\rangle_4$ . One can see that the measurement results in an equal mixture of the four Bell states. For clarity, we zoomed on the sub-matrices along the diagonal to show the Bell states more clearly ( $|\psi^\pm\rangle = \frac{1}{\sqrt{2}}(|00\rangle \pm |11\rangle)$ ,  $|\phi^\pm\rangle = \frac{1}{\sqrt{2}}(|01\rangle \pm |10\rangle)$ ).

represented by the following Kraus operator-sum representation:

$$\rho_{out} = \sum_{k=1}^5 A_k \rho_{in} A_k^\dagger.$$

where  $A_1 = \sqrt{(1 - \alpha^2)}I$ ,  $A_2 = \alpha(|00\rangle\langle 00|)_{23}$ ,  $A_3 = \alpha(|01\rangle\langle 01|)_{23}$ ,  $A_4 = \alpha(|10\rangle\langle 10|)_{23}$  and  $A_5 = \alpha(|11\rangle\langle 11|)_{23}$  and where by  $(|\psi\rangle\langle\psi|)_{23}$  we mean the projectors in the subspace of qubits 2 and 3 (note that the trace-preserving condition is satisfied  $\sum_{k=1}^5 A_k^\dagger A_k = I$ ). The value of  $\alpha$  is then varied to study the entanglement transfer as a function of the strength of the measurement,  $\alpha = 1$  corresponding to a strong measurement and  $\alpha = 0$  to no measurement. In Fig. 4-7, we plot as a function of  $\alpha$  the correlation between  $\rho_{out}$ , obtained by doing the simulation described above, and  $\rho_{th}$  (the maximally entangled theoretical density matrix). This plot shows the amount of entanglement transferred as a function of the strength of the measurement.

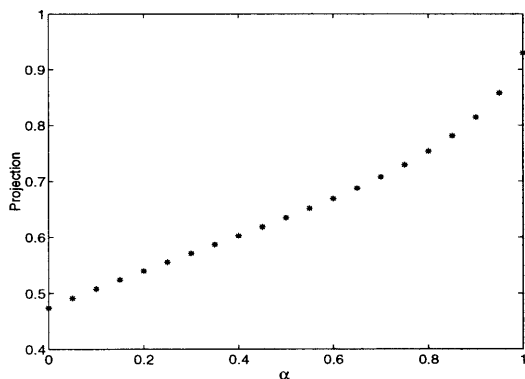


Figure 4-7: **Entanglement transfer efficiency versus the strength of the measurement.** For  $\alpha = 1$  the correlation between the simulated  $\rho_{out}$  and the theoretical density matrix is equal to 0.93. This value being less than 1 is due to the non perfect experimental input state and to the coherent errors contained in  $U_{BellMap}$ .

The correlation between our measured output density matrix and the theoretical one was 0.90. Fig. 4-7 thereby reveals that we reached a precision of better than 5 % ( $\alpha > 0.95$ ) for the implemented selective decoherence.

### 4.3 Conclusion

We reported in this chapter experiments that demonstrate the coherent control achieved by using strongly modulating pulses. When information about the types of time-independent errors is available, we showed how the former method could be extended to counteract them and we provided strong experimental evidence for the improvement made. Incorporating these features in the design of the pulses allowed to obtain an evolution very close to being unitary for single qubit gates. Only the second experiment made use of pulses corrected for systematic variations using the feedback mechanism, and designed to be robust against RF inhomogeneity. We reconstructed the density matrices at the key steps and extracted the correlations in both experiments. The higher correlations reported in the second experiment indicate a net improvement of coherent control, in spite of a higher complexity (65 vs. 44 pulses, and 121 ms vs. 75 ms).



# Chapter 5

## Quantum Process Tomography

Although quite general schemes exist to protect quantum information against decoherence [89, 90, 91], designing the optimal quantum error correction code requires knowledge about the noise generators involved in the non-unitary process. We present in this chapter a robust method for quantum process tomography, which yields a set of Lindblad operators that optimally fit the density operators measured at a sequence of time points. The benefits of this method are illustrated using a set of liquid-state nuclear magnetic resonance measurements on a molecule containing two coupled hydrogen nuclei, which are sufficient to fully determine its relaxation superoperator. It was found that the complete positivity constraint, which is necessary for the existence of the Lindblad operators, was also essential for obtaining a *robust* fit to the measurements.

### 5.1 Introduction

An important task in designing and building devices capable of quantum information processing (QIP) is to determine the superoperators that describe the evolution of their component subsystems from experimental measurements. This task is commonly known in QIP as *Quantum Process Tomography* (QPT) [54]. The superoperators obtained from QPT allow one to identify the dominant sources of decoherence and focus development efforts on eliminating them, while precise knowledge of relevant parameters can be used to design quantum error correcting codes and/or decoherence-free subsystems that circumvent their effects [92, 54]. Methods have previously been described by which the “superpropagator”  $\mathcal{P}$  of a quantum process can be determined [75, 93]. Assuming that the process’ statistics are stationary and Markovian [94, 95], a more complete description may be obtained by determining the corresponding “supergenerator”, that is, a time-independent superoperator  $\mathcal{G}$  from which the superpropagator at any time  $t$  is obtained by solving the differential equation

---

<sup>1</sup>Parts of this chapter were extracted from N. Boulant, T. F. Havel, M. A. Pravia, and D. G. Cory, “Robust method for estimating the Lindblad operators of a dissipative quantum process from measurements of the density operator at multiple points,” *Physical Review A*, 67:042322, 2003.

$\dot{\mathcal{P}}(t) = -\mathcal{G}\mathcal{P}(t)$ . The formal solution to this equation is  $\exp(-\mathcal{G}t)$ , where “exp” is the operator exponential.

The purpose of this chapter is to describe a data fitting procedure by which estimates of a supergenerator can be obtained. This problem is nontrivial because, as in many other data fitting problems, the estimates obtained from straightforward (e.g. least-squares) fits turn out to be very sensitive to small, and even random, errors in the measured data. In some cases, this may result in a supergenerator that is obviously physically impossible; in others, it may simply result in large errors in the generator despite it yielding a reasonably good fit to the data. Parameter estimation problems with this property are commonly known as *ill-conditioned* [96, 97]. The main result is that, although the problem of estimating a supergenerator from measurements of the superpropagators at various times is ill-conditioned, this ill-conditioning can be greatly alleviated by incorporating prior knowledge of the solution into the fitting procedure as a constraint. The prior knowledge that we use here is a very general property of open quantum system dynamics known as *complete positivity*.

Roughly speaking, complete positivity means that if  $\mathcal{P}$  is a superoperator that maps a density operator of a system to another density operator, then any extension of the form  $\mathcal{I} \otimes \mathcal{P}$  also returns a positive operator, where  $\mathcal{I}$  denotes the identity map on an extension of the domain of  $\mathcal{P}$ . The most general form of a completely-positive Markovian master equation for the density operator  $\rho$  of a quantum system is known as the Lindblad equation [94, 95]. This may be written as

$$\dot{\rho}(t) = -i[H, \rho(t)] + \frac{1}{2} \sum_{m=1} ([L_m \rho(t), L_m^\dagger] + [L_m, \rho(t) L_m^\dagger]), \quad (5.1)$$

where  $\hbar = 1$ ,  $t$  is the time,  $H$  is the system’s Hamiltonian, the  $L_m$  are known as Lindblad operators, and the  $L_m^\dagger$  denote their adjoints. It is easily seen that the Lindblad equation necessarily preserves the trace  $\text{tr}(\rho) = 1$  of the density matrix, meaning  $\text{tr}(\dot{\rho}) = 0$ , and a little harder to show that it also preserves the positive-semidefinite character of the density operator. Proofs that it has the yet-stronger property of complete positivity may be found in Refs. [94, 98, 99, 68]. The QPT method we describe here relies upon the Lindblad characterization of complete positivity.

This chapter is organized as follows. In the first part we present a computational procedure which fits a completely positive supergenerator to a sequence of estimates of the superpropagators of a quantum process at multiple time points. This procedure initially extracts an estimate of the decoherent part of the supergenerator, without the Hamiltonian commutation superoperator (which is assumed to be available from independent prior measurements). It then refines this initial estimate via a nonlinear least-squares fit to the superpropagators, in which complete positivity is enforced by adding a suitable penalty function to the sum of squares minimized. Finally, any residual non-completely-positive part of the supergenerator is “filtered” out by a matrix projection technique based on principle component analysis [68, 100].

In the second part of this chapter, the procedure is validated by using it to determine the natural spin-relaxation superoperator of a molecule containing two coupled

spin 1/2 nuclei in the liquid state from a temporal sequence of density operators. These in turn were derived by state tomography, meaning a set of NMR measurements sufficient to determine the density matrix. In the process we confirm the ill-conditioned nature of the problem, and that the complete positivity constraint is needed to obtain a robust estimate of the supergenerator. The final results are used to compute the corresponding Lindblad operators, but these were difficult to interpret. Hence the Hadamard representation of  $T_2$ -relaxation dynamics [101] was used to derive a new set of Lindblad operators which are easier to interpret and explain most of the relaxation dynamics. The information these operators convey agree with theoretical expectations as well as with some additional independent measurements, in support of the accuracy of the results obtained.

## 5.2 Computational Procedure

We are concerned here with an  $N$ -dimensional open quantum system ( $N < \infty$ ), the dynamics of which are described by a Markovian master equation of the form [47, 95, 94]:

$$\frac{d\rho}{dt} = -i[H, \rho] - \mathcal{R}(\rho - \rho_{\text{eq}}) \quad (5.2)$$

$$\Leftrightarrow \frac{d\rho_{\Delta}}{dt} = -i\mathcal{H}\rho_{\Delta} - \mathcal{R}\rho_{\Delta} \quad (5.3)$$

In this equation,  $\hbar \equiv 1$ ,  $\rho = \rho(t)$  is the system's density operator,  $\rho_{\text{eq}}$  this operator at thermal equilibrium,  $\rho_{\Delta} \equiv \rho - \rho_{\text{eq}}$ ,  $H$  is the system's internal Hamiltonian,  $\mathcal{H}$  the corresponding commutation superoperator, and  $\mathcal{R}$  is the so-called *relaxation superoperator*. The equivalence of the first and second lines follows from the fact that  $\rho_{\text{eq}}$  is time-independent and proportional to the Boltzman operator  $\exp(-H/k_{\text{B}}T)$ , so that it commutes with  $H$ .

By choosing a basis for the ‘‘Liouville space’’ of density operators, the equation may be written in matrix form as [47, 102, 68]

$$\frac{d|\underline{\rho}_{\Delta}\rangle}{dt} = -(\underline{i\mathcal{H}} + \underline{\mathcal{R}})|\underline{\rho}_{\Delta}\rangle \equiv -\underline{\mathcal{G}}|\underline{\rho}_{\Delta}\rangle \quad (5.4)$$

where the underlines denote the corresponding matrices and  $|\underline{\rho}\rangle$  is the  $N^2$ -dimensional column vector obtained by stacking the columns of the density matrix  $\underline{\rho}$  on top of each other in left-to-right order [68]. A numerical solution to this equation at any point  $t$  in time may be obtained by applying the propagator  $\underline{\mathcal{P}}(t)$  to the initial condition  $|\underline{\rho}_{\Delta}(0)\rangle$ , where the propagator is obtained by computing the matrix exponential  $\underline{\mathcal{P}}(t) = \underline{\exp}(-\underline{\mathcal{G}}t)$  [102, 103]. Note that  $\underline{\mathcal{H}}$  and  $\underline{\mathcal{R}}$  do not commute in general, and that the sum  $\underline{\mathcal{G}} \equiv \underline{i\mathcal{H}} + \underline{\mathcal{R}}$  will not usually be a normal matrix (one which commutes with its adjoint). This in turn greatly reduces the efficiency and stability with which its matrix exponential can be computed [104] (although this was not an issue in the small problems dealt with here), and we expect it to also significantly complicate the

*inverse problem.*

In this section we describe an algorithm for solving this inverse problem, that is to determine the relaxation superoperator  $\underline{\mathcal{R}}$  from an estimate of the Hamiltonian  $\underline{H}$  together with estimates of the propagator  $\underline{\mathcal{P}}_m = \underline{\mathcal{P}}(t_m)$  at  $M \geq 1$  time points  $0 < t_1 < t_2 < \dots < t_M$ . This problem, like many other inverse problems, turns out to be ill-conditioned, meaning that small experimental errors in the estimates of the  $\underline{H}$  and  $\underline{\mathcal{P}}_m$  may be amplified to surprisingly large, and generally nonphysical, errors in the resulting superoperator  $\underline{\mathcal{R}}$  [96]. For example, if one tries to estimate  $\underline{\mathcal{R}}$  in the obvious way as

$$\underline{\mathcal{R}} \approx \left( -i\underline{\mathcal{H}} - \underline{\log}(\underline{\mathcal{P}}_1) \right) / t_1, \quad (5.5)$$

one will generally obtain nonsense even if  $\underline{H}$  and  $\underline{\mathcal{P}}_1$  are known to machine precision, because of the well-known ambiguity of the matrix logarithm with respect to the addition of independent multiples of  $2i\pi$  onto its eigenvalues. Using the principal branch of the logarithms will only work if  $\mathcal{H}$  is small compared to  $\mathcal{R}$ , and the only reasonably reliable means of resolving the ambiguities is to utilize additional data and/or prior knowledge of the solution. Even then, a combinatorial search for the right multiples of  $2i\pi$  may be infeasibly time-consuming.

An alternative to the logarithm which utilizes data at multiple time points and is capable of resolving the ambiguities even when  $\mathcal{H}$  is much larger than  $\mathcal{R}$  is to estimate the derivative at  $t = 0$  of

$$\underline{e}^{it\underline{\mathcal{H}}/2} \underline{\mathcal{P}}(t) \underline{e}^{it\underline{\mathcal{H}}/2} = \underline{e}^{-t\underline{\mathcal{R}}} + O(t^2). \quad (5.6)$$

This derivative is obtained by Richardson extrapolation using central differencing about  $t = 0$  over a sequence of time points such that  $t_m = 2^{m-1}t_1$  ( $m = 1, \dots, M$ ), according to the well-known procedure [105]:

```

for m from 1 to M do
   $\underline{\mathcal{D}}_{1,1+M-m} := 2^{m-2} (\underline{e}^{it_m\underline{\mathcal{H}}/2} \underline{\mathcal{P}}_m \underline{e}^{it_m\underline{\mathcal{H}}/2} - \underline{e}^{-it_m\underline{\mathcal{H}}/2} \underline{\mathcal{P}}_m^{-1} \underline{e}^{-it_m\underline{\mathcal{H}}/2})$ ;
  for l from 1 to m-1 do
     $\underline{\mathcal{D}}_{1+l,1+M-m} := \underline{\mathcal{D}}_{l,1+M-m} + (\underline{\mathcal{D}}_{l,1+M-m} - \underline{\mathcal{D}}_{l,M-m}) / (4^l - 1)$ ;
  end do
end do

```

The inverse  $\underline{\mathcal{P}}_m^{-1} = \underline{\mathcal{P}}(-t_m)$  is assured of existing unless long times are used or the errors in the data are large. The method produces an estimate of the derivative at  $t = 0$  that is accurate up to  $O(t_1^{2M})$ , and which may be increased by computing the exponential from the highest-order estimate at further interval halvings. The method performs well when the relative errors in the Hamiltonian  $\delta \ll 1/(\Delta\nu t_M)$ , where  $\Delta\nu$  is the range of frequencies present in the Hamiltonian, but it tends to emphasize the errors in  $\underline{\mathcal{P}}_1$  rather than averaging over the errors at all the time points. Hence we do not recommend that it be used alone, but rather as a means of obtaining a good starting point for a nonlinear fit to the data, as will now be described.

This nonlinear fit involves minimization of the sum of squares

$$\chi^2(\underline{\mathcal{R}}; \underline{\mathcal{H}}, \underline{\mathcal{P}}_1, \dots, \underline{\mathcal{P}}_M) \equiv \sum_{m=1}^M \left\| \exp(-(\imath \underline{\mathcal{H}} + \underline{\mathcal{R}}) t_m) - \underline{\mathcal{P}}_m \right\|_{\mathbb{F}}^2 \quad (5.7)$$

with respect to  $\underline{\mathcal{R}}$ , where  $\|\cdot\|_{\mathbb{F}}^2$  denotes the squared Frobenius norm (sum of squares of the entries of its matrix argument). Previous results with similar minimization problems indicate that  $\chi^2$  will have many local minima [106], making a good starting point that takes the  $2\imath\pi$  ambiguities into account absolutely necessary. The derivatives of this function may be obtained via the techniques described in Ref. [103], but the improvements in efficiency to be obtained by their use are likely to be of limited value in practice given that all the resources needed, both experimental and computational, grow rapidly with  $N$  (which itself grows exponentially with the number of qubits used in quantum information processing problems). In addition, the quality of the results matters a great deal more than the speed with which they are obtained, and the quality will not generally depend greatly on the accuracy with which the minimum is located.

For these reasons, we have used the Nelder-Mead simplex algorithm [46], as implemented in the MATLAB<sup>TM</sup> program, for the small (two qubit) experimental test problem described in the following section. This has the further advantage of being able to avoid local minima better than most gradient-based optimization algorithms. Preliminary numerical studies, however, exhibited the anticipated ill-conditioning with respect to small perturbations in the data, even when  $\underline{\mathcal{R}}$  was constrained to be symmetric (implying a unital system which satisfies detailed balance) and positive semidefinite (as required for the existence of a finite fixed point). Therefore it is necessary to incorporate additional prior information regarding  $\underline{\mathcal{R}}$  into the minimization. The information that we have found to be effective is a property of  $\underline{\mathcal{R}}$  known as *complete positivity* [95, 94, 68].

An *intrinsic* definition which does not involve an environment was first given by Kraus [53], and states that a superpropagator  $\mathcal{P}$  is completely positive if and only if it can be written as a “Kraus operator sum”, namely

$$\mathcal{P}(\rho) = \sum_{\ell=1}^{N^2} K_{\ell} \rho K_{\ell}^{\dagger}, \quad (5.8)$$

where  $\rho = \rho^{\dagger}$  and  $K_1, \dots, K_{N^2}$  all act on the system alone. Another intrinsic definition subsequently given by Choi [107] states that a superpropagator is completely positive if and only if, relative to any basis of the system’s Hilbert space, the so-called *Choi matrix* is positive semidefinite [68], namely

$$\underline{0} \preceq \underline{\mathcal{C}} \equiv \sum_{i,j=0}^{N-1} \underline{\mathcal{P}}(|i\rangle\langle j|) \otimes (|i\rangle\langle j|) = \sum_{i,j=0}^{N-1} \underline{\mathcal{P}}(|i\rangle\langle j|) \langle\langle i|j| \rangle\rangle. \quad (5.9)$$

This equation uses the notation of quantum information processing, in which the  $i$ -th

elementary unit vector is denoted by  $|i\rangle$  ( $0 \leq i < N$ ),  $\underline{\mathcal{P}}(|i\rangle\langle j|)$  is the  $N \times N$  matrix of the operator obtained by applying the superpropagator  $\mathcal{P}$  to the projection operator given by  $|i\rangle\langle j|$  versus our choice of basis, and  $\underline{\mathcal{P}}$  is the  $N^2 \times N^2$  matrix for  $\mathcal{P}$  versus the Liouville space basis  $|i\rangle|j\rangle$  (as for  $\underline{\mathcal{H}}$  etc. above). It can further be shown that the eigenvectors  $\underline{k}_\ell$  of the Choi matrix are related to the (matrices of an equivalent set of) Kraus operators by  $|\underline{K}_\ell\rangle = \sqrt{\kappa_\ell} \underline{k}_\ell$ , where  $\kappa_\ell \geq 0$  are the corresponding eigenvalues and the “ket”  $|\underline{K}_\ell\rangle$  again indicates the column vector obtained by stacking the columns of  $\underline{K}_\ell$  on top of one another [68].

These results can be used not only to compute a Kraus operator sum from any completely positive superpropagator given as a “supermatrix” acting on the  $N^2$ -dimensional Liouville space, but also to “filter” such a supermatrix so as to obtain the supermatrix of the completely positive superpropagator nearest to it, in the sense of minimizing the Frobenius norm of their difference [68]. This is done simply by setting any negative eigenvalues of the Choi matrix to zero, rebuilding it from the remaining eigenvalues and vectors, and converting this reconstructed Choi matrix back to the corresponding supermatrix. Although this generally has a beneficial effect upon the least-squares fits versus  $\chi^2$  (as defined above), it is still entirely possible that the sequence of filtered propagators  $\mathcal{P}'_m$  will not correspond to a completely positive *Markovian* process, so that no time-independent relaxation superoperator  $\mathcal{R}$  can fit it precisely. This, together with the ill-conditioned nature of the problem, implies one will still not usually obtain satisfactory results even after filtering. For this reason we shall now describe how the above characterizations of completely positive superpropagators can be extended to supergenerators.

As indicated in the introduction, completely positive Markovian processes, or *quantum dynamical semigroups* as they are also known, may be characterized as those with a generator  $\mathcal{G}$  that can be written in Lindblad form [99, 98, 95, 94, 68]. On expanding the commutators in Eqn (5.1), this becomes

$$-\mathcal{G}(\rho) \equiv -i[H, \rho] + \frac{1}{2} \sum_{m=1}^{N^2} \left( 2 L_m \rho L_m^\dagger - L_m^\dagger L_m \rho - \rho L_m^\dagger L_m \right). \quad (5.10)$$

The operators  $L_m$  are usually called *Lindblads*. It may be seen that the Choi matrix  $\underline{\mathcal{C}}$  associated with  $-\underline{\mathcal{R}}$  is *never* positive semidefinite, because  $\langle \underline{I} | \underline{\mathcal{C}} | \underline{I} \rangle = \text{tr}(-\underline{\mathcal{R}}) < 0$ . Nevertheless, it can be shown that the superpropagator obtained by taking the exponential of any trace-preserving supergenerator  $\underline{\mathcal{R}}$  (meaning  $\text{tr}(\mathcal{R}(\rho)) = \langle \underline{I} | \underline{\mathcal{R}} | \underline{\rho} \rangle = 0$ ) is completely positive if and only if a certain projection of  $\underline{\mathcal{C}}$  is positive semidefinite, namely  $\underline{\mathcal{E}} \underline{\mathcal{C}} \underline{\mathcal{E}}$  where  $\underline{\mathcal{E}} = \underline{I} \otimes \underline{I} - |\underline{I}\rangle \langle \underline{I}|$  [68]. In this case an equivalent system of orthogonal Lindblads is determined by  $|\underline{L}_m\rangle = \sqrt{\lambda_m} \underline{\ell}_m$ , where  $\lambda_m \geq 0$  are the eigenvalues and  $\underline{\ell}_m$  the eigenvectors of  $\underline{\mathcal{E}} \underline{\mathcal{C}} \underline{\mathcal{E}}$ . In the event that  $\underline{\mathcal{E}} \underline{\mathcal{C}} \underline{\mathcal{E}}$  has negative eigenvalues we can simply set them to zero to obtain a similar but completely positive supergenerator, much as we did with the Kraus operators. Most importantly, however, this characterization of completely positive supergenerators gives us a means of enforcing complete positivity during nonlinear fits to a sequence of propagators at multiple time points.

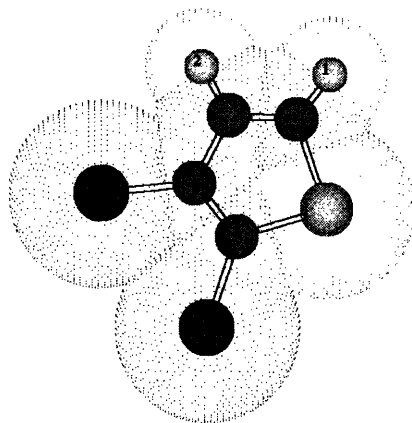


Figure 5-1: Molecule of 2,3 dibromothiophene with the two protons labeled 1 and 2. The chemical bonds among the atoms are indicated by double parallel lines, and a transparent “dot-surface” used to indicate their van der Waals radii.

The following section describes our experience with applying this approach to a sequence of superpropagators obtained from liquid-state NMR data. The complete positivity of the relaxation superoperator was maintained by adding a simple penalty function onto the sum of squares that was minimized by the simplex algorithm, as described above. This penalty function consisted of the sum of the squares of the negative eigenvalues of the corresponding projected Choi matrix. While more rigorous and efficient methods of forcing the projected Choi matrix to be positive semidefinite are certainly possible, this strategy was sufficient to demonstrate that *the complete positivity constraint greatly alleviates the ill-conditioned nature of such fits.*

### 5.3 Experimental Validation

The experiments were carried out on a two-spin  $\frac{1}{2}$  system consisting of the hydrogen atoms in 2,3-dibromothiophene (see Fig. 5.3) at 300K dissolved in deuterated acetone, using a Bruker AVANCE 300 MHz spectrometer.

The internal Hamiltonian of this system in a frame rotating at the frequency of the second spin is

$$H \equiv H_{int} = \pi (\nu_1 \sigma_z^1 + \frac{J}{2} \sigma^1 \cdot \sigma^2) \quad (5.11)$$

where  $\nu_1 = 161.63$  Hz is the chemical shift of the first spin,  $J = 5.77$  Hz is the coupling between the spins, and  $\sigma = [\sigma_x, \sigma_y, \sigma_z]$  are Pauli spin operators.

The “quantum operation” we characterized was just free-evolution of the system under its internal Hamiltonian, together with decoherence and relaxation back towards the equilibrium state  $\rho_{eq} \sim \sigma_z^1 + \sigma_z^2$ . In liquid-state NMR on small organic molecules like dibromothiophene, this process is mediated primarily by fluctu-

ating dipolar interactions between the two protons as well as with spins neighboring molecules, and since the correlation time for small molecules at room temperature liquids is on the order of picoseconds, the Markovian approximation is certainly valid [47, 108]. We add that our sample was not degassed so that the presence of dissolved paramagnetic  $O_2$  shortened the  $T_1$  and  $T_2$  relaxation times.

The experiment consisted of preparing a complete set of orthogonal input states (that is, density matrices), letting each evolve freely for a given time  $T$ , and then determining the full output states via quantum state tomography [52, 67]. Since only “single quantum” coherences can be directly observed in NMR [47, 108], this involves repeating the experiment several times followed by a different readout pulse sequence each time, until all the entries of the density matrix have been mapped into observable ones. The experiments were carried out at four exponentially-spaced times  $T$ , as required by the Richardson extrapolation procedure described above, specifically  $T = 0.4, 0.8, 1.6$  and  $3.2$  s.

| index | operator  | order | index | operator  | order |
|-------|---|-------|-------|---|-------|
| 1     | $4 \times 4$ identity                           | 0     | 9     | $\sigma_x^2$                                    | 1     |
| 2     | $\sigma_z^1$                                    | 0     | 10    | $\sigma_y^2$                                    | 1     |
| 3     | $\sigma_z^2$                                    | 0     | 11    | $\sigma_x^1 \sigma_z^2$                         | 1     |
| 4     | $\sigma_z^1 \sigma_z^2$                         | 0     | 12    | $\sigma_y^1 \sigma_z^2$                         | 1     |
| 5     | $\sigma_x^1 \sigma_x^2 + \sigma_y^1 \sigma_y^2$ | 0     | 13    | $\sigma_z^1 \sigma_x^2$                         | 1     |
| 6     | $\sigma_x^1 \sigma_y^2 - \sigma_y^1 \sigma_x^2$ | 0     | 14    | $\sigma_z^1 \sigma_y^2$                         | 1     |
| 7     | $\sigma_x^1$                                    | 1     | 15    | $\sigma_x^1 \sigma_x^2 - \sigma_y^1 \sigma_y^2$ | 2     |
| 8     | $\sigma_y^1$                                    | 1     | 16    | $\sigma_x^1 \sigma_y^2 + \sigma_y^1 \sigma_x^2$ | 2     |

Table 5.1: **Table of operators (versus Cartesian basis) of the transition basis used for the density and superoperator matrices, the corresponding matrix indices and their coherence orders (see text).**

To describe the density and superoperator matrices, the so-called “transition basis” was used [47]. This Liouville space basis is intermediate between the Cartesian basis and the Zeeman (or polarization and shift operator [47]) basis, in that the basis elements are all Hermitian like those of the Cartesian basis, but like the Zeeman basis they have a well-defined *coherence order*, or difference in total angular momentum along the applied magnetic field  $B_0$  between the two Zeeman states connected by the transition. These basis states are listed in TABLE I versus the Cartesian basis.

This basis was chosen because the relaxation superoperator  $\mathcal{R}$  is expected to have the “Redfield kite” structure in this basis [47]. This block diagonal structure arises because the difference in frequency between transitions of different coherence orders, given that the Zeeman interaction dominates all others, is large enough to average out these other interactions including those responsible for decoherence and relaxation, in effect decoupling the blocks from one another so that no *cross-relaxation* occurs between them <sup>2</sup> (see Fig. 5-2). This so-called “secular approximation” considerably

<sup>2</sup>In general, there is even no cross-relaxation between transverse elements of the density matrix



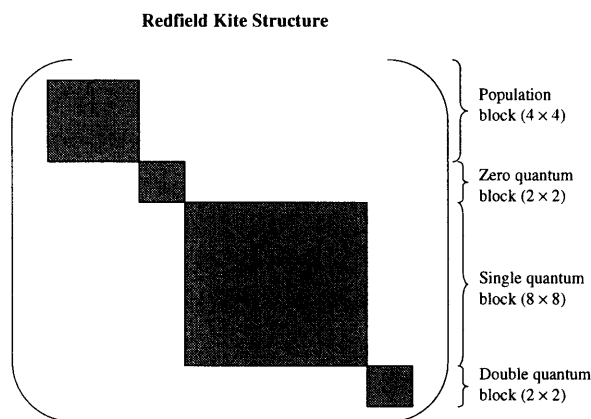


Figure 5-2: **Redfield kite structure of the relaxation superoperator expressed in the transition basis (TABLE I).** The shaded area corresponds to blocks of different coherence order which are effectively decoupled from each other.

reduces the number of parameters in the superoperator from  $256 = ((2^2)^2)^2$  to  $81 = 3^2 + 2^2 + 8^2 + 2^2$  (since neither the identity nor the other diagonal ( $\sigma_z$ ) basis elements are expected to cross relax with any non diagonal elements).

An additional reduction may be obtained by assuming detailed balance: the microscopic reversibility of all cross-relaxation processes. The relaxation superoperator reconstructed from the experimental data was bordered with an initial row and column of zeros to force  $\mathcal{R}(I) = 0$ , because the totally random density matrix  $I/4$  neither varies nor contributes to the variations in any of the other transition operators. This may be done providing  $\mathcal{R}$  operates on  $\rho_\Delta = \rho - \rho_{\text{eq}}$ , and together with detailed balance it implies that the supermatrix  $\underline{\mathcal{R}}$  will be symmetric, reducing the number of parameters to be estimated to only  $48 = 6 + 3 + 36 + 3$ .

The result of applying the fitting procedure without the complete positivity constraint to the initial estimate obtained by Richardson extrapolation is shown in Fig. 5-3(a). It may be seen that the self-relaxation rates did not vary in a systematic fashion with the coherence order and that large cross-relaxation rates were found, neither of which is consistent with the physics of spin relaxation in liquid-state NMR spectroscopy. In addition, this relaxation superoperator implies that spin 1 has a  $T_2 \approx 2.3$  s while spin 2 has a  $T_2 \approx 4.6$  s, in disagreement with the independent measurements of  $T_2$  given below.

The fit after adding the complete positivity constraint is shown in Fig. 5-3(b), again starting from the results of Richardson extrapolation. It may now be seen that the results do vary systematically with coherence number, and that the resulting relaxation superoperator is very nearly diagonal. To obtain further evidence for the

---

in the absence of strong spin-locking fields, so that the relaxation superoperator is in most cases diagonal except for the population part. We still however considered here the possibility of having cross-relaxation between off-diagonal elements of the density matrix.

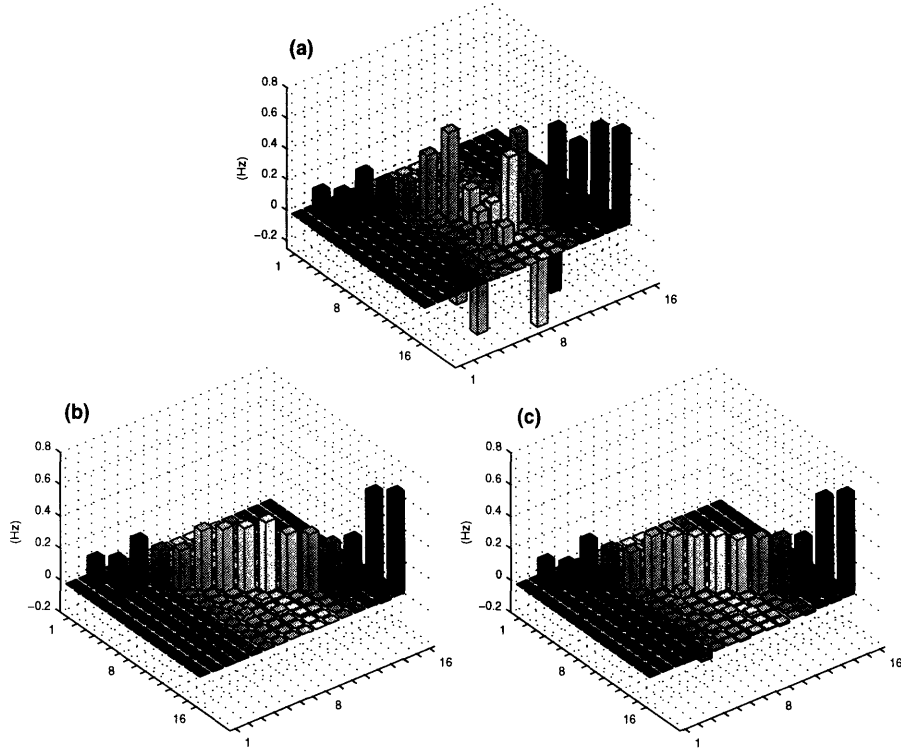


Figure 5-3: **Three different estimates of the relaxation superoperator of 2,3 dibromothiophene in the transition basis, indexed as indicated in Table I.** (a) Relaxation superoperator obtained from a least-squares fit, without the complete positivity constraint, of the exponential  $\exp(-i(\mathcal{H} + \mathcal{R}) t_m)$  to the propagators  $\underline{\mathcal{P}}_m$  at the corresponding times ( $t_1 = 0.4, t_2 = 0.8, t_3 = 1.6, t_4 = 3.2$  s) with respect to the symmetric Redfield kite relaxation superoperator matrix  $\underline{\mathcal{R}}$ , starting from the results of Richardson extrapolation (see text). (b) The relaxation superoperator obtained from a fit to the same data and with the same starting value of  $\underline{\mathcal{R}}$ , but with the complete positivity constraint included in the fit. (c) The relaxation superoperator obtained by assuming that  $\mathcal{H}$  and  $\mathcal{R}$  commute, and using the average of the estimates obtained by taking the logarithms of the absolute values of the eigenvalues of the propagators over all four time points as the final estimate (see text).

validity of this superoperator, we measured the single spin  $T_1$  (longitudinal, or  $\sigma_z$ ) and  $T_2$  (transverse, or  $\sigma_x = \sigma_y$ ) relaxation rates, using the well-established inversion-recovery and CPMG experiments [108]. The results for both spins were  $T_1 = 5.6$  s and  $T_2 = 2.7$  s, which agree quite well with the values of 5.6 s and 2.6 s obtained from this relaxation superoperator. Although this is obviously a relatively simple relaxation superoperator, it is reasonable to expect that a complete positivity constraint will substantially improve the estimates of more complicated superoperators containing nonzero cross-relaxation rates that cannot be obtained from standard experiments.

Finally, the cross-relaxation rate between the population terms  $\sigma_z^1$  and  $\sigma_z^2$ , which is due to the well-known nuclear Overhauser effect [47], is essentially zero in Fig. 3(b). This can occur when the overall rotational correlation time of the molecule plus its “solvent-cage” is on the order of 1 ns, but was somewhat unexpected given the small size of 2,3-dibromothiophene. As a result, we carried out the selective inversion recovery experiment that consists of inverting selectively the longitudinal magnetization of one of the two protons and looking at the evolution of the magnetization of the other one while the first relaxes towards thermal equilibrium. The change in longitudinal magnetization of the second proton was measured to be less than 1% of the unperturbed magnetization revealing essentially no NOE effect and providing yet further evidence for the validity of this superoperator. The discrepancy between this result and that given in Ref. [108] may be explained by the presence of dissolved paramagnetic  $O_2$  in our sample, which shortened the  $T_1$  relaxation time so that the NOE effect became almost unobservable (our  $T_1$  was 5.6 s while the  $T_1$  in Ref. [108] was 47.5 s).

Because of the substantial degeneracy of the diagonal elements with the same coherence order, the superoperator in Fig. 3(b) was also very nearly diagonal in the eigenbasis of the Hamiltonian commutation superoperator  $\mathcal{H}$ , so that  $\mathcal{H}$  and  $\mathcal{R}$  very nearly commute. This allowed further estimates to be obtained directly from the superpropagators  $\mathcal{P}_m \approx \exp(-i\mathcal{H}t_m)\exp(-\mathcal{R}t_m)$ , simply by taking the (real) logarithms of the absolute values of their eigenvalues and thereby canceling the phase factors from the Hamiltonian’s exponential. From Fig. 5-3(c) we see that the result of averaging these estimates over all four evolution times is very similar to the completely positive estimate in Fig. 5-3(b) (correlation coefficient 0.80; ratio of squared norm of the difference to that of the average 0.90). We note that the estimate in Fig. 5-3(c) did not explicitly assume the Redfield kite structure, thereby providing a further consistency check on our results.

## 5.4 Interpretation via Lindblad and Hadamard Operators

In this section we present a system of Lindblad operators which act on the density operator to give essentially the same derivative as the relaxation superoperator described above (see Fig. 5-3). As described in the foregoing “Computational Procedure” section, such a system of Lindblad operators may be obtained by diagonalizing

the corresponding projected Choi matrix, although it will be seen that a more easily interpreted system was obtained by considering the parts of  $\mathcal{R}$  responsible for  $T_1$  and  $T_2$  relaxation separately using the ‘‘Hadamard relaxation matrix’’ formalism [101]. From here on, the relaxation superoperator  $\mathcal{R}$  will correspond to the matrix shown in Fig. 5-3(b).

These representations of relaxation processes are normally applied to the density matrix in the Zeeman basis  $\rho_{\Delta}^{\text{zee}}$  (regarded as the computational basis in QIP), which requires converting the supergenerator  $\mathcal{R}$  from the transition to the Zeeman basis. This is easily done via a unitary transformation,  $\underline{\mathcal{R}}^{\text{zee}} \equiv 2 \underline{U} \underline{\mathcal{R}}^{\text{tra}} \underline{U}^{\dagger}$ , where  $\underline{U} |\rho^{\text{tra}}\rangle = |\rho^{\text{zee}}\rangle$  (the matrix  $\underline{U}$  may be derived from TABLE I; the factor of 2 corrects for a change in norm due to the fact that the transition basis is Hermitian). Although any relaxation superoperator can be modified to act directly on the density operator  $\rho$  rather than its difference with the equilibrium density operator  $\rho_{\Delta} = \rho - \rho_{\text{eq}}$  (*vide supra*) by taking the right-projection  $\underline{\mathcal{R}} (\underline{I} - |\rho_{\text{eq}}\rangle\langle\underline{I}|)$  [109, 110], this makes only a negligible change to  $\mathcal{R}$  since in liquid-state NMR  $\rho_{\text{eq}}$  differs from the identity  $I$  by  $\|\rho_{\text{eq}} - I\|_{\text{F}}/\|I\|_{\text{F}} \leq 10^{-5}$  at room temperature. In any case, the treatment of  $T_1$  relaxation given below was considerably simplified by treating it as a unital (identity preserving) process acting on  $\rho_{\Delta}$ .

As described following Eqn. (5.10), a complete system of Lindblad operators may be obtained by diagonalizing the projected Choi matrix

$$\underline{\mathcal{E}} \underline{\mathcal{C}} \underline{\mathcal{E}} = \underline{V} \underline{\Lambda} \underline{V}^{\dagger}, \quad (5.12)$$

where it is assumed the eigenvalues have been ordered such that  $\lambda_m \geq \lambda_{m+1}$  for  $m = 1, \dots, N^2 - 1$ , and defining the Lindblad matrices such that for all  $\lambda_m > 0$ :

$$|\underline{L}_m\rangle = \sqrt{\lambda_m} \underline{V} |m\rangle. \quad (5.13)$$

This gave rise to a total of 11 Lindblads, the phases of which were chosen so as to make them as nearly Hermitian as possible. Once this was done, all 11 were within 2% of being Hermitian.

The relative contributions of these Lindblads to the overall relaxation of the spins can be quantified by the squared Frobenius norms  $\|\underline{L}_m\|_{\text{F}}^2 = \lambda_m$ . This calculation shows that about 35% of the mean-square noise resided in the first Lindblad, namely

$$\underline{L}_1 \approx 0.346 (\underline{\sigma}_x^1 + \underline{\sigma}_z^2) + 0.025 \underline{\sigma}_z^1 \underline{\sigma}_z^2, \quad (5.14)$$

which represents strongly correlated dephasing with a  $T_2$  for both spins of  $\sim 4.2$  s [101], much as expected. The next four largest Lindblads together contributed, roughly equally, another 43% to the total mean square noise, but were considerably more difficult to interpret:

$$\begin{aligned} \underline{L}_2 \approx & -0.013 \underline{\sigma}_x^1 - 0.045 \underline{\sigma}_y^1 - 0.153 \underline{\sigma}_x^2 - 0.061 \underline{\sigma}_y^2 \\ & + 0.150 \underline{\sigma}_x^1 \underline{\sigma}_z^2 - 0.039 \underline{\sigma}_y^1 \underline{\sigma}_z^2 + 0.111 \underline{\sigma}_z^1 \underline{\sigma}_x^2 + 0.106 \underline{\sigma}_z^1 \underline{\sigma}_y^2 \\ \underline{L}_3 \approx & +0.046 \underline{\sigma}_z^1 - 0.026 \underline{\sigma}_z^2 - 0.057 \underline{\sigma}_x^1 \underline{\sigma}_y^2 - 0.266 \underline{\sigma}_z^1 \underline{\sigma}_z^2 \end{aligned}$$

$$\begin{aligned}
\underline{L}_4 &\approx -0.024 \underline{\sigma}_x^1 - 0.006 \underline{\sigma}_y^1 - 0.081 \underline{\sigma}_x^2 - 0.077 \underline{\sigma}_y^2 \\
&\quad -0.155 \underline{\sigma}_x^1 \underline{\sigma}_z^2 - 0.193 \underline{\sigma}_y^1 \underline{\sigma}_z^2 + 0.002 \underline{\sigma}_z^1 \underline{\sigma}_x^2 - 0.012 \underline{\sigma}_z^1 \underline{\sigma}_y^2 \\
\underline{L}_5 &\approx -0.017 \underline{\sigma}_x^1 - 0.060 \underline{\sigma}_y^1 - 0.071 \underline{\sigma}_x^2 - 0.090 \underline{\sigma}_y^2 \\
&\quad +0.090 \underline{\sigma}_x^1 \underline{\sigma}_z^2 - 0.001 \underline{\sigma}_y^1 \underline{\sigma}_z^2 - 0.183 \underline{\sigma}_z^1 \underline{\sigma}_x^2 - 0.118 \underline{\sigma}_z^1 \underline{\sigma}_y^2
\end{aligned}$$

It can be shown that  $L_3$  contributes about  $0.15\text{s}^{-1}$  to the decay rates of the single-quantum coherences (single-spin flips), bringing down the decay time  $T_2 \approx 2.6$  s and, save for some small cross terms in the single quantum block, rather little else.

The superoperators corresponding to each of the remaining 9 Lindblads separately all contained significant cross terms between the populations and the zero or double quantum coherences, in violation of the secular approximation [47]. Only on summing over all of them do these nonphysical cross-terms cancel out, leaving a largely diagonal relaxation superoperator behind: the ratio of the mean-square value of the off-diagonal entries of  $\mathcal{R}$  to that of the diagonal entries was 1.3% in the transition basis and 3.8% in the Zeeman; the latter dropped to 1.8% on excluding the block corresponding to  $T_1$  relaxation of the populations (*vide infra*). The nonphysical nature of most of the Lindblads is clearly an artifact of the way that our procedure for calculating them forces them to be orthogonal and minimal in number. In order to physically interpret the dominant relaxation processes, we therefore focus our attention first on  $T_1$  relaxation among the populations (diagonal entries of the density matrix in the Zeeman basis), along with the associated nonadiabatic  $T_2$  relaxation, and then try to account for the remaining  $T_2$  relaxation via simple adiabatic, albeit correlated, processes.

The calculations gave four Hermitian Lindblad operators which describe the  $T_1$  relaxation of the first spin,

$$\begin{aligned}
L_{T_1}^{x1} &= \sqrt{0.1532} \frac{1}{2} \sigma_x^1, & L_{T_1}^{y1} &= \sqrt{0.1532} \frac{1}{2} \sigma_y^1, \\
L_{T_1}^{xz} &= \sqrt{0.1532} \frac{1}{2} \sigma_x^1 \sigma_z^2, & L_{T_1}^{yz} &= \sqrt{0.1532} \frac{1}{2} \sigma_y^1 \sigma_z^2,
\end{aligned} \tag{5.15}$$

and similarly for the second spin,

$$\begin{aligned}
L_{T_1}^{x2} &= \sqrt{0.1528} \frac{1}{2} \sigma_x^2, & L_{T_1}^{y2} &= \sqrt{0.1528} \frac{1}{2} \sigma_y^2, \\
L_{T_1}^{zx} &= \sqrt{0.1528} \frac{1}{2} \sigma_z^1 \sigma_x^2, & L_{T_1}^{zy} &= \sqrt{0.1528} \frac{1}{2} \sigma_z^1 \sigma_y^2.
\end{aligned} \tag{5.16}$$

In addition, the near-degeneracy of the (1, 4) and (2, 3) rates in the relaxation superoperator in the Zeeman basis can be used to combine the associated Lindblad operators into four multiple-quantum  $T_1$  Lindblad operators based on the average rate:

$$\begin{aligned}
L_{T_1}^{xx} &= \sqrt{0.0252} \frac{1}{2} \sigma_x^1 \sigma_x^2, & L_{T_1}^{xy} &= \sqrt{0.0252} \frac{1}{2} \sigma_x^1 \sigma_y^2, \\
L_{T_1}^{yx} &= \sqrt{0.0252} \frac{1}{2} \sigma_y^1 \sigma_x^2, & L_{T_1}^{yy} &= \sqrt{0.0252} \frac{1}{2} \sigma_y^1 \sigma_y^2.
\end{aligned} \tag{5.17}$$

By working through some examples, it may be seen that the sum of the Lindbladian superoperators for each of the three sets of four Lindblad operators above also causes all the *off*-diagonal entries of  $\rho_{\Delta}^{\text{zee}}$  to decay with the same rate constant

$1/(2T_1)$ . This corresponds to *nonadiabatic*  $T_2$  relaxation. Therefore we subtracted the nonadiabatic  $T_2$  contribution to get the adiabatic  $T_2$  contribution to  $\mathcal{R}$  and derived the following three Lindblad operators from it using the Hadamard operator formalism:

$$\begin{aligned} L_{T_2}^{\text{ad1}} &= \sqrt{0.9560} \frac{1}{\sqrt{8}} (\sigma_z^1 + \sigma_z^2), & L_{T_2}^{\text{ad2}} &= \sqrt{0.1721} \frac{1}{\sqrt{8}} (\sigma_z^1 - \sigma_z^2), \\ L_{T_2}^{\text{ad3}} &= \sqrt{0.2931} \frac{1}{2} \sigma_z^1 \sigma_z^2. \end{aligned} \quad (5.18)$$

These correspond to totally correlated, totally anticorrelated, and pure single-quantum  $T_2$  relaxation, respectively [101]. Although the Hadamard product formalism gave a simpler description with a clearer physical interpretation, it left a small discrepancy between the complete relaxation superoperator reconstructed from the new Lindblads above and the completely positive relaxation superoperator  $\mathcal{R}^{\text{zee}}$  obtained by fitting to the experimental superpropagators (Fig. 5-3(b)). The matrix of the relaxation superoperator reconstructed from the new Lindblads above,  $\underline{\mathcal{R}}_{\text{new}}^{\text{zee}}$ , was obtained by taking the  $4 \times 4$  matrices for the  $T_1$  and adiabatic  $T_2$  relaxation, i.e.  $\underline{R}_{T_1}^{\text{zee}}$  and  $\underline{R}_{T_2}^{\text{zee}}$ , and distributing their entries at the corresponding locations of the  $16 \times 16$  matrix  $\underline{\mathcal{R}}_{\text{new}}^{\text{zee}}$  while setting all its other entries to zero. The discrepancy was then quantified by computing the relative difference between the superoperators, namely

$$\frac{\|\underline{\mathcal{R}}^{\text{zee}} - \underline{\mathcal{R}}_{\text{new}}^{\text{zee}}\|_{\text{F}}}{\|\underline{\mathcal{R}}^{\text{zee}}\|_{\text{F}}}. \quad (5.19)$$

This gave a value of 6.3%, which is roughly comparable to the errors in the measurements of the density operators ( $\sim 5\%$ ), indicating that the simplifying assumptions made in deriving the new Lindblads are able to account for the experiments to within the measurement errors. These assumptions included a lack of any correlations in the underlying  $T_1$  processes as well as the absence of cross-relaxation in the adiabatic  $T_2$  processes, and are in accord with what is expected in NMR experiments on small molecules in the liquid-state [47].

## 5.5 Conclusion

In this chapter, we have demonstrated a robust procedure by which one can derive a set of Lindblad operators which collectively account for a Markovian quantum process, without any prior assumptions regarding the nature of the process beyond the physical necessity of complete positivity. This procedure should be widely useful in studies of dissipative quantum processes and in designing and testing new quantum information processing devices. We have further shown how one can use the simpler and more intuitive ‘‘Hadamard operator’’ formalism to extract the physical ‘‘noise generators’’ of the system from its full relaxation superoperator. We believe this two-step process is illustrative of how Quantum Process Tomography on many distinct kinds of physical systems should be done.

# Chapter 6

## Concatenated Quantum Error-Correcting Codes

Concatenated coding provides a general strategy to achieve the desired level of noise protection in quantum information storage and transmission. We report the implementation of a concatenated quantum error-correcting code able to correct against phase errors with a strong correlated component. The experiment was performed using nuclear magnetic resonance on a four spin subsystem of labeled crotonic acid. Our results show that concatenation between active and passive quantum error control codes may offer a practical tool to handle realistic error models contributed by both weak independent noise and strong correlated errors.

Reliable quantum information processing requires the ability to stabilize the information against noise due to both environmental interactions and operational imperfections. Among the various approaches which have been developed to cope with the effects of noise, and which include recent developments such as active dynamical decoupling methods [111, 112] and passive error-avoiding techniques [113, 114, 115, 91], quantum error-correcting codes (QECCs) [89, 90] have proven to date the only strategy carrying the potential for achieving fault-tolerance in scalable quantum information processors under a wide class of error models [116, 117, 48, 118, 119]. In particular, concatenated QECCs are the key ingredient to ensure that a final accuracy can be reached without requiring arbitrarily low error rates at any intermediate stage. The basic idea underlying concatenation is to use multiple levels of encoding to recursively obtain logical qubits with improved robustness properties. In its simplest setting, concatenation consists of hierarchically implementing a fixed QECC, under the assumption that the errors for the encoded information satisfy at each level appropriate independence assumptions [48]. For the procedure to be successful, it is critical that the implementation begins with sufficiently high fidelity, which in turn requires that the entry-level physical qubits are subjected to a sufficiently weak noise.

If small error rates are not available from the start, concatenation techniques may still prove valuable if the originating noise process is highly correlated in nature. This relies on the existence of efficient encodings based on decoherence-free subspaces (DFSs) [113, 114, 115] and noiseless subsystems (NSs) [91, 120, 121]. Because DFS/NS codes are tied to the occurrence of symmetries in the noise-inducing

interaction, they effectively provide passive, infinite-distance QECCs, capable of tolerating arbitrarily high error rates as long as the underlying symmetry is exact. While the infinite-distance behavior is not retained for imperfect symmetry, stability results ensure that the residual errors remain small if the symmetry is broken perturbatively, with short-time fidelity solely determined by the perturbing noise strength [115, 122, 123]. Concatenation schemes taking advantage of these features were originally developed in [124] and subsequently [125] in the context of the so-called cluster error model, where a dominant collective symmetry is perturbed by independent errors on individual qubits.

Here, we further explore theoretically and validate experimentally the usefulness of concatenating active and passive quantum error control codes. Our approach is tailored to realistic hybrid noise models where errors either do not follow a cluster pattern or, while being to a large extent independent, they are dominated by a large error rate which prevents quantum error correction from being affordable with available control resources. Two criteria emerge as general guiding principles in the design of the error control strategy: treating errors in order of their importance, by taking care of dominant errors first; and, at each stage, realizing logical qubits with reduced error rate, by seeking for appropriate subsystems of the previous level's qubits. Unlike the above-mentioned concatenation schemes, where physical qubits are uniformly replaced by logical ones at the first level of encoding, this generally results in schemes where such a replacement may happen only partially at a given stage, and physical and logical qubits are freely treated on the same ground as needed.

## 6.1 Concatenation between Active and Passive Error Control Codes

Let  $S$  be the quantum system of interest, and imagine that noise on  $S$  is to a good approximation Markovian. Then the state of  $S$  evolves as  $\rho_t = e^{\mathcal{L}t}[\rho_0]$ , where the infinitesimal noise super-operator  $\mathcal{L}$  takes the standard Lindblad form [94],

$$\mathcal{L}[\rho] = \sum_{\mu} \mathcal{D}_{L_{\mu}}[\rho] = \frac{1}{2} \sum_{\mu} \left( [L_{\mu}\rho, L_{\mu}^{\dagger}] + [L_{\mu}, \rho L_{\mu}^{\dagger}] \right). \quad (6.1)$$

Given the set of error generators  $\{L_{\mu}\}$ , a measure of the overall noise strength is given by  $\lambda = \sum_{\mu} |L_{\mu}|^2 + |\sum_{\mu} L_{\mu}^{\dagger} L_{\mu}|$ , where  $|X|$  is the maximum eigenvalue of  $\sqrt{X^{\dagger}X}$  [91]. For independent noise on qubits, each  $L_{\mu}$  involves a single-qubit Pauli operator, and  $\lambda$  can be thought of as resulting from the sum of the partial noise strengths  $\lambda_{\mu} = 2|L_{\mu}|^2$  associated to each error generator. In general, the error probability for information stored in  $S$  is a complicated function of time. By letting  $F_e(t)$  denote entanglement fidelity [44], one may write an error expansion

$$F_e(t) = 1 + \sum_{k=1}^{\infty} \frac{1}{k!} \left( \frac{t}{\tau_k} \right)^k, \quad (6.2)$$



where the  $k$ th order error rate  $1/|\tau_k^k|$  is upper-bounded by  $\lambda^k$ . If information is protected in a  $w$ -error-correcting code, error rates up to  $w$ th order are effectively canceled, improving the fidelity behavior as  $F_e(t) = 1 - O[(t/\tau_{w+1})^{w+1}] \geq 1 - O[(\lambda t)^{w+1}]$  [91]. The larger the window where  $F_e$  remains reasonably flat, the longer the time interval after which a one-time use of the code still succeeds at regaining the information with high fidelity. Since the former is basically determined by  $\lambda$ , the condition that noise is sufficiently weak is crucial for QEC to be practically useful.

We illustrate our error control methodology by focussing on a practically motivated example. Consider three physical qubits with independent phase errors. Strong noise on one of the qubits, say qubit 3, causes the overall strength to be too high for QEC to produce any significant improvement. However, noise on qubit 3 is dominated by correlated dephasing involving an additional qubit, say qubit 4. The error model can be specified in terms of the following operators:  $L_1 = \sqrt{\lambda_1}/2\sigma_z^1$ ,  $L_2 = \sqrt{\lambda_2}/2\sigma_z^2$ ,  $L_c = \sqrt{\lambda_c}/2(\sigma_z^3 + \sigma_z^4)$ ,  $L_r = \sqrt{\lambda_r}/2\sigma_z^3$ , for positive parameters  $\lambda_\mu$ ,  $\mu = 1, 2, c, r$ . Here,  $\lambda_1$  and  $\lambda_2$  are the strengths of the phase errors on qubits 1, 2, whereas  $\lambda_c$  and  $\lambda_r$  characterize the dominating (collective) and residual (independent) dephasing on qubit 3. For simplicity, we imagine a situation where  $|L_r|/|L_c| = \epsilon$ , with  $\epsilon < 1$ , and  $\lambda_1 \sim \lambda_2 \sim \lambda_r \sim \lambda_0 \sim \epsilon^2\lambda_c$ , in terms of two parameters  $\lambda_c$  and  $\epsilon$ . Physically, the collective and independent error processes affecting qubit 3 may or may not have the same origin. In the latter case (case *a*), qubits 3 and 4 are identically coupled to some environment, and qubit 3 is additionally weakly interacting with a second environment.  $L_c$  and  $L_r$  should be regarded as separate error generators, with an overall noise strength on qubit 3 given by  $\lambda_3 = \lambda_c(1 + \epsilon^2)$ . If the interaction involves a single environment instead (case *b*), then the symmetry between qubits 3 and 4 is perturbatively broken by independent errors on qubit 3. Accordingly,  $L_c$  and  $L_r$  should be combined into a single error generator  $L_3 = L_r + L_c$ , resulting in a noise strength  $\lambda_3 = \lambda_c(1 + \epsilon)^2$ . In both cases,  $\lambda \approx \lambda_c$  for  $\epsilon$  small enough.

Although the fact that the above error model is not cluster dephasing prevents from following a concatenation scheme analogous to [124], the presence of a strong correlated noise component still suggests to use passive error control codes as the first step toward reducing the noise effects. Let  $|0_L\rangle = |01\rangle_{34}$ ,  $|1_L\rangle = |10\rangle_{34}$  define logical DFS basis states for collective dephasing on qubits 3, 4 [1], and work with the new three-qubit system  $S'$  composed of the physical qubits 1, 2, and the resulting logical DFS qubit. Noise for  $S'$  can be analyzed by examining the action of the error generators on a state  $\tilde{\rho}$  that is properly initialized to  $S'$ . The basic observation is that, thanks to the degenerate action of  $L_c$  on DFS states [113, 114, 115, 1],  $L_c|i_L\rangle\langle j_L| = \ell|i_L\rangle\langle j_L|$  for some  $\ell$  ( $\ell = 0$  in our case), the errors caused by  $L_c$  and  $L_r$  on information encoded in  $S'$  can be described, in *both* cases *a* and *b*, as

$$\mathcal{D}_{L_c}[\tilde{\rho}] + \mathcal{D}_{L_r}[\tilde{\rho}] = \mathcal{D}_{L_r}[\tilde{\rho}]. \quad (6.3)$$

Thus, the effects of the strong collective noise disappear completely and, by noting that  $\sigma_z^3$  acts as an encoded  $\sigma_z^L$  observable [1], the residual noise from  $L_r$  corresponds to a logical dephasing process with a lower strength. The overall noise strength for  $S'$  becomes  $\lambda' = 3\lambda_0$ , suitable for further stabilization by an additional level of QEC.

In particular, a standard three-bit QECC is able to improve the ability of preserving one qubit from  $F_e^1(t) = 1 - O(\lambda_0 t)$  to  $F_e^{\text{qec},1}(t) = 1 - O[(\lambda_0 t)^2]$ .

Some generalizations of the above procedure are worth mentioning. For hybrid error models where strong correlated dephasing coexist with weak arbitrary single-qubit errors, concatenation between an “inner” DFS coding on the appropriate pairs and an “outer” five-bit QECC is applicable. If the strong noise processes involve full (non-abelian) collective errors, then three-bit NSs [91, 120, 41] offer the most efficient code to be used at the lowest level. In this case, the analysis is easier under the assumption that the residual error generators are in the commutant [91, 120] of the primary collective generators. This assumption, which parallels the *no-leakage* assumption of standard concatenated coding [48], ensures that the residual noise for the logical subsystem can be, as above, described in terms of encoded observables. Together with the identity action of the collective noise generators on the NS [91], this implies, similar to (6.3), that the effects of the strong noise component are fully eliminated after the first stage of encoding. Concatenation with finite-distance QEC can then further suppress errors. The no-leakage assumption can be relaxed at the expense of complicating the error control strategy. If the residual noise is allowed to cause leakage out of the logical subsystem, the effects appear at first more serious in the perturbative scenario *b*, as the action of  $\mathcal{D}_L$  would include, besides (6.3), additional terms mixing  $L_c$  and  $L_r$  or order  $\epsilon$  [115]. However, general stability results [122, 123] ensure that the contribution from these terms to all the error rates  $1/\tau_k^k$  remains of order  $\epsilon^2$ , as they are already in the independent scenario *a*. This makes concatenation with QEC still advantageous, provided that the procedure is modified to detect and handle leakage appropriately [124, 125, 126].

## 6.2 Experimental Implementation

The experiment implemented the DFS-QEC concatenation scheme for phase errors on three qubits (one of them being a logical DFS qubit) discussed earlier using liquid-state NMR techniques [67]. A 400 MHz Bruker AVANCE spectrometer was used with a sample of  $^{13}\text{C}$  labeled crotonic acid in a deuterated acetone solvent. The experiment combines basic steps used in the implementation of both finite-distance [31, 127] and infinite-distance QECCs [41, 1]. The quantum network is shown in Fig. 6-1 and the pulse sequence in Fig. 6-2. To implement the independent and collective noise, we combined the use of radio-frequency pulses with the non-unitary dynamics of magnetic field gradients integrated over the three independent directions of the spatially distributed sample [9], the different gradient strengths being calibrated to yield equal noise strengths on the different qubits. If  $k_i$  is the wavenumber of the gradient ramp along the  $i$ th axis [9], the phase coherence of the corresponding qubit averaged along that direction will be attenuated as  $\text{sinc}(k_i \frac{L_i}{2})$  where  $k_i = \gamma G_i t$ ,  $L_i$  being the length of the sample in the  $i$ th direction,  $\gamma$  the gyromagnetic ratio of

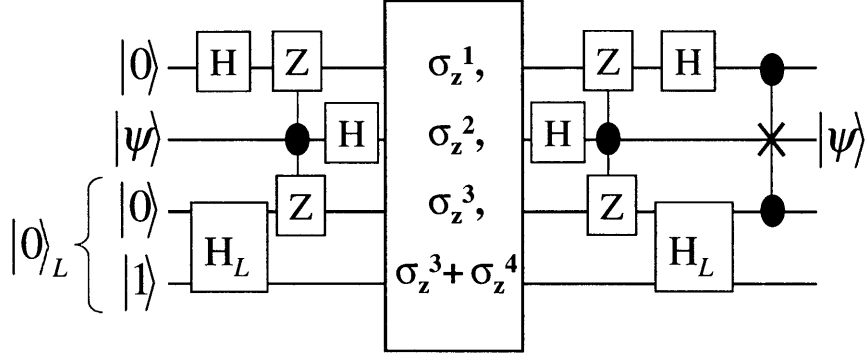


Figure 6-1: **Quantum network for the DFS-QEC concatenation scheme.** The second physical qubit from the top is the data qubit, while the first physical qubit and the third grouped with the fourth one are the ancillae and the logical ancillae respectively.  $H_L$  denotes a logical Hadamard operation [1]. The engineered noise implemented incoherent independent  $z$  noise on qubits 1, 2 and 3, in addition to a strong collective  $z$  noise on qubits 3 and 4 only.

the spin,  $G_i$  the gradient strength and  $t$  the duration of the gradient pulse <sup>2</sup>. The calibration mentioned above therefore yields  $k_i L_i = k_0 L$  where  $L$  is taken here to be the length of the sample in the  $z$  direction. Because the qubits are also subject to natural decoherence, the total time was kept constant in order to keep the relaxation effects the same while the value of  $k_i$  was swept over a given range. The sequence of pulses and magnetic field gradients applied to implement the specific incoherent noise is shown in Fig. 6-3. Because there are three independent directions, and due to the incoherent noise approach, we implemented case b, corresponding to a single environment coupled to spin 3.

Four different scenarios were investigated. First, the regular three-qubit QEC code with independent  $z$  noise was performed in order to provide a reference for the DFS-QEC concatenation scheme. If the scheme is indeed successful, then the former behavior should be recovered. Second, the same three-qubit code was also performed with a stronger collective  $z$  noise added on qubits 3 and 4 ( $k_c/k_r \sim 2$ ). QEC in these conditions in principle still works but its efficiency is greatly reduced. Finally, because the attenuation of the phase coherence still yields an initial slope equal to 0 even with no QEC at all, because of the incoherent nature of the implemented noise, we also carried out the experiment of applying the noise above on the different input states with no QEC, in order to demonstrate the improvement yielded by QEC. In each scenario, we prepared the conditional pseudo-pure states [67, 32]  $E_p \otimes \sigma_i \otimes E_p \otimes E_p$ , where  $E_p = |0\rangle\langle 0|$  and did the experiments for  $i = x, y$  and  $z$ . Four qubit and one qubit state tomography [52] were performed to determine the input and output states

<sup>2</sup>The sinc function arises from the Fourier transform of the spatial distribution of spins and is therefore valid if the sample can be considered rectangular.



Figure 6-2: **Pulse sequence for the DFS-QEC scheme.** The blocks represent selective one-qubit rotations while the bell-shapes represent magnetic field gradients. Each pulse is a strongly modulating pulse designed to be robust against RF inhomogeneity, and corrected using a feedback loop to counteract systematic errors. The experiment contains 83 pulses, 13 gradient pulses and lasts roughly 130 ms.

respectively, and their correlations. A total number of 18 readout pulses was used to determine the 4 qubit state while only two pulses were needed to reconstruct the state of qubit 2. To control the qubits, we used strongly modulating pulses designed to be robust against radio-frequency power inhomogeneity [128]. A feedback loop was also implemented in order to correct for systematic errors arising from the response of the electronics chain [129]. The protons were decoupled both during the experiment and acquisition to avoid additional incoherence and decoherence mechanisms, but at the expense of some nuclear Overhauser enhancement [47]. We stress that, once the NMR spectrometer had been calibrated and the pulses programmed, no further adjustments of any kind were required (or made) during the course of the measurements that made up this study.

### 6.3 Results

When the dynamics of the system is described by Eqn. 6.1, the entanglement fidelity with three-qubit QEC at noise strength  $\lambda_0$ , under the assumption of equally

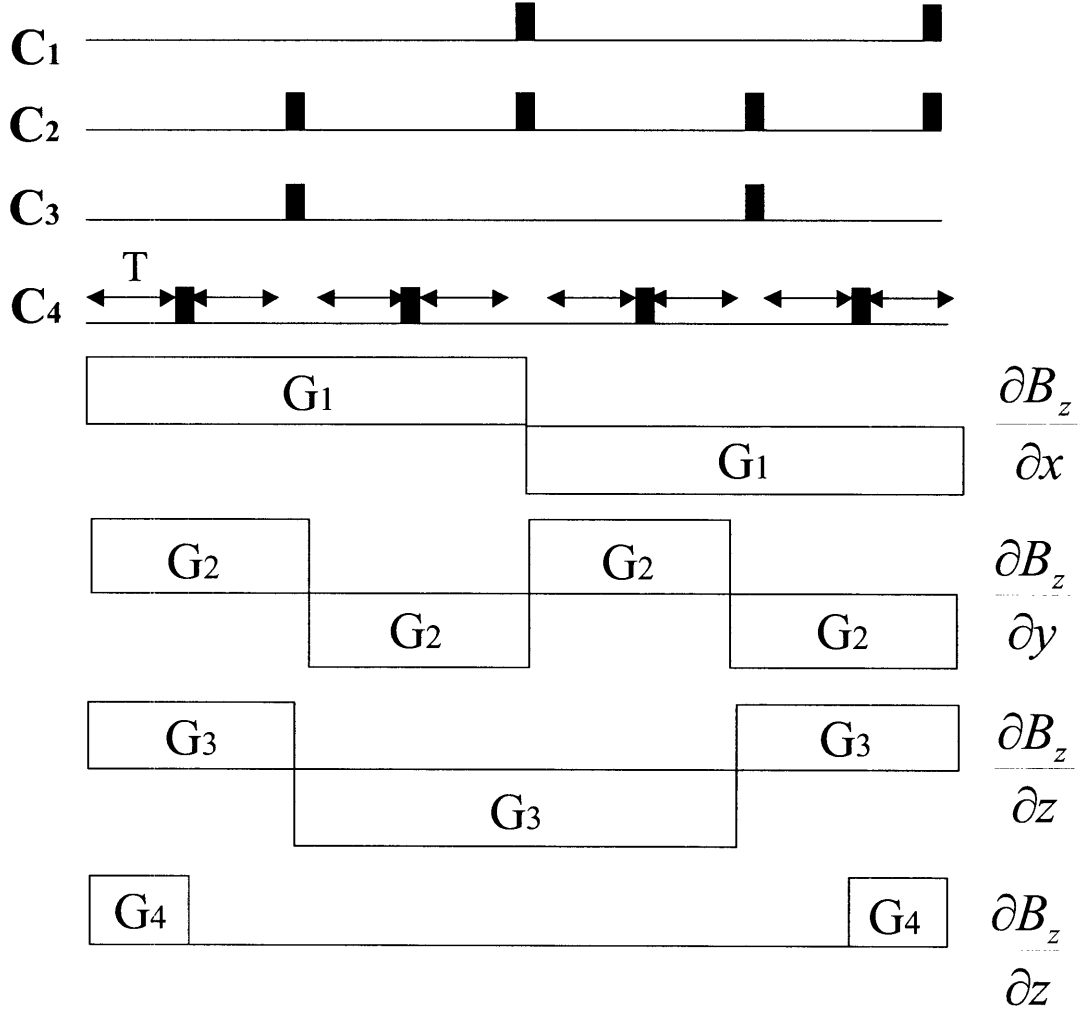


Figure 6-3: **Pulses and magnetic field gradients sequence to implement the noise.** The black boxes represent  $\pi$  pulses. The internal Hamiltonian is thereby refocused while encoding k-space components along different directions for the different qubits. The collective noise was also implemented using a magnetic field gradient in the  $z$  direction together with the weak  $z$  noise on the third physical qubit, thereby implementing the noise model b. Here  $T = 35 \mu s$ ,  $G_3 = 60 \times 2.6\% G/cm$ ,  $G_4 = 60 \times 20\% G/cm$ , and  $G_1$  and  $G_2$  were calibrated to yield the same attenuations as for  $G_3$  given the geometry of the sample ( $L_z \approx 1.6 cm$ ,  $L_x = L_y \approx 0.5 cm$ ) and unequal gradient strengths ( $G_z^{max} = 60 G/cm$ ,  $G_x^{max} = G_y^{max} \approx 46 G/cm$ ).

distributed, uncorrelated phase errors is given by [127]:

$$F_e^{\text{qec},1}(t) = \frac{1}{2} + \frac{1}{4} \left( 3e^{-\lambda_0 t} - e^{-3\lambda_0 t} \right) \quad (6.4)$$

while in the presence of the strong collective noise component and, again, with no correlation [127]:

$$F_e^{\text{qec},1}(t) = \frac{1}{2} + \frac{1}{4} \left( 2e^{-\lambda_0 t} + e^{-\lambda_3 t} - e^{-(2\lambda_0 + \lambda_3)t} \right). \quad (6.5)$$

In both cases, it can easily be seen that QEC corrects the effect of the noise to first order. However, for longer times it is clear that the collective noise part decreases the entanglement fidelity much faster. In the case of the incoherent noise we implemented, the previous equations become

$$F_e^{\text{qec},1}(t) = \frac{1}{2} + \frac{1}{4} \left( 3 \text{sinc}(k_0(t) \frac{L}{2}) - \text{sinc}^3(k_0(t) \frac{L}{2}) \right)$$

and

$$F_e^{\text{qec},1}(t) = \frac{1}{2} + \frac{1}{4} \left( 2 \text{sinc}(k_0(t) \frac{L}{2}) + \text{sinc}(k_3(t) \frac{L}{2}) - \text{sinc}^2(k_0(t) \frac{L}{2}) \text{sinc}(k_3(t) \frac{L}{2}) \right).$$

where  $k_3 = k_c + k_0$  for the case b we implemented. The first experimental results are shown in Fig. 6-4.a. The plots show the entanglement fidelity calculated for the four scenarios. The 4 qubit input state correlations with the desired states were calculated to be on average  $0.93 \pm 0.02$  after the state tomography procedure. First, it is clear that the QEC with independent noise plot (dots) shows some improvement compared with no QEC at all (squares). The "hump" was found to arise from imperfect initialization of the ancillae. Since this was unexpected, we provide a more detailed analysis of this effect in the next section. The QEC plot with additional strong collective noise (asterisks) also contains the same effect but is not as apparent. In any case, the efficiency of the QEC code with independent and strong collective noise is greatly reduced. The diamonds in the same figure show the DFS-QEC concatenated scheme result. The initial drop was mainly due to coherent errors caused by the longer pulse sequence necessary to perform such scheme, with additional decoherence induced by putting the 4th physical qubit in the transverse plane. Most of these results and effects are accounted for by extensive simulations including coherent and incoherent errors, in addition to imperfect readouts, that we present in the next section. Although the inflexion point of the DFS-QEC scheme seems to occur roughly at the same noise strength as for the QEC alone (with independent noise only), the standard QEC behavior reported in [31, 127] is not as transparent here. The entanglement fidelity being equal to  $F_e = (C_x + C_y + C_z + 1)/4$  in the case of a unital channel, and  $C_i = \frac{\text{tr}(\rho_{\text{in}} \cdot \rho_{\text{out}})}{\text{tr}(\rho_{\text{in}}^2)}$  (the density matrices in this formula are the second,

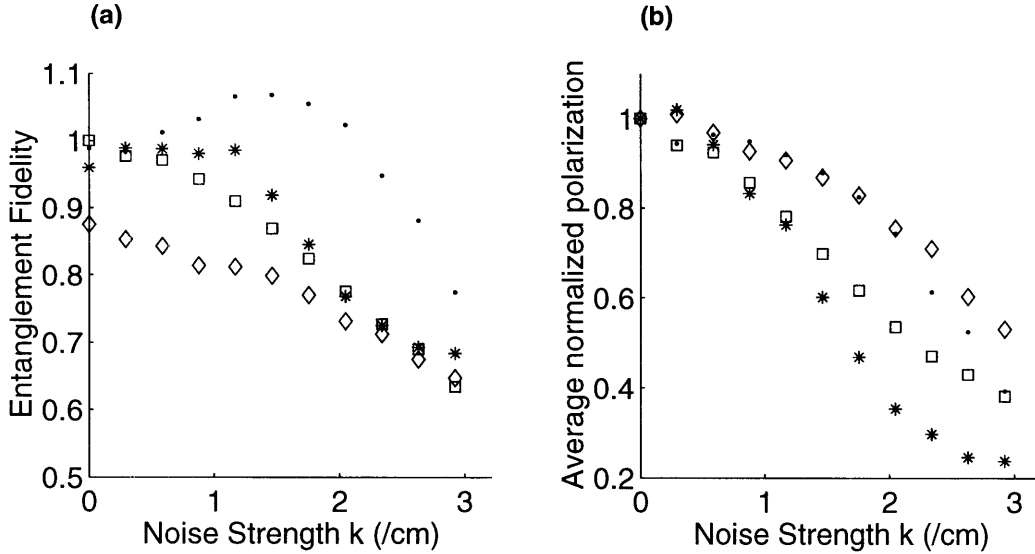


Figure 6-4: **Experimental results.** The dots correspond to the 3-qubit QEC scenario with independent  $z$  noise only while the asterisks correspond to the same scenario but with additional strong collective noise, and  $k(t) = k_0(t)$ . The squares correspond to the No QEC scenario and the diamonds to the DFS-QEC scheme. There is an error bar of  $\pm 0.02$  for each data point which is not displayed here for the sake of clarity. (a) Entanglement fidelity results (see text for an explanation of the different effects). (b) Average normalized polarization of the output states (see text).

or data, qubit density matrix obtained by tracing over the three other qubits), this metric is clearly sensitive to the direction and length of the output states. For that reason, we also calculated the normalized polarization  $\frac{\text{tr}(\rho_{\text{out},n}^2)}{\text{tr}(\rho_0^2)}$  where  $\rho_0$  and  $\rho_{\text{out},n}$  are the outputs at zero noise and noise index  $n$  respectively for the three input states ( $\rho_0 = \rho_{\text{out},0}$ ), and took the average (this metric is also used in [130]). The results are shown in Fig. 6-4.b. These are now more transparent and clearly demonstrate the gain one would obtain by using the DFS-QEC concatenation scheme, if there were no coherent errors and no initial loss of polarization. The QEC behavior with independent noise only (dots) is recovered quite well by the DFS-QEC concatenated scheme with both independent and collective noise (diamonds). Further analysis of the data revealed that the hump noticeable in Fig. 6-4.a is still present but much less important because of the insensitivity of the new metric concerning the initial coherent errors in  $\rho_{\text{out},0}$ .

## 6.4 Discussion

The results in Fig. 6-4.a, since they are not as transparent as in [31, 127], or even surprising, deserve special attention. To understand the different features of the data, we carried out extensive numerical simulations that we present here. Only the four

qubits used in the crotonic acid sample were taken into account, thereby reducing the size of the Hilbert space by a factor of 8 and making the simulations more doable. By doing so, we neglect the imperfect decoupling of the protons. But independent simulations justify this approximation.

The simulations were therefore done on the four qubit system with radio-frequency power inhomogeneity, starting from the measured experimental pseudo-pure input states. The tomographic procedure makes use of the knowledge of the simulated unitary readout pulses, although the true evolution is not unitary because of RF inhomogeneity and relaxation. This imperfection was taken into account by simulating the incoherent evolution but still assuming unitary dynamics in the evolution for the reconstruction of the density matrix<sup>3</sup>, the main goal here being to reproduce faithfully the experimental results. Because the length of the experiment is roughly equal to  $T_2/5$ , simulating relaxation would certainly provide valuable information but this was not done for convenience (the size of the superoperator in this case is  $256 \times 256$ ). Furthermore, the coherent and incoherent evolution of the 4 qubits seemed to be enough to explain most of the features observed in the experiment. To simulate the engineered noise, we attenuated the density matrix elements consistently with the noise model we implemented [9]. A matrix element  $|i, j, k\rangle\langle m, n, r|$  ( $i, j, k, m, n, r = 0$  or  $1$ ) is attenuated as  $\text{sinc}(|i - m|G_1\gamma T \frac{L_x}{2})\text{sinc}(|j - n|G_2\gamma T \frac{L_y}{2})\text{sinc}(|k - r|G_3\gamma T \frac{L_z}{2})$  for the independent noise model, while in the case of the independent noise model plus the collective noise (scenario b), a matrix element  $|i, j, k, l\rangle\langle m, n, r, s|$  is attenuated as  $\text{sinc}(|i - m|G_1\gamma T \frac{L_x}{2})\text{sinc}(|j - n|G_2\gamma T \frac{L_y}{2})\text{sinc}(|k - r|G_3 + |(k - r) + (l - s)|G_4)\gamma T \frac{L_z}{2})$  (see Fig. 6-3 for an explanation of the different variables). The results of the simulation are shown in Fig. 6-5. We see that most features observed in the experiment are reproduced here. The drop between the QEC-DFS and the QEC alone scenarios is mainly due to coherent and incoherent errors caused by the longer sequence involved in the former case. The behavior of the initial portion of the QEC with collective noise is also reproduced. It is worth however pointing out that the experimental entanglement fidelity is initially higher than what the simulations predict. This can be due to some nuclear Overhauser enhancement in addition to some coherent errors. Since we are tracing over qubits 1, 3 and 4, coherent errors on the four-qubit system can yield sensitive "artificial" enhancement on the second qubit. One can finally observe also in the simulations the "hump" in the QEC scenario alone. We now investigate the origin of this unexpected result.

To answer this question, we shall do an analysis of a three-qubit system under ideal encoding, decoding and noise implementation (for the three qubit phase flip quantum error correction code). We will indeed show that this effect is due to the imperfect initialization of the ancillae so that dealing with four qubits and real implementations is not necessary. Say the starting state of the system is

$$\rho_{in} = (1 - \beta)\frac{I}{8} + \beta|0\rangle\langle 0| \otimes (E_p + \epsilon_2\sigma_z^2) \otimes (E_p + \epsilon_3\sigma_z^3),$$

---

<sup>3</sup>Relaxation during the readout pulses can be safely neglected because of their short lengths compared to typical  $T_2$  times.



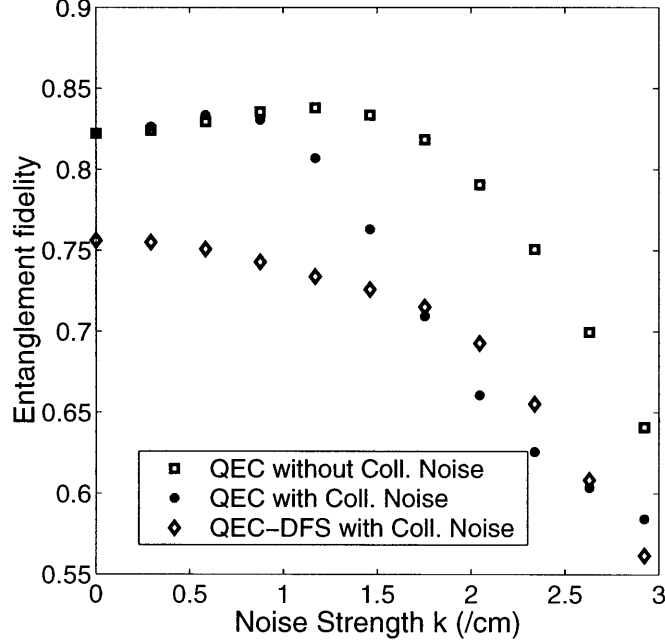


Figure 6-5: **Simulation of the DFS-QEC concatenation experiment.** Most of the experimental features, i.e. the "hump" in addition to the drop of the QEC-DFS scenario compared to the QEC alone are reproduced. The "hump" is due to an imperfect initialization of the ancillae (see text for a detailed explanation). The drop mentioned above on the other hand is primarily due to coherent and incoherent errors because of the longer sequence (more pulses) for the QEC-DFS scheme. We add here for clarity that  $k(t) = k_0(t)$ .

where  $E_p = |0\rangle\langle 0|$  and we assume  $\beta \geq 0$ . Qubit 1 is the data qubit. We will worry about the validity of the initial density matrix at the end of the analysis. We now apply the encoding sequence  $U_{enc}$  of the three qubit phase error code and then the  $\{\sigma_z^1, \sigma_z^2, \sigma_z^3\}$  noise. Such a noise will attenuate terms like  $\sigma_x^i$  as  $e^{-\lambda t}$  independently of the product operators corresponding to the other qubits. If we describe such evolution by the superoperator  $\Lambda(\rho)(t)$ , the previous state becomes

$$\begin{aligned} \Lambda(U_{enc}\rho_{in}U_{enc}^\dagger)(t) &= \frac{I}{8} + \frac{\beta}{8}e^{-\lambda t}(\sigma_x^1 + (1 + 2\epsilon_2)\sigma_x^2 + (1 + 2\epsilon_3)\sigma_x^3) + \\ &\frac{\beta}{8}e^{-2\lambda t}((1 + 2\epsilon_2)\sigma_x^1\sigma_x^2 + (1 + 2\epsilon_3)\sigma_x^1\sigma_x^3 + 2(\epsilon_2 + \epsilon_3 + 2\epsilon_2\epsilon_3)\sigma_x^2\sigma_x^3) + \\ &\frac{\beta}{8}e^{-3\lambda t}(1 + 2\epsilon_2 + 2\epsilon_3 + 4\epsilon_2\epsilon_3)\sigma_x^1\sigma_x^2\sigma_x^3. \end{aligned}$$

Applying the decoding sequence  $U_{dec}$  and tracing over qubits 2 and 3 then yields

$$\begin{aligned} tr_{2,3}(U_{dec}\Lambda(U_{enc}\rho_{in}U_{enc}^\dagger)(t)U_{dec}^\dagger) &= \frac{I}{2} + \frac{\beta}{4}((3 + 2\epsilon_2 + 2\epsilon_3)e^{-\lambda t} \\ &\quad - (1 + 2\epsilon_2 + 2\epsilon_3 + 4\epsilon_2\epsilon_3)e^{-3\lambda t})\sigma_z, \end{aligned}$$

while  $\text{tr}_{2,3}(\rho_{in}) = \rho_{1,\text{in}} = \frac{I}{2} + \frac{\beta}{2}\sigma_z$ . We immediately see that at  $t = 0$ ,  $\rho_{1,\text{out}} \neq \rho_{1,\text{in}}$  unless  $\epsilon_2$  or  $\epsilon_3$  is equal to 0. This is because a coherent error is in this case introduced by the Toffoli gate in the decoding sequence and because  $U_{\text{dec}} \neq U_{\text{enc}}^\dagger$ . We now calculate the attenuated correlation  $C(t) = \frac{\text{tr}(\rho_{1,\text{in}} \cdot \rho_{1,\text{out}}(t))}{\text{tr}(\rho_{1,\text{in}}^2)}$ . From the previous expressions, we obtain

$$C(t) = \frac{1}{\frac{1}{2} + \frac{\beta^2}{2}} \left( \frac{1}{2} + \frac{\beta^2}{4} ((3 + 2\epsilon_2 + 2\epsilon_3)e^{-\lambda t} - (1 + 2\epsilon_2 + 2\epsilon_3 + 4\epsilon_2\epsilon_3)e^{-3\lambda t}) \right). \quad (6.6)$$

We wish to maximize  $C(t)$  with respect to  $t$ ,  $\epsilon_2$  and  $\epsilon_3$ . Finding  $t_m = t$  such that  $\frac{dC}{dt}(t) = 0$  yields

$$C(t_m) = \frac{1}{\frac{1}{2} + \frac{\beta^2}{2}} \left( \frac{1}{2} + \frac{\beta^2}{6\sqrt{3}} \frac{(3 + 2\epsilon_2 + 2\epsilon_3)^{\frac{3}{2}}}{(1 + 2\epsilon_2 + 2\epsilon_3 + 4\epsilon_2\epsilon_3)^{\frac{1}{2}}} \right).$$

Note that if  $\epsilon_3 = 0$  and  $\epsilon_2 < 0$ , one would find  $t_m < 0$  and the slope equal to 0 would occur at negative times ( $t_m = \frac{1}{2\lambda} \ln(\frac{3(1+2\epsilon_2+2\epsilon_3+4\epsilon_2\epsilon_3)}{3+2\epsilon_2+2\epsilon_3})$ )! The problem being symmetric with respect to  $\epsilon_2$  and  $\epsilon_3$ , we shall now maximize  $C(t_m)$  with  $\epsilon_2 \geq \epsilon_3$ . We first take the derivative of  $C(t_m)$  with respect to  $\epsilon_2$  and find, because  $\epsilon_2 \geq \epsilon_3$  that  $C(t_m)$  is an increasing function with respect to  $\epsilon_2$ . Hence, we have  $C(t_m, \epsilon_2 > \epsilon_3) > C(t_m, \epsilon_2 = \epsilon_3) > 1$ . Because  $C(t_m, \epsilon_2)$  is an increasing function of  $\epsilon_2$ , we want to make the latter variable as large as possible. In addition,  $\beta$  should also be as large as possible provided the initial density matrix is physically valid. Let us call  $f = \frac{(3+2\epsilon_2+2\epsilon_3)^{\frac{3}{2}}}{(1+2\epsilon_2+2\epsilon_3+4\epsilon_2\epsilon_3)^{\frac{1}{2}}}$  so that  $\frac{df}{d\epsilon_3} = 2 \frac{(2\epsilon_3 - \epsilon_2)(3+2\epsilon_2+2\epsilon_3)^{\frac{1}{2}}}{(1+2\epsilon_2)^{\frac{1}{2}}(1+2\epsilon_3)^{\frac{3}{2}}}$  for a given  $\epsilon_2$ . Since  $f(\epsilon_3)$  is differentiable on the interval  $[0; \epsilon_2]$ , every global extremum must be a local extremum or an endpoint extremum, meaning  $\epsilon_3 = 0$ ,  $\epsilon_3 = \epsilon_2$  or  $\epsilon_3 = \frac{\epsilon_2}{2}$ . Further inspection of  $\frac{df}{d\epsilon_3}$  indicates that the latter possibility corresponds in fact to a minimum. For a given  $\epsilon_2$  the global maximum for  $\epsilon_3 \in [0; \epsilon_2]$  therefore is an endpoint maximum. Now because  $f(\epsilon_2, 0) \geq f(\epsilon_2, \epsilon_3 = \epsilon_2)$ , the global maximum will be obtained for  $\epsilon_3 = 0$ , i.e. only the second (or third) ancillae is wrongly initialized. The last thing to do now is to find  $\epsilon_2$  and  $\beta$  that maximize  $C(t_m)$  and which makes  $\rho_{in}$  a valid density matrix. We find  $\max(C(t_m)) \approx 1.00341$  for  $\beta \approx 0.200$  and  $\epsilon_2 \approx 0.497$  (i.e.  $\epsilon_2 = \frac{1}{8}(\frac{1}{\beta} - 1)$ ).

One therefore finds that an imperfect initialization of the ancillae can yield  $\frac{dC}{dt} = 0$  at a time  $t_m > 0$  leading to an initial increase in the correlation (reaching  $C(t_m) > 1$ ). It is also worth pointing out that according to Eqn. 6.6, we have  $\frac{dC}{dt}|_{t=0} = \frac{\beta^2\lambda}{1+\beta^2}$  for  $\epsilon_2 \approx 0.5$ . For this class of initial states, QEC therefore improves the entanglement fidelity from  $F_e(t) = 1 - O(\lambda t)$  to  $F_e(t) = 1 + O(\lambda t)$  for short enough times, as opposed to  $F_e(t) = 1 - O[(t/\tau_2)^2]$  for pure initial states. The initial slope increases linearly with  $\lambda$  while the time at which it starts losing information decreases as  $1/\lambda$ . One could also show easily that the purity (the entropy) of the first qubit is also initially increased (decreased) in this case. The analysis on other input states would lead to the same result (except for the  $|+\rangle$  state which yields an eigenstate of the noise and therefore remains unaffected throughout). Because the encoding-

noise-decoding sequence can presumably be expressed as a unital channel, it seems at first sight that this observation violates the theorem stating that a unital channel outputs non-decreasing entropy states [131]. The theorem however does not apply here because qubit 1 starts in a non-separable state, making linear quantum channels results inapplicable. We provide in Fig. 6-6 an ideal simulation demonstrating the "hump" effect for  $\epsilon_2 = 0.497$  and  $\beta = 0.2$ . The numerical simulation confirms the theoretical results derived throughout this section. It is worth saying that, as can

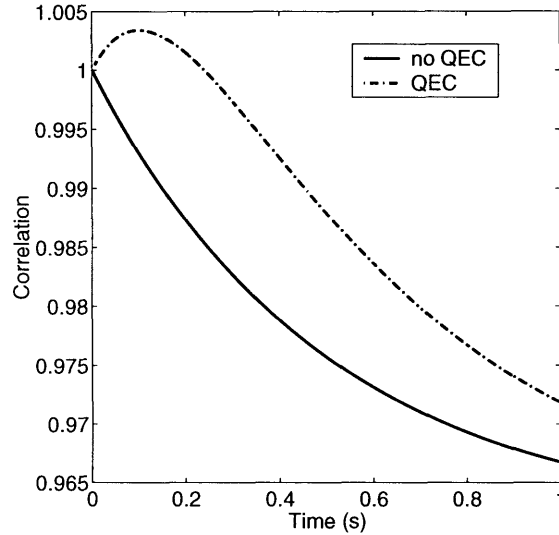


Figure 6-6: **Illustration of the "hump" effect (ideal simulation).** The maximum correlation for the QEC case is  $\sim 1.00341$  as predicted by the analysis.

be seen from the plot, it is a small effect when one is interested in the correlation, the purity or the entropy. This is because  $I$  is preserved throughout and that the QEC code acts only on the deviation from identity of the density matrix, i.e. on the polarization (scaled down by  $\beta = 0.2$  and therefore less important). It can be shown however that this 0.34% increase in the correlation actually corresponds to a 8.79% increase in the polarization. Since in NMR QIP we deal with pseudo-pure states and therefore look mostly at the deviation of the density matrix from identity, this explains why in the experiment, and in the simulation, the effect appears bigger. It also occurs only when dealing initially with mixed states. If one had  $\beta = 1$ , implying the state of the first qubit  $\rho_{1,\text{in}}$  to be pure, one would be forced to set  $\epsilon_2 \leq 0$  to have an initial positive semi-definite density matrix and there would be no hump. Another possible way of seeing it is that if the data qubit is pure, it is necessarily separable from the other qubits and therefore the entropy non-decreasing theorem of unital channels holds.

## 6.5 Conclusion

We have demonstrated here sufficient control to implement a DFS-QEC concatenated scheme on a 4-qubit system. Although we did not truly implement a quantum memory, we clearly showed the potential of combining such techniques and we explained most experimental results by thorough simulations. By doing the experiment, we furthermore discovered an effect suggesting that QEC can in some cases purify the initial data qubit, for which we provided an analysis. Our results further support the hope that, for realistic errors in physical systems, clever concatenation between active and passive error control codes carries the potential of practically realizing fault-tolerance in quantum information processing.

# Bibliography

- [1] E. M. Fortunato, L. Viola, J. Hodges, G. Teklemariam, and D. G. Cory. Implementation of universal control on a decoherence-free qubit. *New Journal of Physics*, 4:5.1–20, 2002.
- [2] R. Feynman. Simulating physics with computers. *International Journal of Theoretical Physics*, 21(6-7):467–88, 1982.
- [3] P. W. Shor. Polynomial-time algorithms for prime factorization and discrete logarithms on a quantum computer. *Siam. J. Comput.*, 26:1484–1509, 1997.
- [4] I. I. Rabi, S. Millman, P. Kusch, and J. R. Zacharias. The molecular beam resonance method for measuring nuclear magnetic moments. *Physical Review*, 55:526–535, 1939.
- [5] U. Haeberlen and J. S. Waugh. Coherent averaging effect in magnetic resonance. *Physical Review*, 175:453–67, 1968.
- [6] A. F. Haught. Lasers and their applications to physical chemistry. *Annual Review of Physics and Chemistry*, 19:343, 1968.
- [7] W. S. Warren, H. Rabitz, and M. Dahleh. Coherent control of quantum dynamics - the dream is alive. *Science*, 259:1581–9, 1993.
- [8] W. S. Warren. Effects of pulse shaping in laser spectroscopy. *Science*, 242:878–84, 1988.
- [9] A. Sodickson and D. G. Cory. A generalized  $k$ -space formalism for treating the spatial aspects of a variety of n. m. r. experiments. *Progress in Nuclear Magnetic Resonance Spectroscopy.*, 33:77–108, 1998.
- [10] C. Counsell, M. H. Levitt, and R. R. Ernst. Analytic theory of composite pulses. *Journal of Magnetic Resonance*, 63:133–41, 1985.
- [11] S. Connolly, D. Nishimura, and A. Macovski. Optimal control solutions to magnetic resonance selective excitation problem. *IEEE Transactions on Medical Imaging*, MI-5:106–15, 1986.
- [12] R. Tycko, E. Schneider, and A. Pines. Broadband population inversion in solid state n. m. r. *Journal of Chemical Physics*, 81:680–8, 1984.

- [13] P. G. Morris, D. E. Rourke, D. J. O. McIntyre, and A. Al-Beshr. New approaches to selective pulse design. *Magnetic Resonance Materials in Physics, Biology, & Medicine*, 2:279–83, 1994.
- [14] J. Stoustrup, O. Schedletzy, S. J. Glasser, C. Griesinger, N. C. Nielsen, and O. W. Sørensen. Generalized bound on quantum dynamics: efficiency of unitary transformations between non-hermitian states. *Physical Review Letters*, 74:2921–4, 1995.
- [15] L. Emsley and G. Bodenhausen. Optimization of shaped selective pulses for n. m. r. using a quaternion description of their overall propagators. *Journal of Magnetic Resonance*, 97:135–48, 1992.
- [16] H. Green and R. Freeman. Band-selective radiofrequency pulses. *Journal of Magnetic Resonance*, 93:93–141, 1991.
- [17] B. Ewing, S. J. Glasser, and G. P. Drobny. Experimental demonstrations of shaped pulses for narrowband inversion of uncoupled and coupled systems. *Journal of Magnetic Resonance*, 98:381–7, 1992.
- [18] J. L. Schiano, A. G. Webb, and R. L. Magin. Feedback control of the nuclear magnetization state: experimental results. *IEEE Transactions on Medical Imaging*, 11:203–14, 1992.
- [19] A. P. Peirce, M. Dahleh, and H. Rabitz. Optical control of quantum mechanical systems: existence, numerical approximations and applications. *Physical Review A*, 37:4950–64, 1988.
- [20] W. S. Warren and A. H. Zewail. Multiple phase-coherent laser pulses in optical spectroscopy. i. the technique and experimental applications. *Journal of Chemical Physics*, 78:2279–97, 1983.
- [21] M. Dahleh, A. P. Peirce, and H. Rabitz. Optimal control of uncertain quantum systems. *Physical Review A*, 42:1065–79, 1990.
- [22] A. Assion, T. Baumert, M. Bergt, T. Brixner, B. Kiefer, V. Seyfried, M. Strehle, and G. Gerber. Control of chemical reactions by feedback-optimized phase-shaped femtosecond laser pulses. *Science*, 282:919–22, 1998.
- [23] B. J. Pearson, J. L. White, T. C. Weinacht, and P. H. Bucksbaum. Coherent control using adaptive learning algorithms. *Physical Review A*, 63:063412, 2001.
- [24] A. Sørensen and K. Molmer. Ion trap quantum computer with bichromatic light. *Fortschritte der Physik-Progress of Physics*, 48:811–21, 2000.
- [25] D. Kielpinski, V. Meyer, M. A. Rowe, C. A. Sackett, W. M. Itano, C. Monroe, and D. J. Wineland. A decoherence-free quantum memory using trapped ions. *Science*, 291:1013–1015, 2001.

- [26] D. G. Cory, A. F. Fahmy, and T. F. Havel. Ensemble quantum computing by nuclear magnetic resonance spectroscopy. *Proceedings of the National Academy of Science*, 94:1634–1639, 1997.
- [27] N. A. Gershenfeld and I. L. Chuang. Bulk spin-resonance quantum computation. *Science*, 275:350–356, 1997.
- [28] J. A. Jones and M. Mosca. Implementation of a quantum algorithm on a nuclear magnetic resonance quantum computer. *Journal of Chemical Physics*, 109:1648–1653, 1998.
- [29] I. L. Chuang, N. Gershenfeld, M. Kubinec, and D. Leung. Experimental implementation of fast quantum searching. *Physical Review Letters*, 80:3408–11, 1998.
- [30] Y. S. Weinstein, M. A. Pravia, E. M. Fortunato, S. Lloyd, and D. G. Cory. Implementation of the quantum fourier transform. *Physical Review Letters*, 86:1889–91, 2001.
- [31] D. G. Cory, W. Maas, M. Price, E. Knill, R. Laflamme, W. H. Zurek, T. F. Havel, and S. S. Somaroo. Experimental quantum error correction. *Physical Review Letters*, 81:2152–5, 1998.
- [32] E. Knill, R. Laflamme, R. Martinez, and C. Negrevergne. Benchmarking quantum computers: the five-qubit error correcting code. *Physical Review Letters*, 86:5811–4, 2001.
- [33] S. Somaroo, C.-H. Tseng, T. F. Havel, R. Laflamme, and D. G. Cory. Quantum simulations on a quantum computer. *Physical Review Letters*, 82:5381–84, 1999.
- [34] F. Bloch and A. Siegert. Magnetic resonance for nonrotating fields. *Physical Review*, 57:522–527, 1940.
- [35] M. Steffen, L. M. K Vandersypen, and I. L. Chuang. Simultaneous soft pulses applied at nearby frequencies. *Journal of Magnetic Resonance*, 146:369–74, 2000.
- [36] E. Knill, R. Laflamme, R. Martinez, and C-H. Tseng. An algorithmic benchmark for quantum information processing. *Nature*, 404:368–70, 2000.
- [37] E.L. Hahn. Spin echoes. *Physical Review*, 90:580–594, 1950.
- [38] H. Y. Carr and E. M. Purcell. Effects of diffusion on free precession in nuclear magnetic resonance experiments. *Physical Review*, 94:630–638, 1954.
- [39] S. Meiboom and D. Gill. Modified spin-echo method for measuring nuclear relaxation times. *Review of Scientific Instruments*, 29:688–691, 1958.

- [40] G. Teklemariam, E. M. Fortunato, M. A. Pravia, T. F. Havel, and D. G. Cory. N. m. r. analog of the quantum disentanglement eraser. *Physical Review Letters*, 86:5845–49, 2001.
- [41] L. Viola, E. M. Fortunato, M. A. Pravia, E. Knill, R. Laflamme, and D. G. Cory. Experimental realization of noiseless subsystems for quantum information processing. *Science*, 293:2059–63, 2001.
- [42] J. Huth, N. D. Kurur, and G. Bodenhausen. Multiple-frequency decoupling in selective correlation spectroscopy. *Journal of Magnetic Resonance*, 118:286–90, 1996.
- [43] R. E. Gordon, P. E. Hanley, D. Shaw, D. G. Gadian, G. K. Radda, P. Styles, P. J. Bore, and L. Chan. Localization of metabolites in animals using  $^{31}\text{P}$  topical magnetic resonance. *Nature*, 287:736–8, 1980.
- [44] B. Schumacher. Sending entanglement through noisy quantum channels. *Physical Review A*, 54:2614–28, 1996.
- [45] S. Lloyd. Almost any quantum logic gate is universal. *Physical Review Letters*, 75:346–9, 1995.
- [46] J. A. Nelder and R. Mead. A simplex method for function minimization. *Comput. J. (UK)*, 7:308–13, 1965.
- [47] R. R. Ernst, G. Bodenhausen, and A. Wokaun. *Principles of Nuclear Magnetic Resonance in One and Two Dimensions*. Oxford University Press, Oxford, 1994.
- [48] E. Knill, R. Laflamme, and W. H. Zurek. Resilient quantum computation. *Science*, 279:342–5, 1998.
- [49] D. G. Cory. A dante-based method for radiofrequency-field selection. *Journal of Magnetic Reson*, 103:23–6, 1993.
- [50] J. S. Waugh. Theory of broadband decoupling. *Journal of Magnetic Reson*, 50:30–49, 1982.
- [51] J. A. Jones and E. Knill. Efficient refocussing of one spin and two spin interactions for n. m. r. quantum computing. *Journal of Magnetic Resonance*, 141:322–5, 1999.
- [52] I. L. Chuang, N. Gershenfeld, M. Kubinec, and D. Leung. Bulk quantum computation with nuclear magnetic resonance: theory and experiment. *Proceedings of the Royal Society of London, Series A*, 454:447–67, 1998.
- [53] K. Kraus. *States, Effects, and Operations*. Springer-Verlag, New York, 1983.
- [54] M. A. Nielsen and I. L. Chuang. *Quantum Computation and Quantum Information*. Cambridge University Press, Cambridge, UK, 2000.



- [55] R. J. Gordon and S. A. Rice. Active control of the dynamics of atoms and molecules. *Annu. Rev. Phys. Chem.*, 48:601–641, 1997.
- [56] S. A. Rice and S. P. Shah. Active control of product selection in a chemical reaction: a view of the current scene. *Phys. Chem. Chem. Phys.*, 4(10):1683–1700, 2002.
- [57] M. H. Levitt and R. Freeman. NMR population-inversion using a composite pulse. *J. Magn. Reson.*, 33:473–476, 1979.
- [58] M. H. Levitt. Symmetrical composite pulse sequences for NMR population inversion. 1. Compensation of radiofrequency field inhomogeneity. *J. Magn. Reson.*, 48:234–264, 1982.
- [59] R. Tycko. Broad-band population-inversion. *Phys. Rev. Lett.*, 51:775–777, 1983.
- [60] A.J. Shaka and R. Freeman. Composite pulses with dual compensation. *J. Magn. Reson.*, 55:487–93, 1983.
- [61] M. H. Levitt. Composite pulses. *Prog. Nucl. Magn. Reson. Spect.*, 18:61–122, 1986.
- [62] J. Baum, R. Tycko, and A. Pines. Broad-band and adiabatic inversion of a 2-level system by phase-modulated pulses. *Phys. Rev. A*, 32:3435–3447, 1985.
- [63] M. S. Silver, R. I. Joseph, and D. I. Hoult. Selective spin inversion in nuclear magnetic-resonance and coherent optics through an exact solution of the bloch-riccati equation. *Phys. Rev. A*, 31:2753–2755, 1985.
- [64] H. K. Cummins and J. Jones. Use of composite rotations to correct for systematic errors in nmr quantum computation. *New J. Phys.*, 2:6.1–6.12, 2000.
- [65] H. K. Cummins, G. Llewellyn, and J. A. Jones. Tackling systematic errors in quantum logic gates with composite rotations. *Phys. Rev. A*, 67:042308, 2003.
- [66] J. A. Jones. NMR quantum computing. *Prog. in NMR Spect.*, 38(4):325–60, 2001.
- [67] D. G. Cory, R. Laflamme, E. Knill, L. Viola, T. F. Havel, N. Boulant, G. Boutis, E. Fortunato, S. Lloyd S, R. Martinez R, C. Negrevergne, M. Pravia, Y. Sharf, G. Teklemariam, Y. S. Weinstein, and W. H. Zurek. NMR based quantum information processing: achievements and prospects. *Prog. Phys.*, 48:875–907, 2000.
- [68] T. F. Havel. Procedures for converting among lindblad, kraus and matrix representations of quantum dynamical semigroups. *Journal of Mathematical Physics*, 44:534, 2003.
- [69] D. Leung. Towards robust computation. *PhD thesis*, 2000. Stanford university.

- [70] L. J. Landau and R. F. Streater. On birkhoff's theorem for doubly stochastic completely positive maps of matrix algebras. *Lin. Alg. Appl.*, 193:107–127, 1993.
- [71] N. Boulant, K. Edmonds, J. Yang, M. A. Pravia, and D. G. Cory. Experimental demonstration of an entanglement swapping operation and improved control in nmr quantum information processing. *Physical Review A*, 68:032305, 2003.
- [72] Y. Weinstein, T. F. Havel, J. Emerson, N. Boulant, M. Saraceno, S. Lloyd, and D. G. Cory. Quantum process tomography of the quantum fourier transform. *Journal of Chemical Physics*, 68:032305, 2004.
- [73] N. Boulant, S. Furuta, J. Emerson, T. F. Havel, and D. G. Cory. Incoherent noise and quantum information processing. *Journal of Chemical Physics*, 68:032305, 2004.
- [74] I. L. Chuang and M. A. Nielsen. Prescription for experimental determination of the dynamics of a quantum black box. *Journal of Modern Optics*, 44:2455–67, 1997.
- [75] A. M. Childs, I. L. Chuang, and D. W. Leung. Realization of quantum process tomography in n. m. r. *Physical Review A*, 64:012314/1–7, 2001.
- [76] J. F. Poyatos, J. I. Cirac, and P. Zoller. Complete characterization of a quantum process: the two-bit quantum gate. *Physical Review Letters*, 78:390, 1997.
- [77] N. Boulant, T. F. Havel, M. A. Pravia, and D. G. Cory. A robust method for estimating the lindblad operators of a dissipative process from the measurement of the density operator at several time points. *Physical Review A*, 67:042322, 2003.
- [78] J. W. Pan, D. Bouwmeester, H. Weinfurter, and A. Zeilinger. Experimental entanglement swapping: Entangling photons that never interacted. *Phys. Rev. Lett.*, 80:3891–3894, 1998.
- [79] A. Cabello. Quantum correlations are not local elements of reality. *Phys. Rev. A*, 59:113–115, 1999.
- [80] T. F. Havel, S. S. Somaroo, C. H. Tseng, and D. G. Cory. *Applic. Alg. Eng., Commun. Comput.*, 10:339–374, 2000.
- [81] S. L. Braunstein, C. M. Caves, R. Jozsa, N. Linden, S. Popescu, and R. Schack. Separability of very noisy mixed states and implications for nmr quantum computing. *Phys. Rev. Lett.*, 83:1054–1057, 1999.
- [82] D. Gottesman and I. L. Chuang. Demonstrating the viability of universal quantum computation using teleportation and single-qubit operations. *Nature*, 402:390–393, 1999.

- [83] Cory et al. *Prog. Phys.*, 48:875, 2000.
- [84] M. D. Price, T. F. Havel, and D. G. Cory. Nuclear magnetic resonance spectroscopy: An experimentally accessible paradigm for quantum computing. *Physica D*, 120:82–101, 1998.
- [85] M. D. Price, S. S. Somaroo, A. E. Dunlop, T. F. Havel, and D. G. Cory. Generalized methods for the development of quantum logic gates for an nmr quantum information processor. *Phys. Rev. A*, 60:2777–2780, 1999.
- [86] M. D. Price, S. S. Somaroo, C.-H. Tseng, J. C. Gore, A. F. Fahmy, T. F. Havel, and D. G. Cory. Construction and implementation of nmr quantum logic gates for two-spin systems. *J. Mag. Res.*, 140:371–378, 1999.
- [87] A. Peres. Delayed choice for entanglement swapping. *J. Mod. Opt.*, 47:139, 2000.
- [88] G. Teklemariam, E. M. Fortunato, M. A. Pravia, Y. Sharf, T. F. Havel, D. G. Cory, A. Bhattaharyya, and J. Hou. Quantum erasers and probing classifications of entanglement using nuclear magnetic resonance. *Physical Review A*, 66:012309, 2002.
- [89] P. W. Shor. Scheme for reducing decoherence in quantum computer memory. *Phys. Rev. A*, 52:2493, 1995.
- [90] A. M. Steane. *Proc. R. Soc. London A*, 452:2551, 1995.
- [91] E. Knill, R. Laflamme, and L. Viola. Theory of quantum error correction for general noise. *Physical Review Letters*, 84:2525, 2000.
- [92] D. Bouwmeester, A. Ekert, and A. Zeilinger. *The Physics of Quantum Information*. Springer-Verlag, Berlin, 2000.
- [93] A. Fujiwara. Quantum channel identification problem. *Physical Review A*, 63:042304, 2001.
- [94] R. Alicki and M. Fannes. *Quantum Dynamical Systems*. Oxford University Press, Oxford, 2001.
- [95] U. Weiss. *Quantum Dissipative Systems*. World Scientific, London, 1999.
- [96] P. J. Rousseeuw and A. M. Leroy. *Robust Regression and Outlier Detection*. Wiley, New York, 1987.
- [97] A. Tarantola. *Inverse Problem Theory*. Elsevier Science, Amsterdam, 1987.
- [98] G. Lindblad. *Commun. Math. Phys.*, 48:119, 1976.
- [99] V. Gorini, A. Kossakowski, , and E. C. G. Sudarshan. Completely positive dynamical semigroups of n-level systems. *J. Math. Phys.*, 17:821, 1976.

- [100] I. T. Jolliffe. *Principal Component Analysis*. Springer-Verlag, Berlin, 1986.
- [101] T. F. Havel, Y. Sharf, L. Viola, and D. G. Cory. Hadamard products of product operators and the design of gradient-diffusion experiments for simulating decoherence by n. m. r. spectroscopy. *Physics Letters A*, 280:282–8, 2001.
- [102] R. A. Horn and C. R. Johnson. *Matrix Analysis*. Cambridge University Press, Cambridge, 1985.
- [103] I. Najfeld and T. F. Havel. *Adv. Appl. Math.*, 16:321, 1995.
- [104] C. B. Moler and C. F. van Loan. *SIAM Rev.*, 45:3, 2003.
- [105] G. Dahlquist and A. Bjorck. *Numerical Methods*. Prentice-Hall, New York, 1974.
- [106] I. Najfeld, K. T. Dayie, G. Wagner, and T. F. Havel. A robust method for estimating cross-relaxation rates from simultaneous fits to build-up and decay curves. *J. Magn. Reson.*, 124:372, 1997.
- [107] M. D. Choi. *Linear Algebr. Appl.*, 10:285, 1975.
- [108] R. Freeman, S. Wittekoek, and R. R. Ernst. High resolution nmr study of relaxation in a two-spin system. *J. Chem. Phys.*, 52:1529, 1970.
- [109] T. O. Levante and R. R. Ernst. Homogeneous versus inhomogeneous quantum-mechanical master equations. *Chem. Phys. Lett.*, 241:73, 1995.
- [110] R. Ghose. Average liouvillian theory in nuclear magnetic resonance - principles, properties and applications. *Concepts Magn. Reson.*, 12:152, 2000.
- [111] L. Viola, E. Knill, and S. Lloyd. Dynamical decoupling of open quantum systems. *Physical Review Letters*, 82:2417, 1999.
- [112] L. Viola, S. Lloyd, and E. Knill. Universal control of decoupled quantum systems. *Physical Review Letters*, 83:4888–91, 1999.
- [113] P. Zanardi and M. Rasetti. Noiseless quantum codes. *Phys. Rev. Lett.*, 79:3306–9, 1997.
- [114] P. Zanardi and M. Rasetti. Error avoiding quantum codes. *Modern Physics Letters B*, 11:1085–93, 1997.
- [115] D. A. Lidar and I. L. Chuang K. B. Whaley. Decoherence-free subspaces for quantum computation. *Physical Review Letters*, 81:2594–7, 1998.
- [116] D. Aharonov and M. Ben-Or. Fault-tolerant quantum computation with constant error. In *Proceedings of the 29th Annual ACM Symposium on the Theory of Computation*, New York, 1996. ACM Press.

- [117] A. Yu. Kitaev. Quantum computations: algorithms and error correction. *Russian Math. Surveys*, 52:1191–1249, 1997.
- [118] J. Preskill. Reliable quantum computers. *Proc. R. Soc. London A*, 454:385, 1998.
- [119] A. M. Steane. *Nature*, 399:124, 1999.
- [120] L. Viola, E. Knill, and R. Laflamme. Constructing qubits in physical systems. *Journal of Physics A*, 34:7067–79, 2001.
- [121] P. Zanardi. Stabilizing quantum information. *Physical Review A*, 63:012301/1–4, 2001.
- [122] D. Bacon, D. A. Lidar, and K. B. Whaley. Robustness of decoherence-free subspace for quantum computation. *Physical Review A*, 60:1944–55, 1999.
- [123] P. Zanardi. Stabilization of quantum information: A unified dynamical-algebraic approach. E-print available at <http://xxx.lanl.gov/abs/quant-ph/0203008>.
- [124] D. A. Lidar, D. Bacon, and K. B. Whaley. Concatenating decoherence-free subspaces with quantum error-correcting codes. *Physical Review Letters*, 82:4556, 1999.
- [125] W. Y. Hwang, H. Lee, D. Ahn, and S. W. Hwang. Efficient schemes for reducing imperfect collective decoherences. *Physical Review A*, 62:062305, 2000.
- [126] L.-A. Wu, M. S. Byrd, and D. A. Lidar. Efficient universal leakage elimination for physical and encoded qubits. E-print available at <http://xxx.lanl.gov/abs/quant-ph/0202168>.
- [127] Y. Sharf, D. G. Cory, S. S. Somaroo, T. F. Havel, E. Knill, R. Laflamme, and W. H. Zurek. A study of quantum error correction by geometric algebra and liquid-state nmr spectroscopy. *Molecular Physics*, 98(17):1347–1363, 2000.
- [128] E. M. Fortunato, M. A. Pravia, N. Boulant, G. Teklemariam, T. F. Havel, and D. G. Cory. Design of strongly modulating pulses to implement precise effective hamiltonians in quantum information processing. *Journal of Chemical Physics*, 116:7599–606, 2002.
- [129] N. Boulant, J. Yang, K. Edmonds, M. A. Pravia, and D. G. Cory. Experimental demonstration of an entanglement swapping operation and improved control in nmr quantum information processing. *Physical Review A*, 68:032305, 2003.
- [130] J. E. Ollenrenshaw, D. A. Lidar, and L. E. Kay. A magnetic resonance realization of decoherence-free quantum computation. *Physical Review Letters*, 91:217904, 2003.

- [131] C. King and M. B. Ruskai. Minimal entropy of states emerging from noisy quantum channels. *IEEE Transactions on information theory*, 47:192, 2001.